DEVELOPMENT OF A NEW SPECTRAL MODELING APPROACH TO INVESTIGATE THE DYNAMIC AND BUCKLING BEHAVIOR OF COMPOSITE STRUCTURES

by
MIRMEYSAM RAFIEI ANAMAGH

Submitted to the Graduate School of Engineering and Natural Sciences
in partial fulfillment of the requirements for
the degree of Doctor of Philosophy

Sabancı University
June 2021

DEVELOPMENT OF A NEW SPECTRAL MODELING APPROACH TO INVESTIGATE THE DYNAMIC AND BUCKLING BEHAVIOR OF COMPOSITE STRUCTURES

Approved by:

Date of Approval: July 10, 2021

ABSTRACT

DEVELOPMENT OF A NEW SPECTRAL MODELING APPROACH TO INVESTIGATE THE DYNAMIC AND BUCKLING BEHAVIOR OF COMPOSITE STRUCTURES

MIRMEYSAM RAFIEI ANAMAGH

Ph.D. Thesis, July 2021

Thesis Supervisor: Asst. Prof. Bekir Bediz

Keywords: Chebyshev, meshless methods, composite structures, functionally-graded materials, carbon nanotubes, graphene nano-platelets, vibration, buckling, design

In recent years, composite materials have become increasingly important due to rapidly increasing applications in aerospace, civil, offshore engineering and structural systems in other modern industries. The use of composite materials in the automotive and aerospace industry continues to become widespread due to its high specific strength and high specific rigidity. Since, the composite structures are critical to the functional and failure characteristics of a myriad of systems, understanding and predicting the static, buckling, and dynamic/vibration behavior of these systems is highly crucial. A composite material is obtained basically by mixing two or more materials having different physical and/or chemical properties.

The material properties of the obtained material have different physical and chemical properties. According to the reinforcement type, composite materials are classified as fiber-reinforced, particle-reinforced, and laminated/sandwich composite materials. Also, another category of composite materials are functionally graded materials. Due to the flexibility of the reinforcing process using functionally graded materials, it is possible to design and produce composite materials with desired properties along the specific direction of the structure. Predicting the strains and stresses, buckling instability and dynamics of composite materials is critical to the functional and failure characteristics of a myriad of systems. Furthermore, during the design stage of a composite structure, it is necessary to perform dynamic/structural analysis for the entire design alternatives.

Although there are many analytical/numerical modeling methods developed for com-

posite structures in the literature, they are either for composite structures having simple geometries (one-dimensional models such as beam or two-dimensional models such as plates) or computationally inefficient such as finite element technique. Therefore, in literature, there is no comprehensive modeling technique that can accurately and efficiently calculate the deformation, buckling loads (instability), the vibrational behavior of composite structures having arbitrary geometries under mixed boundary conditions.

In this thesis, it is aimed to develop a new modeling technique for accurate and efficient prediction of two-dimensional and three-dimensional vibration/dynamic behavior, static, and buckling behavior of composite structures and to integrate the proposed solution approach with an optimization algorithm to determine the optimum design. In the proposed modeling technique, first order deformation theory as a two-dimensional modeling and three-dimensional elasticity equations will be used and above-mentioned analysis will be performed using kinetic and strain energies of the composite structure. Since the material properties of composite structures may vary continuously/discontinuously or depend on the direction, the constitutive relationship between strains and stresses needs to be expressed to include all the different material properties specified. Furthermore, to simplify the domain of the boundary value problem, necessary coordinate transformations will be derived to transform the geometries of composite structures having variable curvature along one or two directions. To obtain high accuracy and high computational efficiency in the analyses, a spectral solution technique will be used incorporating Chebyshev polynomials in discretizing the problem domain.

As a general conclusion, this research aims to present an accurate approach to decrease the cost of analysing of composite structures with complex materials and geometries to be a promising method for optimization studies.

ÖZET

KOMPOZIT YAPILARIN DINAMIK VE BURKULMA DAVRANIŞINI ARAŞTIRMAK IÇIN YENI BIR SPEKTRAL MODELLEME YAKLAŞIMININ GELIŞTIRILMESI

MIRMEYSAM RAFIEI ANAMAGH

DOCTORA TEZİ, TEMMUZ 2021

Tez Danışmanı: Asst. Prof. Bekir Bediz

Anahtar Kelimeler: Chebyshev, ağsız yöntemler, kompozit yapılar, fonksiyonel olarak derecelendirilmiş malzemeler, karbon nanotüpler, grafen nano-plakalar, titreşim, burkulma, tasarım

Son yıllarda, inşaat, denizcilik, havacılık mühendisliği ve diğer modern endüstrilerdeki yapısal sistemlerdeki hızla artan uygulamalarından dolayı kompozit malzemeler giderek önem kazanmıştır. Özellikle, kompozit malzemelerin yüksek spesifik mukavemet ve yüksek spesifik rijitlik benzeri üstün özelliklerinden dolayı otomotiv ve havacılık sanayiinde kullanımı giderek yaygınlaşmaktadır. Dolayısıyla, bu yapıların gerilme (yarı-durağan ve dinamik kuvvetler altında), burkulma (yapısal kararsızlık) ve dinamik/titreşim davranışlarının modellenmesi, fonksiyonel özellikleri ve performansları açısından büyük bir önem arz eder.

Kompozit malzeme, temel olarak farklı fiziksel ve/veya kimyasal özelliklere sahip iki veya daha fazla malzemenin karıştırılması/birleştirilmesi yolu ile elde edilir. Elde edilen malzeme, bu malzemelerden farklı fiziksel ve kimyasal özelliklere sahiptir. Kompozit malzemeler takviye türüne göre lif destekli, parçacık destekli ve katmanlı kompozit malzemeler olmak üzere üçe ayrılır. Takviye işleminin esnekliğinden dolayı istenilen sağlamlık ve sertlik gibi özelliklere sahip kompozit malzemeler tasarlanabilir ve üretilebilir. Kullanıldıkları alanlardan dolayı kompozit malzemelerin yapısal kararsızlık ve dinamik davranışlarının yüksek hassasiyet ile bulunması çalışma koşulları altındaki davranışları ve arızalanma karakteristikleri açısından kritik bir öneme sahiptir. Ayrıca tasarım sürecinde ortaya çıkan tüm tasarım alternatiflerinin değerlendirilmesi için dinamik/yapısal analizlerinin yapılması ve sistem karakteris-

tiklerinin çıkarılan tüm alternatif tasarımlar için belirlenmesi ve en uygun tasarımın seçilmesi gerekmektedir.

Literatürde kompozit malzemelerin yapısal/dinamik davranışlarını tahmin etmek için birçok analitik/numerik yöntem olmasına rağmen, bu yöntemler sadece belli basit geometrideki (kiriş benzeri bir boyutlu -1B- ya da plaka benzeri iki boyutlu -2B-) kompozit yapılar için çalışmaktadır ya da sonlu elemanlar tekniği gibi uygulama alanı geniş ama oldukça zaman alıcı yöntemlerdir. Fakat, günümüzde üç boyutlu kompozit yapıların gerilme/gerinim, burkulma (yapısal kararsızlık) ve dinamik davranışlarının tam olarak anlaşılmasını ve çalışmaları esnasında değişik dinamik yükler altındaki davranışlarının incelenmesini/ön görülmesini sağlayacak şekilde kapsamlı, yüksek başarımlı (hem yüksek doğruluğa hem de yüksek hesaplama verimliliğine sahip) bir hesaplama tekniği bulunmamaktadır.

Bu tezde, kompozit yapıların iki ve üç boyutlu titreşim/dinamik davranışlarının, burkulma davranışlarının ve deformasyon karakteristiklerinin hızlı ve yüksek doğrulukla tahmini için yeni bir modelleme tekniği geliştirilmesi ve bir tasarım sürecinde optimum özelliklere sahip kompozit yapının bulunabilmesi amacıyla geliştirilecek modelleme tekniği ile entegre çalışabilecek optimizasyon (eniyileme) algoritması tasarlanması amaçlanmaktadır. Öngörülen modelleme tekniğinde birinci dereceden kayma deformasyon teorisi (2-B-) ve üç boyutlu doğrusal olmayan elastisite denklemleri kullanılacak ve belirtilen analizler yapının kinetik ve gerinim enerjis kullanılarak gerçekleştirilecektir. Kompozit yapıların malzeme özellikleri yapı içerisinde sürekli veya süreksiz bir davranış gösterebileceği için veya yöne bağlı olabileceği için gerilim ve gerinim arasında ilişkiyi içeren yapısal matris belirtilen tüm farklı malzeme özelliklerini içerecek şekilde ifade edilecektir. Endüstride kullanılan değişken kavisli ve kompleks bir kesit alanına sahip olan geometrilerdeki kompozit yapıların incelenmesi için gerekli koordinat transformasyonları tanımlanarak problemin tanımlandığı alan basitleştirilecektir. Yapısal ve dinamik analizler için elde edilecek denklemlerin çözümünde hem yüksek doğruluğun hem de yüksek hesaplama verimliliğinin elde edilmesi amacıyla spektral bir çözüm yönteminden yararlanılacak ve denklemlerin ayrıklaştırılmasında Chebyshev polinomları kullanılacaktır. Geliştirilen modelleme tekniği sonlu elemanlar yöntemi kullanılarak doğrulanacaktır.

Genel bir sonuç olarak, bu araştırma, optimizasyon çalışmaları için umut verici bir yöntem olarak karmaşık malzeme ve geometrilere sahip kompozit yapıların analizinin maliyetini düşürmeyi amaçlamaktadır.

ACKNOWLEDGEMENTS

Another step of my life is finished with all nice and tough days. I am a lucky person to be a member of Sabanci university where I found valuable friends and colleagues who support me in tough days and share their cheerfulness days with me. I know, I can not express my deep appreciations in these sentences, I hope all to be healthy and successful in their whole life.

My family, for their unconditional love and support in each day of my life, I appreciate them. My love, Mahsa, who I started this journey with her, who I can not continue this road without her help, support and motivations, I would like to express my deep gratitude to her.

I want to thanks my advisor, Prof. Bekir Bediz, who I obtain valuable experiences from him in academic life. His guidance, persistence on a issue and his critical view at the subject are exemplary. He always shares his knowledge, skills and experiences to support our team and motives us to be stable in the studies. I thanks him for all of good things that I learned from him.

Also, I want to thanks committee members; Prof. Serkan Dağ, Assoc. Prof. İpek Başdoğan, Asst. Prof. Polat Şendur and Asst. Prof. Adnan Kefal, who provide valuable suggestion regarding my research. I would like to thanks people who devote their time to guide me in my research field; Assoc. Prof. Güllü Kızıltaş Şendur, Prof. Melih Papila, Asst. Prof. Eralp Demir and Asst. Prof. Kamer Kaya.

All these issues are happened with the existence of Sabanci University where provides us a comfortable, equipped and efficient place to study and research. I hope to see the university in higher academic levels in the world.

To the memory of
Dr. Mohammad Mosaddegh

LIST OF TABLES

LIST OF FIGURES

xvi

LIST OF ABBREVIATIONS

1.   INTRODUCTION

1.1 Motivation

Material science has achieved notable progress in recent years to produce novel materials with extraordinary mechanical properties for various applications such as aerospace, energy, and biomedical fields. In these wide range of engineering fields, the need for lighter and stiffer materials become inescapable. Composite materials are one of the outstanding materials that can meet the need for many cutting-edge applications due to their high stiffness-to-weight ratio, resistance to corrosion and thermal effects [1].

Composite materials are basically composed of two or more materials [2]. Thus, tailoring the design (or material properties) is highly feasible [3]. However, considering the vast design space and complexity in geometry, an accurate and efficient modeling approach is required to leverage the flexibility in design.

Therefore, the main goal of this study is to develop an accurate and computationally efficient modeling approach to study and predict the behavior of composite structures.

1.2 Composite materials

Materials have always played a major role in the development and growth of human civilization. Generally, materials can be divided into four main categories; **(i)** metal, **(ii)** polymers, **(iii)** ceramics, and **(iv)** composites. Composite materials are composed of the first three categories of materials. The use of composite materials can be traced back to 4000 BC or even earlier[4]. Evidence exists on the use of composites in ancient Japan, where the Samurais used laminated metals to make swords[5].

The composite materials can be considered as a two-phase material that includes a continuous phase (matrix) and a discontinuous phase (reinforcement) [2]. The role of the matrix phase is to bind the reinforcement phase together. The reinforcement parts are not dissolved or merged. Therefore, the constituent materials retain their individual properties. The resultant combination of these two-phase exhibits an efficient behavior in comparison to each phase behavior merely. From the structural and material points of view, the composite definition includes two main categories where they can be subdivided into the several different types as shown in Fig. 1.1. Furthermore, Table 1.1 is presented for common terms used in the composite materials field.
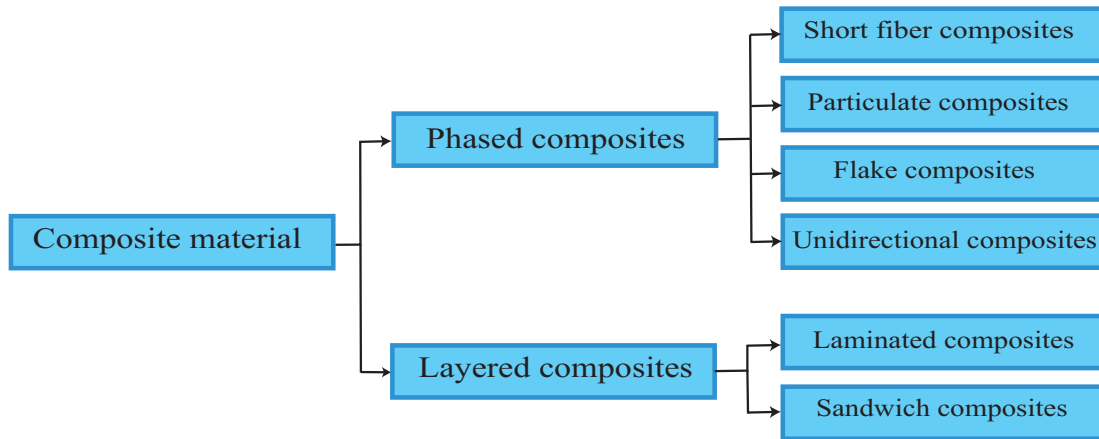
Figure 1.1 Categorization of composite materials.

Table 1.1 Terminology for composite materials.

Terminology	Definition
Isotropic	Material properties are not dependent on directions in an isotropic material.
Anisotropic	Material properties are dependent on directions.
Orthotropic	Material properties that are different in three mutually perpendicular directions at a point.
Homogeneous	Material has equal or same material properties in a specified direction at all points.
Nonhomogeneous	Matrial has unequal or dissimilar material properties in a specified direction at different points.
Lamina	It (laminae in plural) is a single layer or ply in a laminated composite material.
Laminate	It is a laminated composite structural element that is made by a number of laminae.

The first category is the phased composites in which inclusions in the form of **(i)** short fibers/whiskers, **(ii)** particles, **(iii)** flakes, and **(iv)** continuous fibers are added to a continuous matrix. In short fiber, particulate, and flake composites, the inclusions are distributed randomly; thus the material properties are isotropic [5]. Note that, although the material properties are isotropic, the inclusions can be added to increase/decrease along a specified direction to create a varying material property [5]. On the other hand, unidirectional composites include continuous fibers. Since the strength and stiffness of the structure highly depend on the direction of the fibers, the material property is anisotropic [5].

The second category is the layered composites, commonly divided as laminated and sandwich composites. The laminated composite structures include stacked thin plies, where each ply is reinforced with unidirectional, bidirectional, or multi-directional fibers. In the case of sandwich composites, there is a core layer (commonly lightweight) between two face sheets. The core material can be foam or honeycomb type of structures [6].

The composite materials can be produced via various manufacturing processes as presented in Fig. 1.2. Open mold processes, also referred to as contact molding processes, are one of the most common fabrication techniques that operate as placing either dry fabrics or prepregs on an open mold [7, 8]. The main advantage of these processes is that the cost of tooling and equipment, and machinery is generally low. On the other hand, in the closed mold processes, the fabrication is performed in a closed mold as the names suggests; thus it is more expensive compared to the open mold process. The closed molding is done by pumping the matrix part in a porous environment which contains the fibers. Another fabrication process is continuous molding processes that include pultrusion, winding processes, fiber placement, etc. Winding processes are those in which continuous reinforcement in the form of either roving or tape is deposited on a rotating mandrel. Two distinct winding processes are in practice, filament winding and tape winding [5].
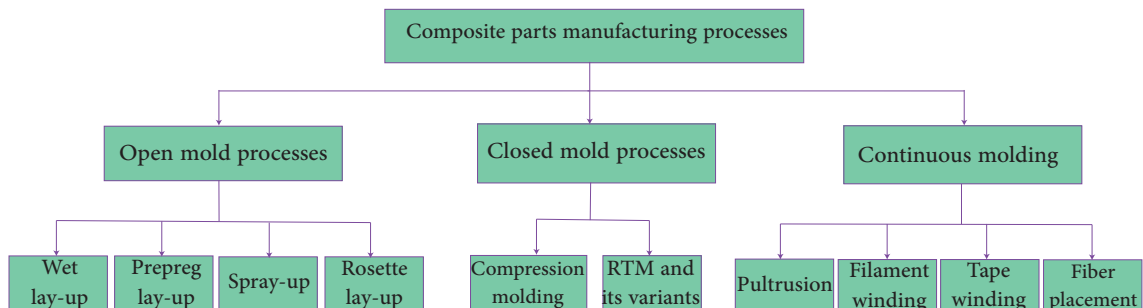
Figure 1.2 Manufacturing processes of composite parts.

The introduction of advanced composites has influenced almost every aspect of modern life. Today, major impacts are experienced in the aerospace/aviation, automobile, naval and civil engineering application, *etc.* Composites have their own unique features that enables them to be used in a wide range of applications [9, 10, 11, 12]. However, note that they have advantages as well as disadvantages as listed below:

- Advantageous:
    - high strength and stiffness
    - high weight-to-stiffness ratio

- high fatigue strength

- inherent material damping and good impact properties

- design flexibility

- resistance to corrosion

- near net shape part and lower part count

- cost-effective product development

- Disadvantages:

    - may have low service temperature

    - sensitivity to radiation and moisture

    - low elastic properties in the transverse direction

    - complex design and analysis

    - complex mechanical characterization

    - high cost of raw materials and fabrication

    - difficulty in joining

A common type of (laminated) composite structures is the singly- or doubly-curved geometries since the coupling between the membrane and bending deformations leads to higher strength [13, 14, 15]. Thus, these structures have attracted increasing attention leading to a wide range of applications [16]. In recent decades, composite sandwich structures have been designed and used in complicated systems such as aerospace applications (*e.g.*, helicopter rotor blades, large wind turbine blades, fitting, joints and ribs, and vehicle armor).

In addition to the fabrication of thin composite shells and plates with low curvature, thick laminates are growing to be utilized in automobile and aerospace industries to decrease the system's overall weight. Sandwich types of structures can be designed with specific materials to satisfy the reduction and enhancement of the weight and stiffness properties of the thick structures, respectively. Sandwich structures consist of two thin and stiff face-sheets, usually the same thickness, that are separated by a lightweight, thicker core. The face-sheets carry almost all of the bending and in-plane loads, while the core helps stabilizing the face-sheets and defines the flexural stiffness and out-of-plane shear and compressive behavior [17]. Generally, these structures are subjected to dynamic loading. Therefore, it is highly crucial to obtain

high-fidelity computationally efficient models to understand their dynamic/vibration behavior [18].

1.2.1 Functionally graded materials

The main scope of this study is on developing novel modeling approaches for thin/thick functionally graded (FG) composites. Functionally graded materials (FGM), a concept in composite structures that is proposed in the late twentieth century, are heterogeneous composites made from different phases of material constituents (usually ceramic and metal) [19, 20]. Depending on the volume fraction of the material constituents that is generally described by a simple power law or an exponential relationship, a smooth transition (variation) of material properties can be obtained within the structure (along the gradation direction) [21, 22]. Therefore, it is possible to mitigate the problems of the conventional laminated composite structures such as delamination and matrix cracking problems that occur due to the sudden change of material properties [23]. Furthermore, to achieve a desired dynamic behavior, a tailor-made composite structure can be designed by simply varying the gradation amount and rate along a desired direction within the domain of the structure [23, 24, 25].

To describe the material distribution within the FGM structure along one or more spatial directions, there are two common approaches: **(i)** Mori–Tanaka Method [21, 22, 26] or **(ii)** the theory of mixtures [14, 27]. In the theory of mixtures method, the material properties of the composite structure is found as a linear combination of the constitute materials based on their volumetric ratios. Various models are based on the thoery of mixture such as Rule of mixture (ROM) [28], Chamis (Ch) [29], Halpin-Tsai (HT) [30], Modified rule of mixture (ROMm)[31]. In the Mori–Tanaka approach the material properties are found using Eshelby's elasticity solution using the eigenstrain concept [32] where the idea is to establish an average behavior defined from fiber and matrix behaviors. To find the volumetric fractions for both techniques, different methods such as four parameter power law and Weibull distributions are used in literature [14, 33].

As aforementioned, FGMs are fabricated generally using metals and ceramics as in particulate composites (see Fig. 1.1). However, it is possible to obtain a varying material property through various approaches such as the inclusion of short fibers/whiskers (*e.g.* carbon nanotubes - CNTs) and flake composites (*e.g.* graphene nano-platelets - GPLs) [34].

1.2.1.1 Porous media

Porous (cellular) materials, such as metal foams, are one of the recent composite materials [35, 36]. The porosity distribution in the structure can be engineered to offer distinct properties such as weight reduction, energy absorption, and bio-compatibility; thereby enabling these materials to be used in diverse applications in aerospace, automobile, civil industries, and bio-engineering fields [37, 35]. Although, there has been a lot of attention to these materials in recent years, mainly materials having uniform or random porosity distributions are used. However, above-mentioned distinct properties highly depend on the porosity distribution, and random porosity distributions may have problems such as mismatch of mechanical properties. To better control the associated material properties of the porous structures, a smooth (*i.e.* functionally graded - FG) distribution can be utilized [38, 39, 40].

Although, the porosity in the structure can be tailored to achieve an FGM property and meet the design requirements, effective stiffness of the material is significantly compromised due to the presence of pores [41]. To overcome this reduction in stiffness without increasing the weight of the material, one common approach is to reinforce the material with nanofillers [42, 43, 44]. In this regard, due to the remarkable mechanical and stability characteristics, carbon nanotubes (CNTs) have been widely used as reinforcement material [45, 46]. More recently, instead of CNTs, platelets that include few layers of graphene (graphene platelets - GPLs) have been introduced as a reinforcement material. It has been reported that compared to CNTs, due to the increased interaction between the surfaces of GPLs and the matrix material, GPLs showed better mechanical enhancement [42, 47, 48].

1.2.1.2 Carbon nanotubes

Carbon nanotubes (CNTs) have been widely used as a reinforcement material due to their extraordinary mechanical and stability characteristics (high strength, high stiffness, and high aspect ratio but very low density) [49]. Carbon nanotubes can be produced in two different configuration: **(i)** single-walled carbon nanotube (SWCNT) [50, 51] and **(ii)** multi-walled carbon nanotube (MWCNT). Single-walled carbon nanotubes are fabricated by rolling a graphene sheet as a cylindrical shaped particle with 1 nm diameter, where the MWCNTs are fabricated as an array of concentric cylinders with an interlayer spacing of 3.4 nm [52].

Until recently, scientists mostly research on the traditional fiber fillers. These con-

ventional fibers have an impressive ultimate and yield stresses properties with a range of 230–725 GPa and 1.5–4.8 GPa, respectively [53]. The carbon nanotubes with a diameter of between 1 to 100 nm and a length in the order of millimeters provide superior mechanical properties compared to the traditional fibers; for instance the Young's Modulus exceeds 1 TPa. Thus, they act as the leader type of carbon fibers [54] and an excellent candidate to be used in . FGMs. Functionally graded CNTs (FGCNTs) as an advanced type of FGM can also be engineered to achieve the desired behavior in a preferred direction.

The FGCNTs were presented by Shen [55] for the first time with an isotropic material property. After Shen's study, it can be seen that there is an extraordinary interest on FGCNT materials [56]. After Shen's study, a large body of literature is devoted to the advantages of using CNTs to enhance the dynamic and static behavior of composite structures. Investigations demonstrate that utilizing a meager percentage of the weight of CNTs compared to the matrix part of the composite has a remarkable effect in improving the performance of the structure [57, 58, 59, 60, 61]. Thostenson and Chou [62] show that using CNTs, the tensile modulus, yield strength, and ultimate strength of the structure increases significantly. Also, they concluded that the improvement of elastic modulus with the aligned CNTs is five times greater than the improvement of the randomly oriented CNTs. Zhu. et al. [63] considered the various distribution type of CNTs along with the thickness of the structure and show that the volume fraction distribution of CNTs has a major role in changing the natural frequencies and mode shapes of the moderately thick structure. Aragh et al. [64] studied different distribution of CNTs and geometry parameters and their results indicate that the symmetric distribution of CNTs enhances the dynamic behavior more effectively than the uniform distribution of CNTs.

Considering the mentioned extraordinary properties of FGCNTs, they are a promising candidate to be used in the face-sheet and core layers of a sandwich structure to strengthen the weak structures such as honeycomb type of structures. In practice, sandwich structures include a core layer, usually composed of foam materials [65] or lattice materials [66]. In this regard, the advantage of the foam type of layer is to have a continuous form, leading to a continuous connection to the face-sheets. Nevertheless, the foam structures have low stiffness and strength. In contrast, the lattice material such as honeycomb types possesses high stiffness and strength due to their strong nodal connectivity [67]. Due to the high out-of-plane stiffness, longitudinal shear strength, and ultra-low density characteristics of honeycombs, they are considered a viable solution for aerospace engineering application [68]. To overcome the honeycomb's weakness in the in-plane stiffness, the CNT face-sheets can be used.

1.2.1.3 Graphene platelets

Functionally graded graphene platelets (GPL) reinforced porous composite materials are a relatively new concept and have attracted immense attention since it can be widely used in many engineering applications. Thus, it is highly critical to develop novel modeling approaches to accurately and efficiently predict their mechanical and dynamic behavior. Although, there are many studies regarding modeling of the conventional composite materials, the computational modeling studies of GPL reinforced FG porous composites are still limited. The studies in the literature can be divided into two categories as beams and plates/shells depending on the domain of the problem.

Among the recent studies on the GPL reinforced FG porous material (FGPM-GPL) composites, the majority of the literature are devoted to investigate the bending and dynamic behavior of structures using beam based theories. Kitipornchai et al. [42] employed the Timoshenko beam theory with the Ritz approach to obtain the natural frequencies and critical buckling loads of nano composite beams. Then, buckling and post-buckling behavior of functionally graded multilayer beams reinforced with randomly oriented GPLs was studied by Yang et al. [69]. In this study, the first order shear deformation theory (FSDT) was used to express the kinematic relations and the numerical solution was performed using the differential quadrature method (DQM). They concluded that introducing even a low percentage of GPLs into the matrix material enables the composite structure to have stiffer behavior. The post-buckling behavior was also studied by Kiani and Mirzaei [70] for laminated beams reinforced with the GPLs using the von Karman type of strain displacement relations and including the temperature effects. In a recent work done by Ganapathi et al. [71], the vibrational behavior of curved FG porous beams with GPLs by employing the trigonometric shear deformation theory and considering thickness stretching effect was studied. The Navier's method is applied to solve the derived equations and the results showed that porosity distribution over the thickness result in variation of natural frequencies. Apart from predicting the natural frequencies and buckling loads, dynamic stability is another important issue. Liu et al. [72] studied the stability of FG porous arches reinforced with graphene platelets (GPLs) analytically. Later, Zhao et al. [48] conducted the instability analysis using the classical Euler–Bernoulli theory and Galerkin approach. They investigated the dynamic instability using the Bolotin method. The dynamic buckling analysis of FGPM-GPL plates were investigated by Li et al. [73]. They concluded that the porosity and GPLs distributions have a significant effect on the stiffness of the plate. The dynamic behavior and stability of the FGPM-GPL plates under dynamic/aerodynamic

loads were also investigated [74, 75]. It was concluded that increasing the percentage of GPLs in the structure increases the resonance frequencies.

1.3 Modeling approaches of composite structures

To model composite structures, researchers use either two-dimensional (2D) or three-dimensional (3D) modeling approaches based on the geometry of structure such as thickness ratio and curvature amount. It should be noticed that there is not a straightforward conclusion to choose a 2D or 3D approach. However, using an appropriate approach can help to decrease the cost of computation. Furthermore, using an approach that enables to predict strains and stresses at any location of the structure is a critical issue [76]. Therefore, in this section, an overview of the common 2D and 3D modeling approaches is presented.

1.3.1 Two-dimensional approaches

Due to the wide range of applications, plate/shell type of composite structures have also attracted considerable attention due to their load carrying capabilities. Majority of the studies based on different 2D analytical and numerical methods are listed in the review articles of Gibson et al. [77], Liew et al. [54], and Swaminathan et al. [19]; however only the significant and recent relevant works are listed here for the sake of completeness. These studies can be classified according to the order of the shear deformation mechanism that is followed, such as Kirchhoff–Love (classical) plate theory (CPT) [78, 79, 80, 81, 82], Mindlin plate (first order shear deformation theory — FSDT) theory [81, 83, 84, 85], or higher-order shear deformation theories (HSDT) [86, 87]. The classical theory that follows Kirchhoff–Love assumptions is only suitable for thin plates and shells as it neglects the effects of the shear deformation [88, 89, 90, 91, 92]. To overcome the limitations of the classical plate theory, Mindlin or higher order shear theories are utilized. For instance, in Tornabene et al.'s work [93, 94], the dynamics of the doubly-curved plate is analyzed using FSDT where the solution is performed using the Generalized Differential Quadrature (GQD) method.

To overcome the inadequacies of the plate theories (arising from the restricting assumptions for the deformation kinematics) and also to increase their computational efficiency, attempts were made to modify the plate/shell theories to accurately and

efficiently capture the dynamics of composites and also to construct a general modeling approach. For instance, Tornabene et al. [16, 86] overcome the inadequacies of the plate theory in the case of zig-zag effects [95] and analyzed the dynamics of laminated doubly-curved structures including plate geometries with arbitrarily shaped in-plane geometries [16] and varying thickness [86]. Another important modeling approach that can overcome the limitations in deformation kinematics is to use meshless methods such as unified formulation (UF) where the displacement field is written by approximating functions; and the solution can be performed using collation methods or generalized differential quadrature (GDQ) method [96, 97]. The GQD method is one of the common approaches used in the literature due to its simplicity and versatility [98]. However, the derivative and integral operations are performed numerically in the GQD technique; thereby, the selected basis functions and the sampling scheme highly effect the precision of the results. To analyze the arbitrarily shaped composite plates, in some recent studies, a unified modeling approach such as integration of NURBS or isogeometric modeling or conventional mapping approach commonly used in finite element method to plate modeling equations is followed [99, 100, 101, 102, 43]. This method enables accurately capturing the geometry of the structure and achieving more controllable continuity across elements.

As stated above, computational duration is another important factor of the developed modeling techniques. Thai et al. [100] and Khiloun et al. [103] used a refined plate model and thus decreased the total number of degrees of freedom of the structure. Another common approach to increase the computational efficiency is to select fast converging orthogonal polynomials in the solution approach. To achieve this, Fourier series or Chebyshev (Tchebychev) polynomials are selected since they present exponential convergence characteristics [104, 105, 106, 107]. Furthermore, spectral/meshless methods lead to lower number of degrees of freedom; since these methods uses basis functions that are non-zero over the whole domain, they enable accurate and computationally efficient prediction of the mechanical and dynamic behavior [108, 107, 109].

Despite that the mentioned plate theories can predict the accurate behavior of the thin structures, they have a critical weakness in the study of thick structures, especially when the material properties have a smooth variation through the thickness [110]. Demasi [111] studied the static behavior of a laminated structure using two dimensional, quasi-three dimensional, and exact three dimensional. He concluded that by increasing the thickness of layers, the accuracy of the two-dimensional approach is decreased. For the moderately thick structures, proportional types of plate theories should be selected among various types of theories. Also, he demonstrated

the high accuracy of layer-wise modeling of laminated structures. Using a simplified formulation of plate theories indicates that they lack accuracy in analyzing the free vibrations [112]. Furthermore, in the case of sandwich structures, the discontinuity between the face-sheets and the core layer with different material properties carried another difficulty for the shell/plate theories [113].

1.3.2 Three-dimensional approaches

Although, there is a large body of literature on 2D (plate and shell) methods to understand the dynamics of composite structure, there are only a few studies on fully 3D methods due to the difficulties in the modeling process [19]. However, 3D methods lead to higher accuracy and also automatically eliminates the need to make the restricting assumptions for the deformation kinematics of the structure as in most of the 2D approaches [114, 115, 116]. In this regard, various HSDT with refinement parameters and quasi-3D theories are presented to catch the thick structure's behavior, especially the transverse deformation of the structure as close as possible to the 3D solution. However, the mentioned approaches are highly affected by geometry's complexity, such as change of thickness and radius of curvature. Also, deriving the analytical or numerical solutions of these approaches need too much effort.

As a part of the engineering process, the empirical stage of testing the study can increase the cost due to the repetition of the test process to evaluate the analyzing method, especially if the study is accomplished for the cases with plastic deformations such as impact or buckling analysis. Hence, it is necessary to improve an accurate and sufficient three-dimensional method to minimize the development costs.

In recent years, it can be seen that literature have been more devoted to using three-dimensional approaches to model and predict the behavior of thick structures. Farid et al.[117] studied a thick and functionally graded curved panel using the three-dimensional elasticity formulation. They used a hybrid semi-analytic-differential quadrature method to solve the problem with the series based expansion of displacement components[117]. In another work done by Malekzadeh, the mentioned method is employed to study the free vibration of a functionally graded structure(FGM) [118]. Liu et al. [119] used the 3D elasticity approach to investigate the static and vibration behavior of a structure reinforced with CNTs. In this study, the state-space-based differential quadrature method is employed to solve the equation of motion for an annular-shaped structure. Malekzadeh and Heydarpour

[120] utilized 3D elasticity to investigate the static and free vibration behavior of a laminated composite structure reinforced with CNTs. A semi-analytical approach composed of the layer-wise differential quadrature method and the series solution was employed to model the 3D variations of the displacement components accurately. Alibegloo et al. [121, 122] study the static and vibrational behavior of CNT reinforced type of laminated structure using 3D elasticity equation and Fourier series expansion approach. In another research, Albeigloo et al. [121, 123] apply the 3D elasticity approach to the FGM sandwich structures where the face-sheets are the soft materials. They carried out the static and vibration analysis by employing the differential quadrature approach and the Fourier series expansion method.

The main disadvantage of using three-dimensional solution of thick structures is the computational time. As a part of the author's knowledge, advances in computer sciences and using new meshless methods integrated with mathematical science can be part of investigations of the engineering field to overcome the computational weakness of the 3D solution methods. In deriving the BVP, 3D elasticity equations are used; and the solutions are carried out using techniques such as spectral element method (SEM), differential quadrature method (DQM), or quadrature element method (QEM) [85, 124, 125]. Although, they are computationally efficient, they suffer due to the difficulty in selecting proper basis/trial functions that needs to be determined for each different geometry and boundary conditions (thus, the solutions can only be performed for certain simple geometries and boundary conditions), and the necessity to use special numerical algorithms to calculate the derivative and integral operations.

One of the most common method that is used in literature to model the dynamics (vibration behavior) of composite structures is finite-element (FE) methods [19, 126, 127]. The FE technique uses weak formulation of the boundary value problem (BVP) and requires an arduous effort to obtain a suitable mesh of the investigated structure. If 3D elements are used, this technique enables accurate prediction of deformations within the structure, natural frequencies, and mode shapes, even for FGM structures having complex geometries and material distributions. Although finite element (FE) based methods are the prevailing approach to analyze mechanical/dynamic behavior of structures, it has several drawbacks: **(i)** when the material gradation rate is rapid along one or more directions, obtaining a converged result requires a significant amount of computational cost; **(ii)** when the investigated structure has complex geometry (for instance sharp edges), it is required to perform h-refinement or p-refinement techniques to achieve accurate results. Both of the refinement techniques increases the size of the system matrices, leading to a decrease in the computational efficiency. Consequently, researches aim to develop more computationally efficient

techniques. However, computational efficiency is the main problem of FE approach. Especially time domain response simulations and harmonic solutions lead to overlong simulation duration.

1.4 Design of composite structures

Due to the flexibility in composite fabrication, the material properties and/or the geometry of the structure can be tailored to meet the design requirements. The process of finding the best possible design is called optimization. In the modern era, optimization is one of the most crucial issues associated with engineering designs. Weight reduction, utilizing less expensive materials, increasing the strength, reducing the number of prototype fabrication and testing have always been sought in designing different mechanical structures. As a result, there are many optimization studies conducted on composite structures, that are focused on developing new optimization algorithms and/or on implementing new design variables, objective functions, and/or constraints. A great insight into optimization of composite structures can be achieved by probing these two areas individually and/or combining them comprehensively.

Commonly, the objectives of most of the studies in literature are either maximizing the critical buckling load [128], minimizing the weight [129], maximizing the fundamental frequency [130], minimizing the coefficient of thermal expansion and maximizing the elasticity modulus [131] or combination of them, where the design variables can be defined as stacking sequence of layers and fiber orientations.

From the literature, it can be concluded that the design studies related to the sandwich structures with accurate solutions need more and comprehensive investigations. Setoodeh and Shojaei accomplished an optimization study to obtain optimum CNTs orientations for maximizing the buckling critical force [132]. They performed the optimization using Genetic algorithms. Vo-Duy et al. [133] conducted an optimization of natural frequencies of the structure by designing the CNTs orientations. Adaptive Elicit Differential Evolution Algorithm (AEDEA) is developed by authors to be used in the optimization process. In the reviewed literature, the CNTs orientations are designed for one layer or for a laminated structure. However, majority of the studies focused on dynamic or static behavior optimizations of sandwich structures are conducted for FGM structures. The materials volume, thickness, and distribution types of FGM are the main design variables of these studies [134, 135, 136]. The literature reviews show a lack of research on the design of sandwich structures

via a 3D modeling approach.

1.5 Objectives

In this thesis, it is aimed to develop a new modeling technique for accurate and efficient prediction of two-dimensional and three-dimensional vibration/dynamic behavior, static, and buckling behavior of composite structures and to integrate the proposed solution approach with an optimization algorithm to determine the optimum design. In the proposed modeling technique, first order shear deformation theory for two-dimensional modeling and three-dimensional elasticity equations will be used and above-mentioned analyses will be performed using kinetic and strain energies of the composite structure. Since the material properties of composite structures may vary continuously/discontinuously or depend on the direction, the constitutive relationship between strains and stresses needs to be expressed to include all the different material properties specified. Furthermore, to simplify the domain of the boundary value problem, necessary coordinate transformations will be derived to transform the geometries of composite structures having variable curvature along one or two directions. To obtain high accuracy and high computational efficiency in the analyses, a spectral solution technique will be used incorporating Chebyshev polynomials in discretizing the problem domain. The accuracy/precision of developed modeling technique will be validated comparing the results to those obtained through finite element method.

1.6 Thesis organization

The thesis outline is as follows:

The second chapter presents the problem definitions and describes the cases to be analyzed. In this chapter, the material definitions for various types of materials are explained. Since complex geometries are considered, a coordinate transformation is presented to simplify the problem domain. Finally, the 2D and 3D integral boundary value problems are derived to obtain the governing equations.

The third chapter is devoted to developed spectral method based on Chebyshev polynomials to solve the integral boundary value problem. The main elements of the spectral-Chebyshev(ST) approach includes discretization, differentiation and in-

tegral operations. Furthermore, basis recombination approach is described to couple different composite structures and to impose (essential) boundary conditions.

The presented approach is validated and examined in chapter four through various problems defined in chapter two. This chapter includes the vibration, buckling, and static analysis of composite structures. Also, a design study is accomplished for the sandwich structure to obtain an optimized displacement and natural frequency.

In the last chapter, a general conclusion regarding the performance of the developed modeling approach is presented. Furthermore, possible future studies are highlighted. The flowchart of thesis is presented in Fig. 1.3.
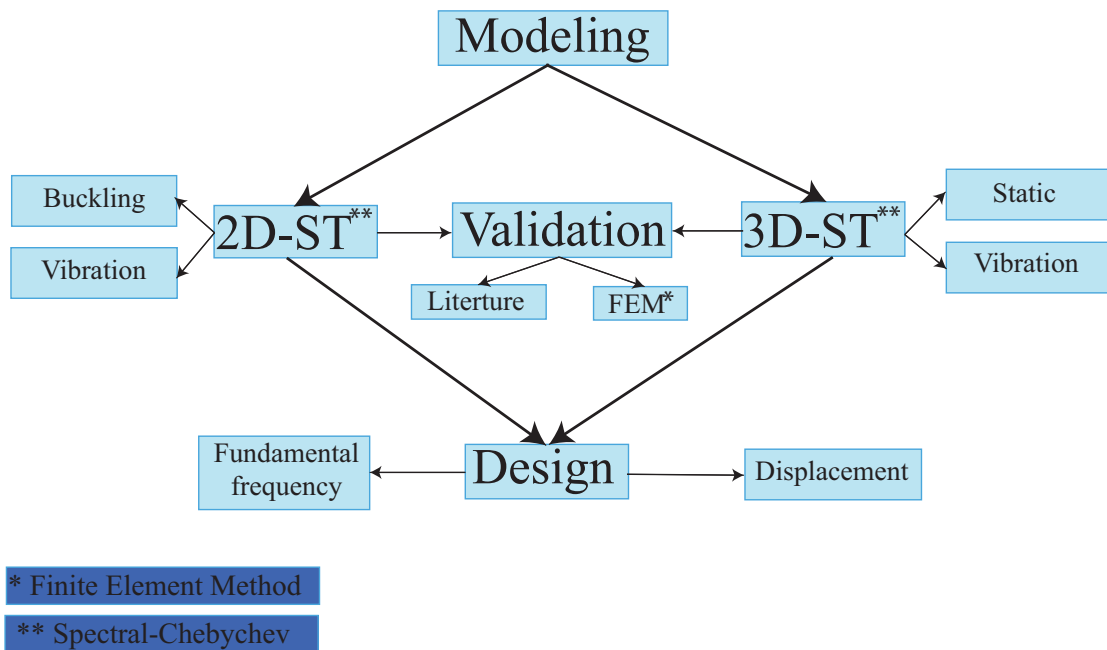
Figure 1.3 Thesis vision.

2.   PROBLEM DEFINITION

2.1 Plate contains graphene platelets and porous media

2.1.1 Boundary value problem

In this study, a multilayer plate model as depicted in Fig. 2.1 is used where the displacement fields are defined based on the first-order shear deformation theory (FSDT) as follows

$$
\begin{aligned}
u(x,y,z,t) &= u_0(x,y,t) + z\phi_x(x,y,t) \\
v(x,y,z,t) &= v_0(x,y,t) + z\phi_y(x,y,t) \\
w(x,y,z,t) &= w_0(x,y,t)
\end{aligned}
\tag{2.1}
$$

Here, u_0, v_0, and w_0 indicate the displacements on the neutral surface along x, y, and z directions, respectively; ϕ_x and ϕ_y represent the rotational movements on $x-z$ and $y-z$ planes, respectively.
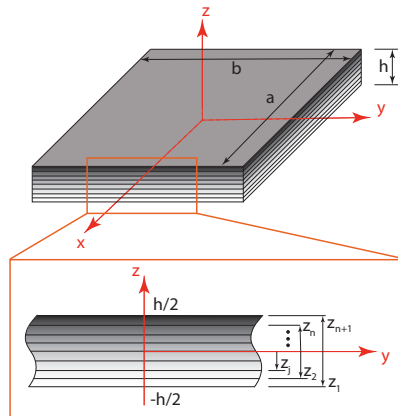
Figure 2.1 Schematic of a multilayer plate.

Considering linear strains, the strain-displacement relations can be written in matrix form as:

$$
\begin{Bmatrix} \epsilon_{xx} \\ \epsilon_{yy} \\ \epsilon_{xy} \\ \epsilon_{xz} \\ \epsilon_{yz} \end{Bmatrix} = \underbrace{\begin{bmatrix} \frac{\partial}{\partial x} & 0 & 0 & z\frac{\partial}{\partial x} & 0 \\ 0 & \frac{\partial}{\partial y} & 0 & 0 & z\frac{\partial}{\partial y} \\ \frac{\partial}{\partial y} & \frac{\partial}{\partial x} & 0 & z\frac{\partial}{\partial y} & z\frac{\partial}{\partial x} \\ 0 & 0 & \frac{\partial}{\partial x} & 1 & 0 \\ 0 & 0 & \frac{\partial}{\partial y} & 0 & 1 \end{bmatrix}}_{\mathbf{B}} \underbrace{\begin{Bmatrix} \mathbf{u_0} \\ \mathbf{v_0} \\ \mathbf{w_0} \\ \phi_x \\ \phi_y \end{Bmatrix}}_{\mathbf{q}}
\tag{2.2}
$$

where $\mathbf{B}$ is the differential operator matrix and $\mathbf{q}$ is the displacement vector. The strain field can also be used to obtain the stresses in the structure using the constitutive matrix, $\mathbf{C}$, as $\boldsymbol{\sigma} = \mathbf{C}\boldsymbol{\epsilon}$. Therefore, using the stresses and the strains, the strain energy can be expressed as

$$
E_s = \frac{1}{2}\int_V \boldsymbol{\epsilon}^{\mathrm{T}}\boldsymbol{\sigma}\,\mathrm{d}V = \frac{1}{2}\int_A\int \mathbf{q}^{\mathrm{T}}\mathbf{B}^{\mathrm{T}}\mathbf{C}\mathbf{B}\mathbf{q}\,\mathrm{d}z\,\mathrm{d}A
\tag{2.3}
$$

The kinetic energy for the plate can be written as

$$
E_k = \frac{1}{2}\int_A\int \rho\dot{\mathbf{q}}^{\mathrm{T}} \underbrace{\begin{bmatrix} 1 & 0 & 0 & 0 & 0 \\ 0 & 1 & 0 & 0 & 0 \\ 0 & 0 & 1 & 0 & 0 \\ 0 & 0 & 0 & z^2 & 0 \\ 0 & 0 & 0 & 0 & z^2 \end{bmatrix}}_{\Upsilon} \dot{\mathbf{q}}\,\mathrm{d}z\,\mathrm{d}A
\tag{2.4}
$$

where ρ is the density and $\dot{\mathbf{q}}$ represent the velocity terms. Lastly, the work done by in-plane stresses (N_{xx} and N_{yy}) can be expressed as

$$
W_{nc} = \frac{1}{2}\int_V \left[N_{xx}\left(\frac{\partial \boldsymbol{w_0}}{\partial x}\right)^2 + N_{yy}\left(\frac{\partial \boldsymbol{w_0}}{\partial y}\right)^2 \right]\mathrm{d}V
\tag{2.5}
$$

Inserting Eqs. (2.3)-(2.5) into Hamilton's equation, the system matrices can be de-

rived as

$$\mathbf{K} = \int_A \int \mathbf{q}^\mathrm{T} \mathbf{B}^\mathrm{T} \mathbf{C} \mathbf{B} \, \delta\mathbf{q} \, \mathrm{d}z \, \mathrm{d}A \tag{2.6}$$

$$\mathbf{M} = \int_A \int \ddot{\mathbf{q}}^\mathrm{T} \rho \, \mathbf{\Upsilon} \, \delta\mathbf{q} \, \mathrm{d}z \, \mathrm{d}A \tag{2.7}$$

$$\mathbf{K_G} = \int_A \int \left[\left(\frac{\partial \boldsymbol{w}_o}{\partial x} \right)^\mathrm{T} N_{xx} \left(\frac{\partial}{\partial x} \delta\boldsymbol{w}_o \right) \right.$$

$$\left. + \left(\frac{\partial \boldsymbol{w}_o}{\partial y} \right)^\mathrm{T} N_{yy} \left(\frac{\partial}{\partial y} \delta\boldsymbol{w}_o \right) \right] \mathrm{d}z \, \mathrm{d}A \tag{2.8}$$

where $\mathbf{M}$, $\mathbf{K}$ and $\mathbf{K_G}$ are the mass, elastic stiffness, and geometric stiffness matrices, respectively. Therefore, to determine the free vibration behavior, the following eigenvalue problem needs to be solved

$$\left[\mathbf{K} - \omega^2 \mathbf{M} \right] \boldsymbol{\psi} = \mathbf{0} \tag{2.9}$$

where ω and $\boldsymbol{\psi}$ represent the natural frequencies and mode shapes of the investigated structure. In the case of (elastic) buckling, the critical buckling load (λ) can be found solving the following eigenvalue problem,

$$\left[\frac{1}{\lambda} \mathbf{K} - \mathbf{K_G} \right] \boldsymbol{\psi} = \mathbf{0} \tag{2.10}$$

2.1.2 Porosity distributions

Figure 2.2 illustrates the symmetric and uniform porosity distributions. The materials properties corresponding to symmetric porosity distribution can be found as

$$\begin{aligned} E(z) &= E^*(z)[1 - e_0 cos(\pi z/h)] \\ G(z) &= G^*(z)[1 - e_0 cos(\pi z/h)] \\ \rho(z) &= \rho^*(z)[1 - e_m cos(\pi z/h)] \end{aligned} \tag{2.11}$$

Similarly, for the uniform porosity distribution, the material properties can be calculated as

$$E(z) = E^*(z)\alpha$$
$$G(z) = G^*(z)\alpha \qquad (2.12)$$
$$\rho(z) = \rho^*(z)\alpha'$$

where $E(z)$, $G(z)$, and $\rho(z)$ defines the variation Young's Modulus, shear modulus, and density of the porous plates along the thickness direction; $E^*(z)$, $G^*(z)$, and $\rho^*(z)$ are the materials properties corresponding to the non-porous case; e_0 and e_m present the porosity coefficients of distribution and mass density, respectively; α and α' are the coefficients for uniform distribution.
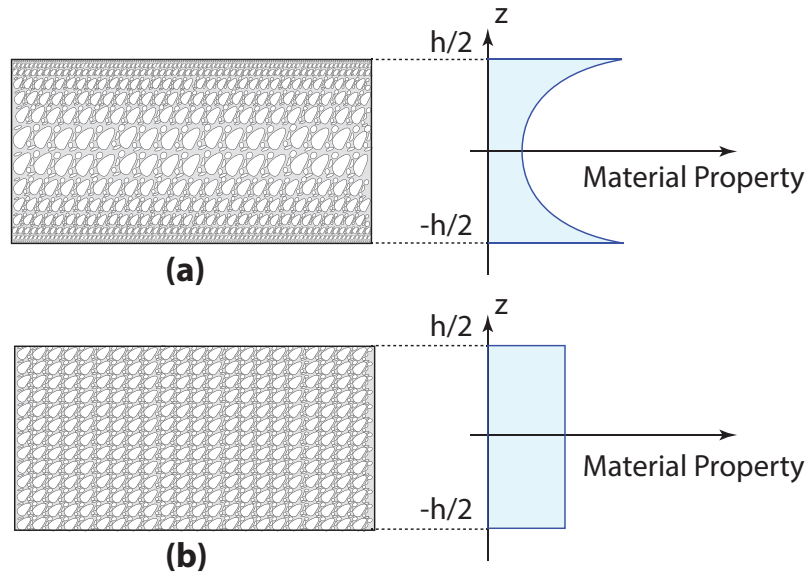
Figure 2.2 **(a)** Symmetric and **(b)** uniform porosity distributions along the thickness direction.

Porosity coefficient, e_0 can be calculated as

$$e_o = 1 - E_1/E_2 \qquad (2.13)$$

where E_1 and E_2 represent the maximum and minimum values of the Young's modulus of the porous plate. The porosity coefficient is proportional to the size and density of pores. As shown in Eqs. (2.11) and (2.12), as the porosity increases, the material properties diminish. The relation between e_0 and e_m is defined as

$$e_m = 1 - \sqrt{1 - e_0} \qquad (2.14)$$

Based on the porosity coefficient, α can be calculated using the theory for open-cell

metal foams:

$$\int_0^{h/2} \sqrt{\alpha}\,\mathrm{d}z = \int_0^{h/2} \sqrt{1 - e_0 \cos(\pi z/h)}\,\mathrm{d}z \tag{2.15}$$

As stated above, the effective stiffness of the material is compromised due to the porosity; thus nanofillers such as CNTs and GPLs can be introduced to improve the strength without a significant increase in the overall weight.

2.1.3 Reinforcing with randomly oriented GPLs

Graphene nanoplatelets (GPLs) are a type of 2D nanofillers that are basically stacks of graphene sheets. In this study, two different distributions for randomly oriented GPL reinforcements are considered as shown in Fig. 2.3. The material properties along the thickness vary and they can be obtained following the Halpin-Tsai micromechanics model as follows [137, 48];

$$E^*(z) = \frac{3}{8}\left(\frac{1 + \zeta_L^{\mathrm{GPL}}\eta_L^{GPL} V_{\mathrm{GPL}}(z)}{1 - \eta_L^{\mathrm{GPL}} V_{\mathrm{GPL}}(z)}\right)E_m$$
$$+ \frac{5}{8}\left(\frac{1 + \zeta_W^{\mathrm{GPL}}\eta_W^{\mathrm{GPL}} V_{\mathrm{GPL}}(z)}{1 - \eta_W^{\mathrm{GPL}} V_{\mathrm{GPL}}(z)}\right)E_m \tag{2.16}$$

$$\nu^*(z) = \nu_{\mathrm{GPL}}V_{\mathrm{GPL}}(z) + \nu_m V_m(z) \tag{2.17}$$

$$\rho^*(z) = \rho_{\mathrm{GPL}}V_{\mathrm{GPL}}(z) + \rho_m V_m(z) \tag{2.18}$$

where E_m, ρ_m and ν_m are the elasticity modulus, density, and Poisson's ratio of matrix material; ρ_{GPL} and ν_{GPL} are the density and Poisson's ratio of GPL, respectively; $V_{\mathrm{GPL}}(z)$ and $V_m(z)$ are the volume of the constituent materials along z direction; ζ_L^{GPL}, ζ_W^{GPL}, η_L^{GPL} and η_W^{GPL} represent the geometric parameters of the GPLs that are defined as;

$$\zeta_L^{\mathrm{GPL}} = 2l_{\mathrm{GPL}}/t_{\mathrm{GPL}} \tag{2.19}$$

$$\zeta_W^{\mathrm{GPL}} = 2w_{\mathrm{GPL}}/t_{\mathrm{GPL}} \tag{2.20}$$

$$\eta_L^{\mathrm{GPL}} = \left(1 - \frac{E_m}{E_{\mathrm{GPL}}}\right)\Big/\left(1 + \zeta_L^{\mathrm{GPL}}\frac{E_m}{E_{\mathrm{GPL}}}\right) \tag{2.21}$$

$$\eta_W^{\mathrm{GPL}} = \left(1 - \frac{E_m}{E_{\mathrm{GPL}}}\right)\Big/\left(1 + \zeta_W^{\mathrm{GPL}}\frac{E_m}{E_{\mathrm{GPL}}}\right) \tag{2.22}$$

Here, l_{GPL}, t_{GPL}, and w_{GPL} represents the length, thickness and width of GPLs, and E_{GPL} is the elasticity modulus of GPLs. The GPL distributions along the thickness
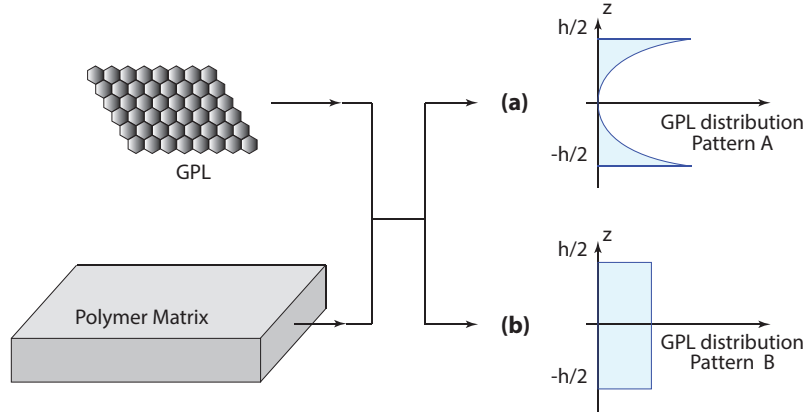
Figure 2.3 **(a)** Symmetric and **(b)** uniform configurations of randomly oriented nanofillers.

corresponding to each distribution, shown in Fig. 2.3, can be found as follows:

$$\text{Pattern A: } V_{\text{GPL}}(z) = A_1\left[1 - \cos\left(\pi z/h\right)\right] \tag{2.23}$$

$$\text{Pattern B: } V_{\text{GPL}} = A_2 \tag{2.24}$$

where A_1 and A_2 can be determined by calculating the total volume of GPLs ($V_{\text{GPL}}^{\text{Tot}}$) in whole structure as

$$V_{\text{GPL}}^{\text{Tot}} = \frac{\Lambda_{\text{GPL}}}{\Lambda_{\text{GPL}} + (\rho_{\text{GPL}}/\rho_m)(1 - \Lambda_{\text{GPL}})} \tag{2.25}$$

$$A_1 = V_{\text{GPL}}^{\text{Tot}} \frac{\sum_{j=1}^{n} \rho_j/\rho^*}{\sum_{j=1}^{n}(1 - \cos(\pi z_j/h))\,\rho(z_j)/\rho^*} \tag{2.26}$$

$$A_2 = V_{\text{GPL}}^{\text{Tot}} \frac{\sum_{j=1}^{n} \rho_j/\rho^*}{\sum_{j=1}^{n} \rho(z_j)/\rho^*} \tag{2.27}$$

where Λ_{GPL} is the weight fraction of GPLs in the plate.

2.2 Laminated structure with functionally graded materials

2.2.1 Structure model

The schematic of a doubly-curved 3D structure having an arbitrary geometry is depicted in Fig. 2.4. Here, x-y-z is the global (inertial) coordinate frame of reference; $B(x,y,z)$ defines the boundary of the 3D structure; and $R_1(\theta_1)$ and $R_2(\theta_2)$ are the vectors that define curvatures around x and y axes, respectively.
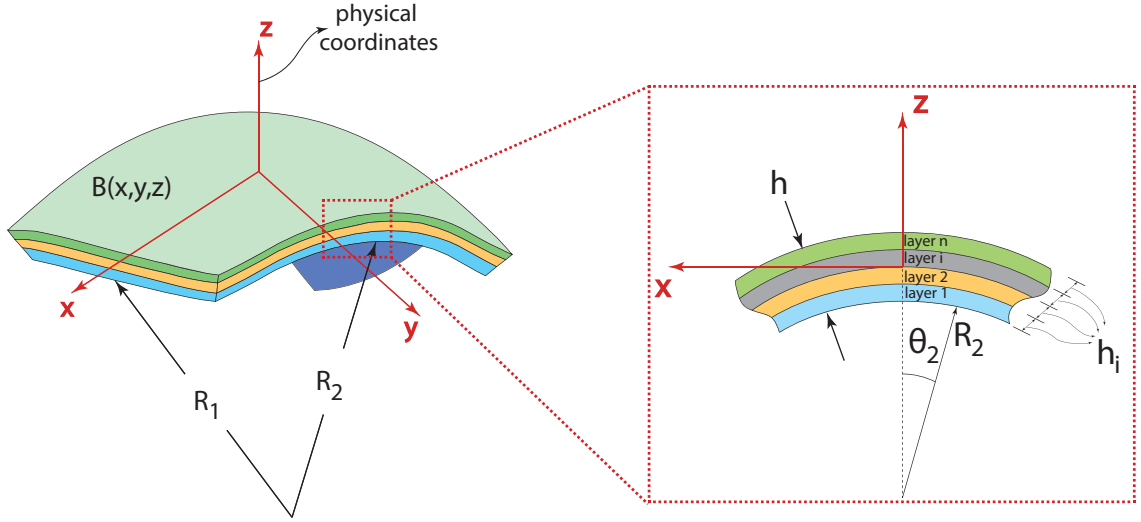
Figure 2.4 Schematic of a doubly-curved laminated composite structure having an arbitrary curved (in-plane) geometry.

To obtain the integral boundary value problem (IBVP) that governs the dynamics of the laminated structures, extended Hamilton's principle is used. Therefore, the IBVP can be derived as;

$$\int_V \left(\rho \ddot{\mathbf{q}}^{\mathrm{T}} \mathbf{q} + \mathbf{q}^{\mathrm{T}} \mathbb{B}^{\mathrm{T}} \mathbf{C} \mathbb{B} \mathbf{q} \right) \mathrm{d}V = \int_V \mathbf{f_q}^{\mathrm{T}} \mathbf{q} \, \mathrm{d}V. \tag{2.28}$$

Here, ρ is the density as a function of spatial variables (x, y, and z), $\mathbf{q} = \{\mathbf{u}; \mathbf{v}; \mathbf{w}\}$ is the deflection vector, $\mathbb{B}$ is the differential operator matrix that relates the displacements (deflections) to strains ($\boldsymbol{\varepsilon} = \mathbb{B} \mathbf{q}$), $\mathbf{C}$ is the constitutive matrix ($\boldsymbol{\sigma} = \mathbf{C} \boldsymbol{\varepsilon}$), and $\mathbf{f_q}$ is the non-conservative forces acting on the structure. Note that the IBVP defined by Eq. (2.28) seems straightforward to solve; however since the integral operation includes varying functions (due to the varying material properties) and is defined over a complicated domain (doubly curved structure with arbitrary geometry), the solution of the IBVP poses significant challenges.

2.2.2 Domain simplification: Coordinate transformations

To address the aforementioned challenges/complexities, in the first step, the domain of the problem is simplified using coordinate transformations and cross-section mapping. Figure 2.5 depicts the flowchart of the domain simplification process. The process starts with mapping the curved geometry onto a straight geometry using two translating (local) coordinate frames, x'-y'-z' and x''-y''-z'' that curl with the curvature around x and y axes (see Fig. 2.5(a)-(c)). Thus, using two rotational

22

transformation matrices consecutively, as follows

$$
\begin{Bmatrix} x \\ y \\ z \end{Bmatrix} = \mathbf{T_x} \begin{Bmatrix} x' \\ R_x \sin(\theta_1) \\ z' - R_x \left[1 - \cos(\theta_1) \right] \end{Bmatrix} \tag{2.29}
$$

$$
\begin{Bmatrix} x' \\ y' \\ z' \end{Bmatrix} = \mathbf{T_y} \begin{Bmatrix} R_y \sin(\theta_2) \\ y'' \\ z'' - R_y \left[1 - \cos(\theta_2) \right] \end{Bmatrix} \tag{2.30}
$$

the doubly curved geometry in Fig. 2.5(a) can be transformed into a straight geometry as depicted in Fig. 2.5(c). Here, $\mathbf{T_x}$ and $\mathbf{T_y}$ are the rotational transformation matrices around x and y axes, respectively; θ_i, is the angle associated with the amount of curvature at any particular location. For instance, considering the rotation around x axis, the angle, θ_1 at any particular location (x') is equal to $\theta_1 = 2\pi\beta y'/L_y$, where β is the curvature rate that quantities the fraction of full revolution. Therefore, it is possible to relate the coordinates of the straight geometry to the coordinates of the curved geometry through the Jacobian matrix, $\mathbb{J}^{\mathrm{CoorM}}$.

$$
\mathrm{d}x\,\mathrm{d}y\,\mathrm{d}z = |\mathbb{J}^{\mathrm{CoorM}}| \,\mathrm{d}x''\,\mathrm{d}y''\,\mathrm{d}z'' \tag{2.31}
$$

where the Jacobian matrix includes the mathematical relationship of the derivatives of Eqs. (2.29)-(2.30) with respect to the coordinates of the straight geometry. Secondly, the complex geometry is mapped onto a simple rectangular geometry defined by the coordinates (ξ and η) using one-to-one cross-section mapping approach [107]. The main steps of the procedure shown in Fig. 2.5(c)-(d) are depicted in Fig. 2.6. To obtain the Jacobian of this cross-section mapping, a polynomial approach is used. In this approach, first, the complex domain defined by x'' and y'' coordinates are discretized; where the number of mapping points are determined based on the order of the mapping functions [138]. Then, a shape function is derived for each mapping point such that the value of the shape function is unity for the corresponding point and zero for all other mapping points.
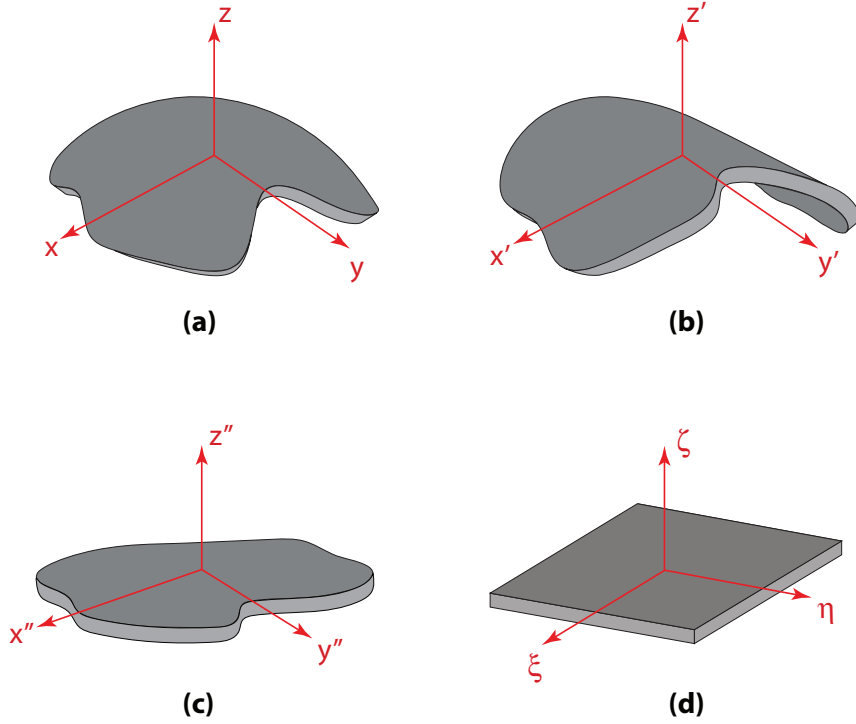
Figure 2.5 Coordinate transformation applied to simplify the primary model: **(a)** doubly-curved structure with arbitrary geometry, **(b)** singly-curved structure with arbitrary geometry, **(c)** straight structure with arbitrary geometry, and **(d)** straight parallelepiped.
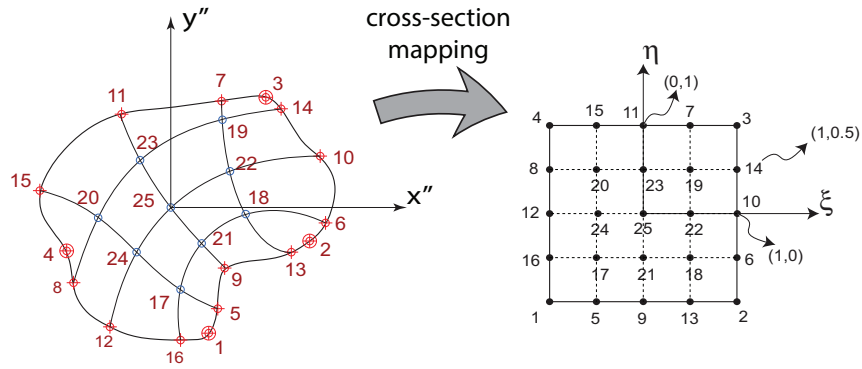
Figure 2.6 Cross-section mapping of arbitrary (in-plane) geometry to a square cross-section.

Using the shape functions defined for the mapping points, the derivatives of these functions respect to the coordinates (ξ and η) in the simplified domain can be calculated to determine the Jacobian matrix, $\mathbb{J}^{\text{CrossM}}$, that relates the physical coordinates (x'' and y'') to the mapped coordinates (ξ and η) as follows

$$\frac{\partial}{\partial q_j} = \sum_{i=1}^{3} \left(\mathbb{J}^{\text{CrossM}}_{ij} \right)^{-1} \frac{\partial}{\partial \epsilon_i} . \tag{2.32}$$

where q and ϵ represent the physical domain and mapped domain coordinates, respectively.

Finally, using the Jacobian of the coordinate transformations defined by Eqs. (2.29)-(2.30) and the Jacobian of cross-section mapping, the physical coordinates of the original doubly-curved structure can be related to the mapped coordinates (ξ and η)

$$\mathrm{d}x\,\mathrm{d}y\,\mathrm{d}z = \underbrace{|\mathbb{J}^{\mathrm{CrossM}}|\,|\mathbb{J}^{\mathrm{CoorM}}|}_{\mathbb{J}}\,\mathrm{d}\xi\,\mathrm{d}\eta\,\mathrm{d}\zeta \tag{2.33}$$

Note that this mathematical relationship increases the computational complexity of the problem; however, more importantly, it simplifies the domain of the IBVP and the calculation of the integral operations given by Eq. (2.28).

2.2.3 Functionally graded materials

Another challenge aforementioned above is the variation of the material properties within the 3D structure. The material distribution can be defined three-dimensionally; however in this study, uni-directional (that the material gradation is only along the one direction) case is considered.

The varying material properties (such as density, Young's Modulus, *etc.*) in FGM structures are based on the volume fraction distributions and thereby the properties of the constituent materials. In literature, two common approaches are used to model the varying material properties: **(i)** Mori-Tanaka [26, 139] and **(ii)** theory of mixtures [14, 83]. For both methods, first, the volume fraction of the material constituents needs to be calculated using methods such as power law or exponential methods. In this study, the volume fractions for an FGM having uni-directional material gradation are calculated using the power law approach as

$$V_c(y,z) = \left(\frac{1}{2} + \frac{z}{h}\right)^p \tag{2.34}$$

$$V_m(y,z) = 1 - V_c \tag{2.35}$$

where V_c is the volume fraction of the particulate phase (added material) and V_m is the volume fraction of the matrix phase; p is the gradation parameter along the z axis.

Based on the volume fractions, the varying material properties can be calculated

using either the Mori-Tanaka method or theory of mixture. In the method of theory of mixture, the material property of the FGM structure is basically the linear combination of the mechanical properties of the constituent materials [14]. However, for the Mori-Tanaka method, the effective material properties are found using the effective local bulk and shear moduli of the FGM calculated using the technique described in [21, 107].

2.3 Sandwich structure with carbon nanotube face-sheets and honeycomb core

2.3.1 Model development

The schematic of the (curved) sandwich-structured composite is depicted in Fig. 2.7. A hexagonal type of honeycomb layer, having a thickness of h_m, is used as the core layer (see Fig. 2.7(b) with detailed geometry properties of the hexagonal type of honeycomb structure); and the top and bottom layers (*i.e.* face-sheets), having a thickness of h_o, are composed of a porous matrix reinforced with CNTs. The curvature of the structure is defined by either the radius of curvature (R) that is measured from the mid-plane of the structure or angle of the curvature (Θ). The curvature amount (β), that quantifies the number (or fraction) of full revolution along the specified direction, can be defined to calculate the curvature radius as $R = L/(2\pi\beta)$ where L is the length of the structure along x or y axis. Lastly, a distributed line force (F) is applied on the edge of the top layer along ($-z$) direction as shown in Fig. 2.7a. It should be noticed that the domain of this structure is simplified using the transformation approach described in section. 2.2.2.

2.3.2 Material definition

2.3.2.1 Honeycomb

In this study, the hexagonal honeycomb structure with double thickness walls as depicted in Fig. 2.7(b) is used as the core layer of the sandwich-structured composite.
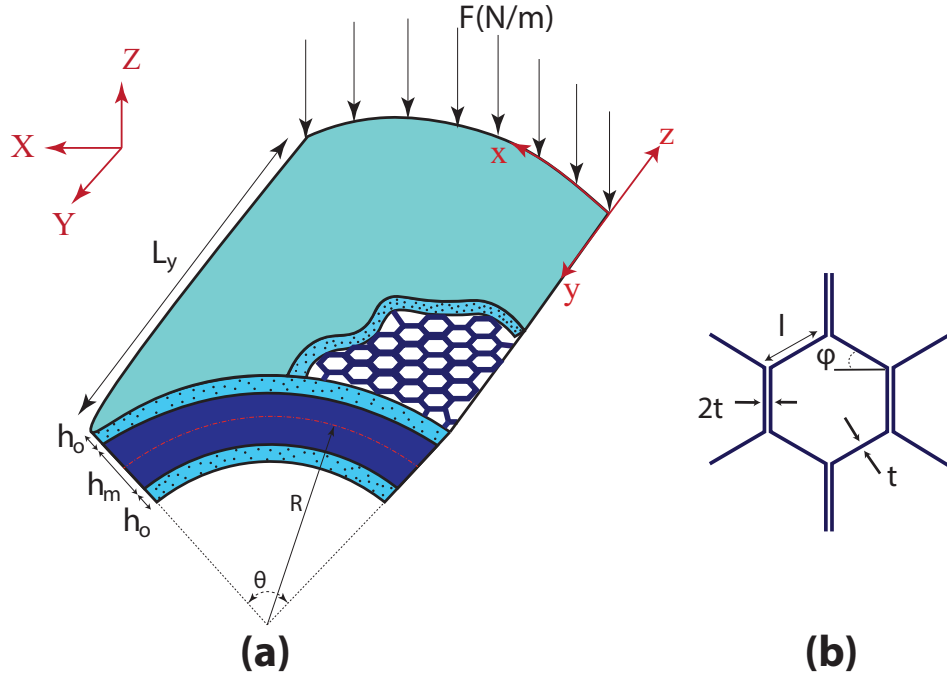
Figure 2.7 **(a)** Schematic of the sandwich-structured composite with CNT-reinforced face-sheets and a honeycomb core. **(b)** Detailed geometry of the hexagonal type of honeycomb structure.

Based on the study of Kelsey et al. [140], out-of-plane shear stiffness and density values can be obtained as;

$$G_{13} = \frac{\delta \cos \varphi}{1 + \sin \varphi} G_s \qquad (2.36)$$

$$\rho = \frac{2\delta}{(1 + \sin \varphi) \cos \varphi} \rho_s \qquad (2.37)$$

where δ is the ratio of thickness to the length of hexagonal geometry (t/l), φ is the honeycomb angle, G_s and ρ_s are the shear and density of the honeycomb material, respectively. In continue, Sun et al. purpose that the direct stiffness of the honeycomb core is proportional to its density [141] and can be presented as;

$$E_{33} = \frac{2\delta}{(1 + \sin \varphi) \cos \varphi} E_s \qquad (2.38)$$

Also, Klintworth and Strong [142] present the equations to obtain the elasticity modulus in other directions;

$$E_{11} = \frac{\delta^3 \cos\varphi}{(1+\sin\varphi)\sin^2\varphi} E_s \qquad (2.39)$$

$$E_{22} = \frac{\delta^3(1+\sin\varphi)}{\cos^3\varphi} E_s \qquad (2.40)$$

$$G_{12} = \frac{\delta^3(1+\sin\varphi)}{\cos\varphi} \qquad (2.41)$$

where E_s is the hexagonal honeycomb core elasticity modulus. The accurate in-plane poisson's ratio is a function of hexagonal honeycomb core poisson's ratio (ν_s) presented by Scarp and Tomlinson [143] as;

$$\nu_{12} = \frac{\cos^2\varphi}{(1+\sin\varphi)\sin\varphi}\left[\frac{1+(1.4+1.5\nu_s)\delta^2}{1+(2.4+1.5\nu_s+\cot^2\varphi)\delta^2}\right] \qquad (2.42)$$

Grediac approximates the other out-of-plane shear modulus [144];

$$G_{23} = \left[\frac{1+\sin\varphi}{2\cos\varphi} + 0.787\frac{1+\sin^2\varphi}{(1+\sin\varphi)\cos\varphi}(\frac{l}{h})\right]\delta G_s \qquad (2.43)$$

Also, Zhang and Ashby calculated the out-of-plane poisson's ratios as [145];

$$\nu_{31} = \nu_{32} = \nu_s \qquad (2.44)$$

$$\nu_{13} = \frac{E_{11}}{E_{33}}\nu_{31} \approx 0 \qquad (2.45)$$

$$\nu_{23} = \frac{E_{22}}{E_{33}}\nu_{32} \approx 0 \qquad (2.46)$$

2.3.2.2 Face-sheets

In this section, porosity and CNTs distributions along the thickness of the face-sheets and honeycomb type of structure are described. Four different CNTs distributions

along the thickness of the face-sheets are used as shown in Fig. 2.8;

$$V_{\mathrm{cnt}} = V_{\mathrm{cnt}}^* \qquad UD$$
$$V_{\mathrm{cnt}} = (1 + 2\frac{z}{h})V_{\mathrm{cnt}}^* \quad FG - V$$
$$V_{\mathrm{cnt}} = 2(1 - 2\frac{|z|}{h})V_{\mathrm{cnt}}^* \quad FG - O \tag{2.47}$$
$$V_{\mathrm{cnt}} = (4\frac{|z|}{h})V_{\mathrm{cnt}}^* \quad FG - X$$

where V_{CNT} defines the contained volume of CNTs in thicknesses direction and V_{CNT}^* is the total volume contained of CNTs in each layer;

$$V_{\mathrm{CNT}}^* = \frac{w_{\mathrm{CNT}}}{w_{\mathrm{CNT}} + (\rho_{\mathrm{CNT}}/\rho_{\mathrm{m}}) - (\rho_{\mathrm{CNT}}/\rho_{\mathrm{m}})w_{\mathrm{CNT}}} \tag{2.48}$$

where w_{CNT} is the mass fraction of CNTs in the layer, ρ_{m} and ρ_{CNT} are the matrix
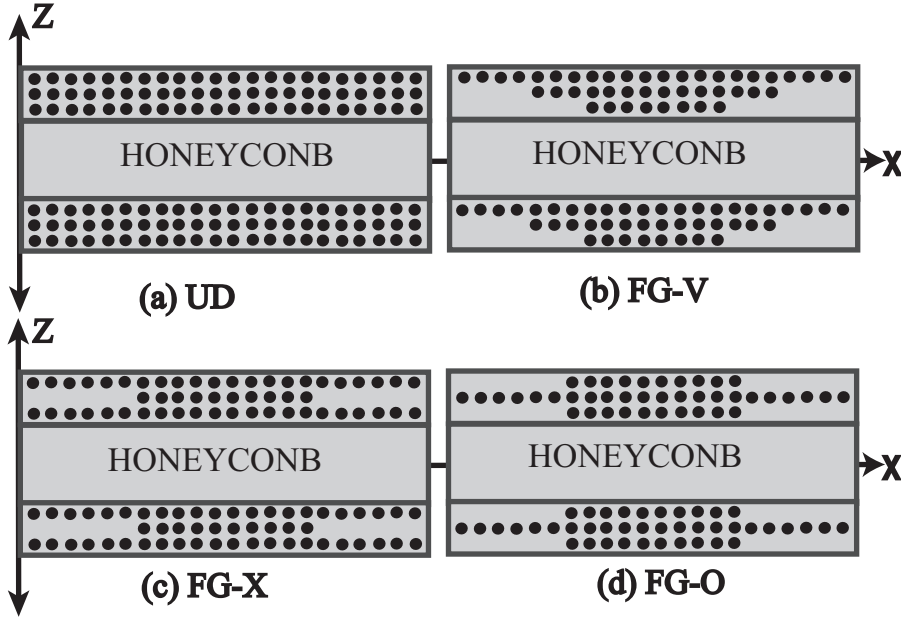
Figure 2.8 CNT distribution along the thickness of each face-sheets with honeycomb core; (a) Uniform, (b) FG-V, (c) FG-X, (d) FG-O.

and CNTs densities, respectively. However, the effective material properties of face-sheets can be determined using the matrix and CNTs material properties;

$$E_{11}^* = \eta_1 V_{\mathrm{CNT}} E_{11}^{\mathrm{CNT}} + V_m E^{\mathrm{m}}$$
$$\frac{\eta_2}{E_{22}^*} = \frac{V_{\mathrm{CNT}}}{E_{22}^{\mathrm{CNT}}} + \frac{V_{\mathrm{m}}}{E^{\mathrm{m}}} \tag{2.49}$$
$$\frac{\eta_3}{G_{12}^*} = \frac{V_{\mathrm{CNT}}}{G_{12}^{\mathrm{CNT}}} + \frac{V_{\mathrm{m}}}{G^{\mathrm{m}}}$$

29

where E_{11}^{CNT}, E_{22}^{CNT}, and G_{12}^{CNT} corresponds to the elasticity and shear modulus of CNTs. Also, E^{m} and G^{m} are the elasticity and shear modulus of the matrix part of the CNTs, respectively. η_i (i=1,2,3) are the CNTs efficiency parameters. Poisson ratio and density properties of face-sheets can be obtained as;

$$\nu_{12} = V_{\text{CNT}}^* \nu_{12}^{\text{CNT}} + V_{\text{m}} \nu^{\text{m}}$$
$$\rho = V_{\text{CNT}} \rho^{\text{CNT}} + V_{\text{m}} \rho^{\text{m}} \tag{2.50}$$

where, $\nu_1 2^{\text{CNT}}$ and nu^{m} are the poisson's ratios of CNT and matrix parts of face-sheet, respectively. ρ^{CNT} and ρ^{m} are the CNT and matrix parts' densities, respectively. The CNTs composite including the CNTs particles and matrix part is distributed in the porous media in which the media's distribution (P_{dist}) along the thickness is specified as;

$$P_{\text{symm}} = 1 - e_0 cos(\frac{\pi z}{h_o}) \tag{2.51}$$

where e_0 is the porosity parameter. It should be noticed that Eq. (2.51) is defined for the mechanical property variation of the material along the thickness; where, for the density distribution, e_0 should be replaced with e_m(porosity mass parameter, $e_m = 1 - \sqrt{1 - e_0}$). Consequently, the face-sheet material properties can be obtained as;

$$\begin{cases} E_{ii} = E_{ii}^* \times P_{\text{symm}} \\ G_{ij} = G_{ij}^* \times P_{\text{symm}} \quad \text{Symmetric porosity distribution}, i,j = 1,2,3 \\ \rho = \rho^* \times P_{\text{symm}} \end{cases} \tag{2.52}$$

2.3.3 Governing equations

To study the sandwich structure's dynamic and static behavior, the system's integral boundary value problem (IBVP) is obtained using the Hamilton approach as written in equation. 2.28. It should be noticed that the constitutive matrix C contains the

30

transformed material properties of the face-sheets as[146];

$$C = T \begin{bmatrix} Q_{11} & Q_{12} & Q_{13} & 0 & 0 & 0 \\ Q_{12} & Q_{22} & Q_{23} & 0 & 0 & 0 \\ Q_{13} & Q_{23} & Q_{33} & 0 & 0 & 0 \\ 0 & 0 & 0 & Q_{44} & 0 & 0 \\ 0 & 0 & 0 & 0 & Q_{55} & 0 \\ 0 & 0 & 0 & 0 & 0 & Q_{66} \end{bmatrix} T' \tag{2.53}$$

$$T = \begin{bmatrix} \cos^2(\psi) & \sin^2(\psi) & 0 & 0 & 0 & \sin(\psi)\cos(\psi) \\ \sin^2(\psi) & \cos^2(\psi) & 0 & 0 & 0 & -\sin(\psi)\cos(\psi) \\ 0 & 0 & 1 & 0 & 0 & 0 \\ 0 & 0 & 0 & \cos(\psi) & -\sin(\psi) & 0 \\ 0 & 0 & 0 & \sin(\psi) & \cos(\psi) & 0 \\ -\sin(2\psi) & \sin(2\psi) & 0 & 0 & 0 & \cos^2(\psi)-\sin^2(\psi) \end{bmatrix} \tag{2.54}$$

The ψ is the CNTs orientations. The system matrices can be obtained;

$$M = \int_V \rho \, dV \tag{2.55}$$

$$K = \int_V \mathbb{B}^{\mathrm{T}} C \mathbb{B} \, dV \tag{2.56}$$

where M and K are the stiffness and mass matrices of the problem, respectively.

3.   SOLUTION OF GOVERNING EQUATIONS

3.1 Two dimensional spectral-Chebyshev solution

To numerically calculate the vibration and buckling behavior, the continuous deflection functions need to be represented by a vector sampled at certain increments in the domain. For sampling the domain, Gauss-Lobatto sampling is used to minimize the interpolation error. Since, the problem domain forms a 2D space, the sampling of deformations along x and y directions will lead to a second rank tensor as $q_{ij} = q(x(i), y(j))$. However, for numerical purposes, the following mapping algorithm is used

$$q_k = q_{ij} , \quad k = (i-1)N_y + j \tag{3.1}$$

to obtain the deflections as a vector where $i, j = 1, \ldots, N_x$ or N_y. The deflection at any point (x, y) can be expressed as double expansion of Chebychev polynomials

$$q_k = \sum_{i=1}^{N_x} \sum_{j=1}^{N_y} a_{q_k} T_{i-1}(x) T_{j-1}(y) \tag{3.2}$$

where T's are the Chebychev polynomials (of the first kind), a's are the coefficients of expansion, N_x and N_y are the number of polynomials used for expansion along x and y directions, respectively. The (sampled) deflection vectors can be written as

$$\begin{aligned}
\mathbf{u}_o &= [\mathbb{I}\,\mathbb{O}\,\mathbb{O}\,\mathbb{O}\,\mathbb{O}] = \mathbb{I}_{\boldsymbol{u_o}}\mathbf{q} \\
\mathbf{v}_o &= [\mathbb{O}\,\mathbb{I}\,\mathbb{O}\,\mathbb{O}\,\mathbb{O}] = \mathbb{I}_{\boldsymbol{v_o}}\mathbf{q} \\
\mathbf{w}_o &= [\mathbb{O}\,\mathbb{O}\,\mathbb{I}\,\mathbb{O}\,\mathbb{O}] = \mathbb{I}_{\boldsymbol{w_o}}\mathbf{q} \\
\boldsymbol{\phi}_x &= [\mathbb{O}\,\mathbb{O}\,\mathbb{O}\,\mathbb{I}\,\mathbb{O}] = \mathbb{I}_{\boldsymbol{\phi_x}}\mathbf{q} \\
\boldsymbol{\phi}_y &= [\mathbb{O}\,\mathbb{O}\,\mathbb{O}\,\mathbb{O}\,\mathbb{I}] = \mathbb{I}_{\boldsymbol{\phi_y}}\mathbf{q}
\end{aligned} \tag{3.3}$$

where $\mathbb{I}$ and $\mathbb{O}$ are $(N_x N_y \times N_x N_y)$ zero and identity matrices, respectively. It is possible to relate the sampled function's values to the coefficients of expansion as $\mathbf{q} = \boldsymbol{\Gamma}_B \mathbf{a}$ or $\mathbf{a} = \boldsymbol{\Gamma}_F \mathbf{q}$, where $\boldsymbol{\Gamma}_B$ and $\boldsymbol{\Gamma}_F$ are $(N_x N_y \times N_x N_y)$ extended backward and forward transformation matrices $(\boldsymbol{\Gamma}_B \boldsymbol{\Gamma}_F = \mathbf{I})$. These extended transformation matrices can be derived using the forward and backward transformation matrices obtained using the one-dimensional expansion for each direction as $\Gamma^{q_t}_{B_{ij}} = T_{j-1}(q_{t_i})$ where $i, j = 1, \ldots, N_{q_t}$ and $t = 1, 2$ (*i.e.* $q_1 = x$ and $q_2 = y$) [108, 107]. Thus, using the mapping algorithm defined in Eq. (3.1), extended transformation matrices can be calculated as

$$\Gamma_{B_{k_1 k_2}} = \Gamma^x_{B_{i_1 i_2}} \Gamma^y_{B_{j_1 j_2}} \tag{3.4}$$
$$k_1 = (i_1 - 1) N_y + j_1, \ \ k_2 = (i_2 - 1) N_y + j_2$$
$$i_1, i_2 = 1, \ldots, N_x, \ \ j_1, j_2 = 1, \ldots, N_y$$

To perform the derivative operations in Eqs. (2.6)-(2.8), differentiation matrices ($\mathbf{Q}_x$ and $\mathbf{Q}_y$) need to be determined. Using the recursive polynomial form of the Chebychev polynomials, it is possible to obtain a relationship between the coefficients of expansion of a function and its derivative as $\mathbf{b} = \mathbf{D}^{q_t} \mathbf{a}$, where b's are the coefficients of expansion of the function's derivative and $\mathbf{D}^{q_t}$ is $(N_{q_t} \times N_{q_t})$ derivative matrix. Using Eq. (3.4), the derivative matrices calculated for x and y variable can be extended for a two-dimensional function to obtain $(N_x N_y \times N_x N_y)$ extended derivative matrices, $\mathbb{D}^{\mathbf{q_t}}$. Note that these derivative matrices are defined between the coefficients of the expansion; however, it is required to apply the derivative operation to the function values. Thus, using the extended forward and backward transformation matrices, the derivative of the deflection vector with respect to x and y can be calculated as follows

$$\frac{\partial q}{\partial q_t} = \boldsymbol{\Gamma}_{\mathbf{B}} \mathbf{b} = \boldsymbol{\Gamma}_{\mathbf{B}} \mathbb{D}^{\mathbf{q_t}} \mathbf{a} = \boldsymbol{\Gamma}_{\mathbf{B}} \mathbb{D}^{\mathbf{q_t}} \boldsymbol{\Gamma}_{\mathbf{F}} \mathbf{q} = \mathbf{Q}_{\mathbf{q_t}} \mathbf{q} \tag{3.5}$$

where, $\mathbf{Q}_{\mathbf{q_t}}$ is the differentiation matrix.

To obtain the system matrices in Eqs. (2.6)-(2.8), we need to perform integral operations. Similar to the derivation operation described above, first the inner product matrix, $\mathbf{V}^{\mathbf{q_t}}$, for each individual direction needs to be determined [108]. Then, using the mapping algorithm as in Eq. (3.4), the extended inner product matrix, $\mathbb{V}$, can be derived [147].

After finding the differentiation and inner product matrices, the system matrices

(mass, elastic stiffness and geometric stiffness matrices), can be obtained as follows:

$$
\begin{aligned}
\mathbf{K} =& h\Bigg[C_{11}\mathbb{I}_{u_o}^{\mathrm{T}}\,\mathbf{Q}_x^{\mathrm{T}}\mathbf{V}\mathbf{Q}_x\mathbb{I}_{u_o} + C_{12}\mathbb{I}_{u_o}^{\mathrm{T}}\,\mathbf{Q}_x^{\mathrm{T}}\mathbf{V}\mathbf{Q}_y\mathbb{I}_{v_o} + C_{21}\mathbb{I}_{v_o}^{\mathrm{T}}\,\mathbf{Q}_y^{\mathrm{T}}\mathbf{V}\mathbf{Q}_x\mathbb{I}_{u_o} + C_{22}\mathbb{I}_{v_o}^{\mathrm{T}}\,\mathbf{Q}_y^{\mathrm{T}}\mathbf{V}\mathbf{Q}_y\mathbb{I}_{v_o} \\[4pt]
&+ C_{33}\mathbb{I}_{u_o}^{\mathrm{T}}\,\mathbf{Q}_y^{\mathrm{T}}\mathbf{V}\mathbf{Q}_y\mathbb{I}_{u_o} + C_{33}\mathbb{I}_{u_o}^{\mathrm{T}}\,\mathbf{Q}_y^{\mathrm{T}}\mathbf{V}\mathbf{Q}_x\mathbb{I}_{v_o} + C_{33}\mathbb{I}_{v_o}^{\mathrm{T}}\,\mathbf{Q}_x^{\mathrm{T}}\mathbf{V}\mathbf{Q}_y\mathbb{I}_{u_o} + C_{33}\mathbb{I}_{v_o}^{\mathrm{T}}\,\mathbf{Q}_x^{\mathrm{T}}\mathbf{V}\mathbf{Q}_x\mathbb{I}_{v_o} \\[4pt]
&+ C_{44}\mathbb{I}_{w_o}^{\mathrm{T}}\,\mathbf{Q}_x^{\mathrm{T}}\mathbf{V}\mathbf{Q}_x\mathbb{I}_{w_o} + C_{44}\mathbb{I}_{w_o}^{\mathrm{T}}\,\mathbf{Q}_x^{\mathrm{T}}\mathbf{V}\mathbb{I}_{\phi_x} + C_{44}\mathbb{I}_{\phi_x}^{\mathrm{T}}\,\mathbf{V}\mathbf{Q}_x\mathbb{I}_{w_o} + C_{44}\mathbb{I}_{\phi_x}^{\mathrm{T}}\,\mathbf{V}\mathbb{I}_{\phi_x} \\[4pt]
&+ C_{55}\mathbb{I}_{w_o}^{\mathrm{T}}\,\mathbf{Q}_y^{\mathrm{T}}\mathbf{V}\mathbf{Q}_y\mathbb{I}_{w_o} + C_{55}\mathbb{I}_{w_o}^{\mathrm{T}}\,\mathbf{Q}_y^{\mathrm{T}}\mathbf{V}\mathbb{I}_{\phi_y} + C_{55}\mathbb{I}_{\phi_y}^{\mathrm{T}}\,\mathbf{V}\mathbf{Q}_y\mathbb{I}_{w_o} + C_{55}\mathbb{I}_{\phi_y}^{\mathrm{T}}\,\mathbf{V}\mathbb{I}_{\phi_y}\Bigg] + \\[8pt]
&\frac{h^3}{12}\Bigg[C_{11}\mathbb{I}_{\phi_x}^{\mathrm{T}}\,\mathbf{Q}_x^{\mathrm{T}}\mathbf{V}\mathbf{Q}_x\mathbb{I}_{\phi_x} + C_{12}\mathbb{I}_{\phi_x}^{\mathrm{T}}\,\mathbf{Q}_x^{\mathrm{T}}\mathbf{V}\mathbf{Q}_y\mathbb{I}_{\phi_y} + C_{21}\mathbb{I}_{\phi_y}^{\mathrm{T}}\,\mathbf{Q}_y^{\mathrm{T}}\mathbf{V}\mathbf{Q}_x\mathbb{I}_{\phi_x} + C_{22}\mathbb{I}_{\phi_y}^{\mathrm{T}}\,\mathbf{Q}_y^{\mathrm{T}}\mathbf{V}\mathbf{Q}_y\mathbb{I}_{\phi_y} \\[4pt]
&+ C_{33}\mathbb{I}_{\phi_x}^{\mathrm{T}}\,\mathbf{Q}_y^{\mathrm{T}}\mathbf{V}\mathbf{Q}_y\mathbb{I}_{\phi_x} + C_{33}\mathbb{I}_{\phi_x}^{\mathrm{T}}\,\mathbf{Q}_y^{\mathrm{T}}\mathbf{V}\mathbf{Q}_x\mathbb{I}_{\phi_y} + C_{33}\mathbb{I}_{\phi_y}^{\mathrm{T}}\,\mathbf{Q}_x^{\mathrm{T}}\mathbf{V}\mathbf{Q}_y\mathbb{I}_{\phi_x} + C_{33}\mathbb{I}_{\phi_y}^{\mathrm{T}}\,\mathbf{Q}_x^{\mathrm{T}}\mathbf{V}\mathbf{Q}_x\mathbb{I}_{\phi_y}\Bigg]
\end{aligned}
\tag{3.6}
$$

$$
\mathbf{M} = \rho h\left(\mathbb{I}_{u_o}^{\mathrm{T}}\,\mathbf{V}\mathbb{I}_{u_o} + \mathbb{I}_{v_o}^{\mathrm{T}}\,\mathbf{V}\mathbb{I}_{v_o} + \mathbb{I}_{w_o}^{\mathrm{T}}\,\mathbf{V}\mathbb{I}_{w_o}\right) + \rho\frac{h^3}{12}\left(\mathbb{I}_{\phi_x}^{\mathrm{T}}\,\mathbf{V}\mathbb{I}_{\phi_x} + \mathbb{I}_{\phi_y}^{\mathrm{T}}\,\mathbf{V}\mathbb{I}_{\phi_y}\right) \tag{3.7}
$$

$$
\mathbf{K}_G = h\left(\mathbb{I}_{w_o}^{\mathrm{T}}\mathbf{Q}_x^{\mathrm{T}} N_{xx}\mathbf{V}\mathbf{Q}_x\mathbb{I}_{w_o} + \mathbb{I}_{w_o}^{\mathrm{T}}\mathbf{Q}_y^{\mathrm{T}} N_{yy}\mathbf{V}\mathbf{Q}_y\mathbb{I}_{w_o}\right) \tag{3.8}
$$

The system matrices that are evaluated by applying the area integrals as shown in Eqs. (3.6)-(3.8), corresponds to a plate whose mid-surface is its neutral surface (note that the integral operation along the thickness is evaluated analytically and the results are placed as constants in area integral calculations). However, to accurately capture the varying material properties along the thickness direction, a multilayer plate approach is used. In this approach, the plate is divided into n number of layers having the same thickness (see Fig. 2.1). It is assumed that each layer is made from an isotropic porous matrix and nanofillers; however the porosity amount and the weight fraction of the nanofillers varies from layer to layer. In other words, each layer has different material properties based on the gradation amount. Furthermore, the integral operation along the z direction has different limits for each layer based on the distance of the individual layer to the neutral surface of the composite plate. Therefore, the overall system matrices can be obtained using the superposition method. For instance, the overall stiffness matrix can be calculated as

$$
\mathbf{K} = \sum_{l=1}^{n}\int_A\int_{z_l}^{z_{l+1}}\mathbf{q}^{\mathrm{T}}\mathbf{B}^{\mathrm{T}}\mathbf{C}\mathbf{B}\,\delta\mathbf{q}\,\mathrm{d}z\,\mathrm{d}A \tag{3.9}
$$

3.2 Three dimensional spectral-Chebyshev solution

The three dimensional deformations in the FGM structure can be expressed as a summation of triple expansion of Chebychev polynomials as

$$q(\xi,\eta,\zeta) = \sum_{l=1}^{\infty}\sum_{m=1}^{\infty}\sum_{n=1}^{\infty} a_i T_{l-1}(\xi) T_{m-1}(\eta) T_{n-1}(\zeta) \tag{3.10}$$

where T's represent the orthogonal Chebychev polynomials, and a's are the coefficients of the polynomial expansion (that decay exponentially with increasing i value [148]).

For numerical calculations, the continuous deflection function needs to be discretized (which leads to finite summation in the expansion process). Thus, using the Gauss-Lobatto sampling [149] algorithm, the continuous deflection function is represented by a third rank tensor as follows

$$q_{lmn} = q(\xi(l),\eta(m),\zeta(n)) \tag{3.11}$$

Here, $l = 1,\ldots,N_\xi$, $m = 1,\ldots,N_\eta$, and $n = 1,\ldots,N_\zeta$ are the indices of the tensor; N_ξ, N_η, and N_ζ are the polynomial numbers used in ξ, η, and ζ directions, respectively. To transform this third rank tensor to a vector, a mapping algorithm as follows

$$q_i = f_{lmn}, \quad i = (l-1)N_\eta N_\zeta + (m-1)N_\zeta + n. \tag{3.12}$$

is used. Then, we can write a relationship between the vector of the sampled deflection function ($\mathbf{q}$) and the coefficients of expansion ($\mathbf{a}$) through either extended forward ($\mathbf{\Gamma_F}$) or backward ($\mathbf{\Gamma_B}$) transformation matrices

$$\mathbf{q} = \mathbf{\Gamma_B a}, \quad \text{or} \quad \mathbf{a} = \mathbf{\Gamma_F q}, \tag{3.13}$$

whose sizes are $N_\xi N_\eta N_\zeta \times N_\xi N_\eta N_\zeta$, and are obtained using the forward/backward matrices defined for each direction as $\Gamma_{B_{ij}}^{qt} = T_{j-1}(q_{k_i})$. Thus, using the mapping algorithm defined by Eq. (3.12), the extended forward/backward matrices can be obtained using the individual forward/backward matrices having a size of $N_{q_i} \times N_{q_i}$[150].

After simplifying the domain, calculating the functions for the varying material properties and discretizing the domain using Chebychev polynomials, the IBVP given in Eq. (2.28) can be rewritten for the free vibrations of a lamina as

$$\int_{\mathbb{V}} \left(\mathbf{\Upsilon} \ddot{\mathbf{q}}^{\mathrm{T}} \hat{\mathbf{q}} + \mathbf{q}^{\mathrm{T}} \mathbf{B}^{\mathrm{T}} \mathbf{C} \mathbf{B} \hat{\mathbf{q}} \right) |\mathbb{J}| \, \mathrm{d}\xi \, \mathrm{d}\eta \, \mathrm{d}\zeta = 0. \tag{3.14}$$

Here, $\mathbf{\Upsilon}$ and $\mathbf{C}$ are the matrices that includes the varying density, and Young's

Modulus and Poisson's ratio, respectively, that are evaluated at the sampling points. To solve this equation, the derivative operations inside the differential operator matrix, $\mathbf{B}$, and the volume integral operations should be evaluated considering the varying material properties.

To calculate the spatial derivatives of the 3D deflection vector, differential matrices ($\mathbf{Q_{q_i}}$) are needed. To address this issue, first, the spatial derivative operations, $\mathbf{D^{q_i}}$, for each direction are defined. Since the derivative of the deflection function can also be expressed as a summation Chebychev polynomials with different expansion coefficients, we can formulate a relationship between the coefficients of the derivative of the original function ($\mathbf{b}$) and the original function ($\mathbf{a}$) as $\mathbf{b} = \mathbf{D}^{q_i}\mathbf{a}$. Secondly, using the same mapping algorithm as in the backward/forward matrices, the extended derivative matrices ($\mathbb{D}^{\mathbf{q_i}}$) with respect to each direction, q_i, can be obtained. Finally, the required ($N_\xi N_\eta N_\zeta \times N_\xi N_\eta N_\zeta$) dimensional differential matrices ($\mathbf{Q_{q_i}}$) can be derived as follows

$$\frac{\partial f}{\partial q_i} = \mathbf{\Gamma_B}\mathbf{b} = \mathbf{\Gamma_B}\mathbb{D}^{\mathbf{q_i}}\mathbf{a} = \left(\mathbf{\Gamma_B}\mathbb{D}^{\mathbf{q_i}}\mathbf{\Gamma_F}\right)\mathbf{f} = \mathbf{Q_{q_i}}\,\mathbf{f}\,, \tag{3.15}$$

To calculate the volume integrals, inner product matrix approach is used [108]. The derivation of the inner product matrix for simple 1D and 3D problems are given in author's previous publications [150, 151, 107, 152] in detail. However, here, the IBVP given in Eq. (3.14) has two varying functions (*i.e.* weighting functions). Therefore, the inner product matrix calculation for the multiplication of arbitrary functions $f(x,y,z)$ and $g(x,y,z)$ with weighting functions $A(x,y,z)$ and $B(x,y,z)$ can be written as

$$\int_{\mathbb{V}} f(x,y,z)\,g(x,y,z)\,A(x,y,z)\,B(x,y,z)\mathrm{d}\mathbb{V} = \mathbf{f}^{\mathrm{T}}\mathbf{V}_{A,B}\,\mathbf{g} \tag{3.16}$$

where $\mathbf{V}_{A,B}$ is the weighted inner product matrix. Each function in the integral operation has a degree of $N_x N_y N_z$; thus the multiplication of four functions will have an order of $4N_x 4N_y 4N_z$. Therefore, to obtain the weighted inner product matrix, each function evaluated at $N_x N_y N_z$ sampling points needs to be extrapolated to $4N_x 4N_y 4N_z$ sampling points using

$$\mathbf{f}_{4N_x 4N_y 4N_z} = \mathbf{S}^{x_4}\mathbf{S}^{y_4}\mathbf{S}^{z_4}\,f_{N_x N_y N_z} \tag{3.17}$$

where $S^{q_{in}}$ is the extrapolation matrix that can be obtained following the derivation in [108, 150]. Inserting Eq. (3.17) into Eq. (3.16), we can rewrite the weighted inner

product tensor as

$$\mathbf{V}_{A,B}^{abcdef} = \sum_{i,j,k}^{4N_x\,4N_y\,4N_z} \mathbf{v}_i^{4N_x}\mathbf{v}_j^{4N_y}\mathbf{v}_k^{4N_z}\left[\left(\mathbf{S}_{ia}^{x_4}\mathbf{S}_{jb}^{y_4}\mathbf{S}_{kc}^{z_4}\right)\right.$$

$$\left.\left(\mathbf{S}_{id}^{x_4}\mathbf{S}_{je}^{y_4}\mathbf{S}_{kf}^{z_4}\right)\left(\mathbf{S}_{il}^{x_4}\mathbf{S}_{jm}^{y_4}\mathbf{S}_{kn}^{z_4}\right)\left(\mathbf{S}_{io}^{x_4}\mathbf{S}_{jp}^{y_4}\mathbf{S}_{kr}^{z_4}\right)\mathbf{A}_{lmn}\mathbf{B}_{opr}\right], \tag{3.18}$$

where $\mathbf{v}$'s are the definite integral matrix derived in [108]. Note that $\mathbf{V}_{A,B}^{abcdef}$ is a 6th order tensor. To efficiently calculate this 6th order tensor, tensor multiplications are used [153, 154]. To transform $\mathbf{V}_{A,B}^{abcdef}$ into a matrix form, the same mapping algorithm, as given in Eq. (3.12), is applied.

Consequently, the system matrices of a lamina for the unconstrained case can be derived using the above formulations as;

$$\mathbf{M} = \mathbb{I}_{\boldsymbol{u}}{}^{\mathrm{T}}\mathbf{V}_{(\Upsilon,\mathbb{J})}\mathbb{I}_{\boldsymbol{u}} + \mathbb{I}_{\boldsymbol{v}}{}^{\mathrm{T}}\mathbf{V}_{(\Upsilon,\mathbb{J})}\mathbb{I}_{\boldsymbol{v}} + \mathbb{I}_{\boldsymbol{w}}{}^{\mathrm{T}}\mathbf{V}_{(\Upsilon,\mathbb{J})}\mathbb{I}_{\boldsymbol{w}} \tag{3.19}$$

$$\mathbf{K} = \left(\mathbf{Q_x}\mathbb{I}_{\boldsymbol{u}}\right)^{\mathrm{T}}\mathbf{V}_{(\lambda,\mathbb{J})}\left(\mathbf{Q_x}\mathbb{I}_{\boldsymbol{u}}\right) + 2\left(\mathbf{Q_x}\mathbb{I}_{\boldsymbol{u}}\right)^{\mathrm{T}}\mathbf{V}_{(\mu,\mathbb{J})}\left(\mathbf{Q_x}\mathbb{I}_{\boldsymbol{u}}\right)$$

$$+ \left(\mathbf{Q_x}\mathbb{I}_{\boldsymbol{u}}\right)^{\mathrm{T}}\mathbf{V}_{(\lambda,\mathbb{J})}\left(\mathbf{Q_y}\mathbb{I}_{\boldsymbol{v}}\right) + \left(\mathbf{Q_x}\mathbb{I}_{\boldsymbol{u}}\right)^{\mathrm{T}}\mathbf{V}_{(\lambda,\mathbb{J})}\left(\mathbf{Q_z}\mathbb{I}_{\boldsymbol{w}}\right)$$

$$+ \left(\mathbf{Q_y}\mathbb{I}_{\boldsymbol{v}}\right)^{\mathrm{T}}\mathbf{V}_{(\lambda,\mathbb{J})}\left(\mathbf{Q_x}\mathbb{I}_{\boldsymbol{u}}\right) + \left(\mathbf{Q_y}\mathbb{I}_{\boldsymbol{v}}\right)^{\mathrm{T}}\mathbf{V}_{(\lambda,\mathbb{J})}\left(\mathbf{Q_y}\mathbb{I}_{\boldsymbol{v}}\right)$$

$$+ 2\left(\mathbf{Q_y}\mathbb{I}_{\boldsymbol{v}}\right)^{\mathrm{T}}\mathbf{V}_{(\mu,\mathbb{J})}\left(\mathbf{Q_y}\mathbb{I}_{\boldsymbol{v}}\right) + \left(\mathbf{Q_y}\mathbb{I}_{\boldsymbol{v}}\right)^{\mathrm{T}}\mathbf{V}_{(\lambda,\mathbb{J})}\left(\mathbf{Q_z}\mathbb{I}_{\boldsymbol{w}}\right)$$

$$+ \left(\mathbf{Q_z}\mathbb{I}_{\boldsymbol{w}}\right)^{\mathrm{T}}\mathbf{V}_{(\lambda,\mathbb{J})}\left(\mathbf{Q_x}\mathbb{I}_{\boldsymbol{u}}\right) + \left(\mathbf{Q_z}\mathbb{I}_{\boldsymbol{w}}\right)^{\mathrm{T}}\mathbf{V}_{(\lambda,\mathbb{J})}\left(\mathbf{Q_y}\mathbb{I}_{\boldsymbol{v}}\right)$$

$$+ \left(\mathbf{Q_z}\mathbb{I}_{\boldsymbol{w}}\right)^{\mathrm{T}}\mathbf{V}_{(\lambda,\mathbb{J})}\left(\mathbf{Q_z}\mathbb{I}_{\boldsymbol{w}}\right) + 2\left(\mathbf{Q_z}\mathbb{I}_{\boldsymbol{w}}\right)^{\mathrm{T}}\mathbf{V}_{(\mu,\mathbb{J})}\left(\mathbf{Q_z}\mathbb{I}_{\boldsymbol{w}}\right)$$

$$+ \left(\mathbf{Q_y}\mathbb{I}_{\boldsymbol{u}}\right)^{\mathrm{T}}\mathbf{V}_{(\mu,\mathbb{J})}\left(\mathbf{Q_y}\mathbb{I}_{\boldsymbol{u}}\right) + \left(\mathbf{Q_x}\mathbb{I}_{\boldsymbol{v}}\right)^{\mathrm{T}}\mathbf{V}_{(\mu,\mathbb{J})}\left(\mathbf{Q_x}\mathbb{I}_{\boldsymbol{v}}\right)$$

$$+ \left(\mathbf{Q_z}\mathbb{I}_{\boldsymbol{v}}\right)^{\mathrm{T}}\mathbf{V}_{(\mu,\mathbb{J})}\left(\mathbf{Q_z}\mathbb{I}_{\boldsymbol{v}}\right) + \left(\mathbf{Q_y}\mathbb{I}_{\boldsymbol{w}}\right)^{\mathrm{T}}\mathbf{V}_{(\mu,\mathbb{J})}\left(\mathbf{Q_y}\mathbb{I}_{\boldsymbol{w}}\right)$$

$$+ \left(\mathbf{Q_z}\mathbb{I}_{\boldsymbol{u}}\right)^{\mathrm{T}}\mathbf{V}_{(\mu,\mathbb{J})}\left(\mathbf{Q_z}\mathbb{I}_{\boldsymbol{u}}\right) + \left(\mathbf{Q_x}\mathbb{I}_{\boldsymbol{w}}\right)^{\mathrm{T}}\mathbf{V}_{(\mu,\mathbb{J})}\left(\mathbf{Q_x}\mathbb{I}_{\boldsymbol{w}}\right). \tag{3.20}$$

Here, λ and μ are the varying Lamé parameters, and $\mathbb{I}_{\boldsymbol{q_i}}$ is the operator matrix (having a size of $N_\xi N_\eta N_\zeta \times 3N_\xi N_\eta N_\zeta$) to extract the necessary deflection components ($\mathbf{u}$, $\mathbf{v}$, and $\mathbf{w}$) in each direction and can be defined as

$$\boldsymbol{u} = \begin{bmatrix}\mathbb{I} & \mathbb{O} & \mathbb{O}\end{bmatrix}\mathbf{q} = \mathbb{I}_{\boldsymbol{u}}\mathbf{q}, \tag{3.21}$$

$$\boldsymbol{v} = \begin{bmatrix}\mathbb{O} & \mathbb{I} & \mathbb{O}\end{bmatrix}\mathbf{q} = \mathbb{I}_{\boldsymbol{v}}\mathbf{q}, \tag{3.22}$$

$$\mathbf{w} = \begin{bmatrix}\mathbb{O} & \mathbb{O} & \mathbb{I}\end{bmatrix}\mathbf{q} = \mathbb{I}_{\boldsymbol{w}}\mathbf{q}, \tag{3.23}$$

where $\mathbb{I}$ and $\mathbb{O}$ are ($N_\xi N_\eta N_\zeta \times N_\xi N_\eta N_\zeta$ dimensional) identity and zero matrices.

To increase the numerical efficiency of the presented technique, a non-dimensionalization approach can be used. For non-dimensionalizing, the spatial variables are scaled by a reference length, L_r; thus the spatial parameters defining the geometry of doubly-curved geometry leads to $x^* = x/L_r$, $y^* = y/L_r$, and $z^* = z/L_r$ (superscript * denotes the parameter is non-dimensionalized). The differential operator matrix needs to be non-dimensionalized as $\mathbf{B}^* = \mathbf{B}\,L_r$, since the partial derivative operation includes spatial variables. Lastly, using the Young's Modulus of the one of the constitutes of the FGM material, the constitutive matrix can be non-dimensionalized, $\mathbf{C}^* = \mathbf{C}/E_i$.

3.2.1 Boundary condition and coupling of the laminates

To couple the system matrices (*i.e.* the dynamics of) each lamina, and also to impose the boundary conditions to the system, projection matrices approach can be used. However, note here that since the IBVP approach is used, natural boundary conditions are already incorporated to the system matrices; only the essential boundary conditions need to be imposed. The boundary conditions can be defined in a matrix form as $\boldsymbol{\beta}\mathbf{q}_G = \mathbf{0}$ where $\mathbf{q}_G$ is the generalized coordinates of the laminated composite structure.

To couple individual lamina, compatibility equations need to be formed. These compatibility equations can basically be obtained by equating the degrees of freedom (u, v, and w) of each laminate at the intersection boundary. Similar to the boundary conditions, these equations can be included in the $\boldsymbol{\beta}$ matrix.

Then, following the projection matrices approach, the singular value decomposition of the $\boldsymbol{\beta}$ matrix will lead to $\boldsymbol{\beta} = \mathbf{U}\,\boldsymbol{\Sigma}\mathbf{V}^{\mathrm{T}}$ where $\mathbf{U}$ and $\mathbf{V}$ are unitary matrices and $\boldsymbol{\Sigma}$ is diagonal matrix with singular values of $\boldsymbol{\beta}$. Thus, using the left singular values, we can obtain

$$\mathbf{q}_G = \mathbf{P}\mathbf{q}_d \tag{3.24}$$

where $\mathbf{P}$ is the matrix that span the null space of $\boldsymbol{\beta}$ and can be expressed as

$$\mathbf{P} = \left[\mathbf{V}_{R_\beta}; \mathbf{V}_{R_\beta+1}; \ldots; \mathbf{V}_N\right]. \tag{3.25}$$

where R_β is the rank of $\boldsymbol{\beta}$, and N is the size of $\boldsymbol{\beta}$. Inserting Eq. (3.24) into the IBVP equation, and premultiply each term by $\mathbf{P}^{\mathrm{T}}$, the global system matrices can

be found as

$$\mathbb{M} = \mathbf{P}^{\mathrm{T}} \begin{bmatrix} \mathbf{M}_{l_1} & \dots & \mathbf{0} \\ \vdots & \ddots & \vdots \\ \mathbf{0} & \dots & \mathbf{M}_{l_n} \end{bmatrix} \mathbf{P} \tag{3.26}$$

$$\mathbb{K} = \mathbf{P}^{\mathrm{T}} \begin{bmatrix} \mathbf{K}_{l_1} & \dots & \mathbf{0} \\ \vdots & \ddots & \vdots \\ \mathbf{0} & \dots & \mathbf{K}_{l_n} \end{bmatrix} \mathbf{P} \, , \tag{3.27}$$

where $\mathbf{M}_{l_i}$ and $\mathbf{K}_{l_i}$ are the mass and stiffness matrices of each individual (i^{th}) lamina calculated using Eqs. (3.19) and (3.20), respectively.

4.   RESULTS

4.1 Plate reinforced with GPLs

In this study, we present a two-dimensional spectral method that uses Chebyshev polynomials (that have exponential convergence characteristics [30]) as the basis functions. The integral boundary value problem is derived using FSDT assumptions together with Hamilton's principle. To capture the varying material properties of FGPM-GPL reinforced composite plates, a multilayer modeling approach is followed. The problem domain is descritized using Gauss–Lobatto points to minimize the effect of Runge's phenomenon and further increase the computational efficiency. The problem domain is scaled to interval since in this interval a stable representation can be obtained with Chebyshev polynomials [30], [31]. The accuracy and performance of the presented solution technique is demonstrated for different porosity and nanofiller contents by comparing the natural frequencies and the critical buckling loads to those found in literature or to those calculated using a commercial finite element software.

The main contribution of this work is an accurate and fast converging meshless solution approach based on a novel use of Chebyshev polynomials to predict the vibration and elastic buckling behavior for functionally graded porous plates reinforced by graphene platelets. The recursive relations in forming the differentiation and inner-product (integration) matrices and the basis recombination (projection matrices) approach brings significant advantages including numerical efficiency and stability to the solution approach. The derivative and inner-product operations are calculated exactly, and the basis recombination approach can directly incorporate different boundary conditions without the necessity to use an admissible or an auxiliary function for each different boundary condition.

4.1.1 Model validation

To demonstrate the capability of the presented solution approach, two main case studies are investigated: **(i)** functionally graded porous material (FGPM) plates, and **(ii)** FGPM plates reinforced with GPLs (FGPM-GPL). In each case study, natural frequencies and critical buckling loads under fully-clamped (CCCC) or fully simply supported (SSSS) cases are calculated and the results are validated by comparing to the ones found in literature and/or using FE approach.

4.1.1.1 Convergence study

To determine the required number of layers (to accurately capture the grading material properties) and polynomial numbers along x and y directions, a convergence study is conducted. In this study, polynomial numbers and number of layers in the presented modeling approach is incrementally increased and the results for each individual case is compared to a reference case, that is obtained using a large polynomial number set ($N_x = N_y = 17$) and number of layers ($n = 20$). The convergence assessment is performed via a logarithmic approach given as follows:

$$LCV_{N_x, N_y} = \log\left(\frac{\lambda_{N_x, N_y} - \lambda_r}{\lambda_r}\right) \tag{4.1}$$

where LCV represent the logarithmic convergence number, λ_{N_x, N_y}^i and λ_r^i are the results for each individual case calculated using the selected polynomial numbers, and for the reference case, respectively. Note that the convergence analysis can be performed either for a specific parameter or for a set of parameters through averaging. The logarithmic approach enables to assess the convergence based on percent errors. For instance, for an error threshold of 0.1 %, the polynomial and layer numbers can be selected such that $LCV \leq -3$ is satisfied.

This convergence analysis leads to a four dimensional data. However, two dimensional contour plots are used to clearly visualize the convergence behavior. For instance, Fig. 4.1 shows the convergence behavior of the first five natural frequencies of an FGPM plate having the geometric properties of $a = b$, $h/a = 0.01$, and porosity coefficient of $e_o = 0.1$ under fully simply supported (SSSS) boundary condition for several selected number of layers. Note that, interpolation is used to present continuous contour plots.

As shown in Fig. 4.1, the optimum number of polynomial numbers correspond to $N_x = N_y$ since the investigated geometry is a square plate and the boundary condition is symmetric. Therefore, depending on the required accuracy, suitable poly-
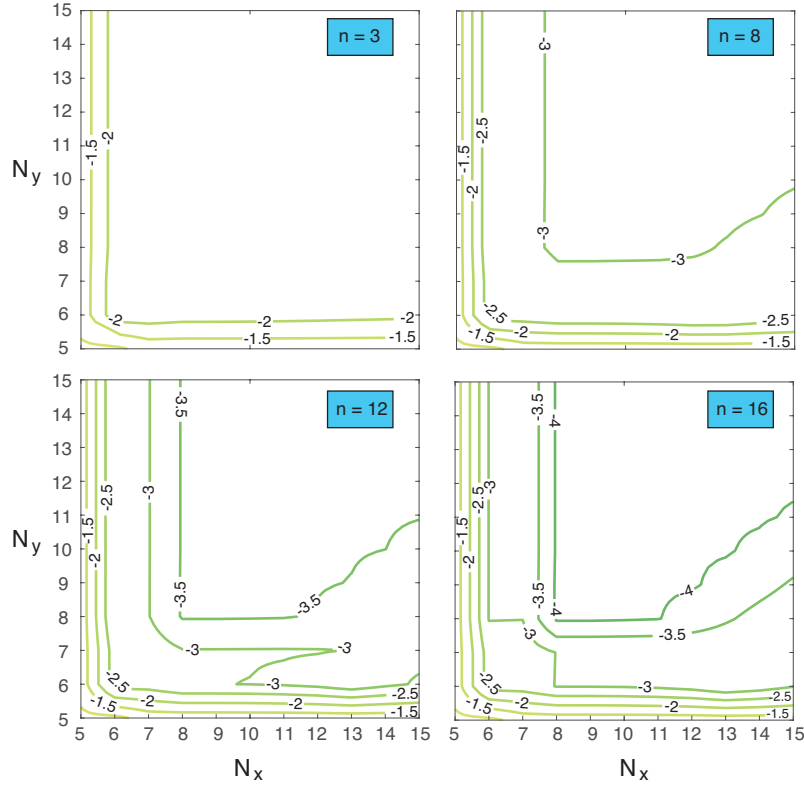
Figure 4.1 Convergence plots for a square FGPM plate with $h/a = 0.01$ under SSSS boundary condition for **(a)** $n = 3$, **(b)** $n = 8$, **(c)** $n = 12$, and **(d)** $n = 16$.

nomial numbers and total layer number can be found. It is important to highlight that depending on the geometry, material gradation amount, and the boundary condition, the required polynomial numbers may change to satisfy the same accuracy. The effect of these parameters on the convergence behavior has been investigated in detail in authors' previous publications [107, 109]. Therefore, following the presented convergence analysis, the polynomial numbers and the number of layers are selected to be $N_x = N_y = 11$ and $n = 15$, respectively, to achieve a minimum logarithmic convergence value of -4 (corresponds to an accuracy of 0.01 %).

4.1.1.2 Vibration and buckling analysis of FGPM plate

In this case study, first, the vibration behavior of an FGPM plate, having the geometric properties of $a/b = 1$, $h/b = 0.01$ or 0.1, is analyzed. The material properties of the nonporous material are given as $E^* = 200$ GPa, $\nu = 0.3$, and $\rho^* = 7850$ kg/m^3. Using the presented solution approach, first five natural frequencies corresponding to symmetric and uniform porosity distributions are calculated for fully-clamped (CCCC) and fully simply supported (SSSS) boundary conditions. The results are compared **(i)** to those given in Xue *et al.*'s study [155] where an isogeometric anal-

ysis based on FSDT and non-uniform rational B-spline (NURBS) basis functions is used, and **(ii)** to those obtained using a commercial FE software (COMSOL v5.5). The FE modeling in COMSOL is performed using the shell model with quadratic shape functions, based on a layered material approach and FSDT theory. A similar convergence analysis is also performed for FE analyses, and the required number of elements along x and y-directions of the plate are determined to be 20.

Table 4.1 The comparison of non-dimensional first five natural frequencies of an FGPM plate with symmetric porosity distribution, having the geometric properties of $a = b$, $h/b = 0.01$ or 0.1.

BC	h/b	Mode	$e_0=0.1$			$e_0=0.3$			$e_0=0.5$		
			ST	[155]	FE	ST	[155]	FE	ST	[155]	FE
CCCC	0.01	1	10.853	10.857	10.853	10.837	10.848	10.837	10.893	10.912	10.893
		2	22.115	22.126	22.115	22.082	22.106	22.081	22.192	22.234	22.192
		3	22.115	22.126	22.115	22.082	22.106	22.081	22.192	22.234	22.192
		4	32.579	32.595	32.578	32.528	32.564	32.526	32.688	32.749	32.687
		5	39.595	39.649	39.594	39.531	39.608	39.531	39.725	39.829	39.724
	0.1	1	9.798	9.800	9.798	9.726	9.734	9.726	9.699	9.713	9.699
		2	18.664	18.668	18.664	18.468	18.482	18.468	18.338	18.361	18.338
		3	18.664	18.668	18.664	18.468	18.482	18.468	18.338	18.361	18.338
		4	26.138	26.143	26.137	25.815	25.832	25.815	25.570	25.601	25.570
		5	30.774	30.781	30.774	30.351	30.371	30.351	30.008	30.042	30.007
SSSS	0.01	1	5.959	5.960	5.959	5.950	5.956	5.950	5.981	5.991	5.981
		2	14.888	14.893	14.888	14.866	14.881	14.866	14.943	14.969	14.943
		3	14.888	14.893	14.888	14.866	14.881	14.866	14.943	14.969	14.943
		4	23.807	23.816	23.807	23.772	23.796	23.772	23.893	23.935	23.893
		5	29.748	29.772	29.748	29.704	29.746	29.704	29.853	29.918	29.854
	0.1	1	5.752	5.754	5.752	5.732	5.737	5.732	5.746	5.755	5.746
		2	13.709	13.712	13.709	13.626	13.638	13.626	13.612	13.632	13.612
		3	13.709	13.712	13.709	13.626	13.638	13.626	13.612	13.632	13.612
		4	19.168	19.169	19.168	18.511	18.513	18.511	17.831	17.835	17.831
		5	19.168	19.169	19.168	18.511	18.513	18.511	17.831	17.835	17.831

Tables 4.1 and 4.2 list the first five non-dimensional natural frequencies for porosity coefficients of $e_0 = \{0.1, 0.3, 0.5\}$. The results are non-dimensionalized following the relation, $\bar{\omega} = \omega\,(b^2/h)\sqrt{\rho^*/E^*}$. As shown, based on the investigated case studies, the results are in excellent agreement with literature and FE results. To show the spectral-Chebychev efficiency in solving the problem, the computational time is compared to the FE method duration. The computational cost are obtained for three boundary conditions of a plate with geometric properties of $a/b = 1$ and $h/b = 0.1$, where the the porosity distribution is set to be symmetric along the thickness. It should be noticed that the study is accomplished with the same central processing unit(CPU). The computational costs are shown in Table. 4.3. The results indicate that the spectral-Chebuchev approach can obtain the accurate solution more efficient in comparison to the most-used method, FE approach.

Secondly, the elastic buckling of an FGPM plate with uniform porosity distribution having the geometry of $a/b = 1.5$, $h/b = \{0.01, 0.05, 0.1, 0.2\}$, is analyzed under SSSS

Table 4.2 The comparison of non-dimensional first five natural frequencies of an FGPM plate with uniform porosity distribution, having the geometric properties of $a = b$, $h/b = 0.01$ or 0.1.

BC	h/b	Mode	$e_0=0.1$ ST	$e_0=0.1$ [155]	$e_0=0.1$ FE	$e_0=0.3$ ST	$e_0=0.3$ [155]	$e_0=0.3$ FE	$e_0=0.5$ ST	$e_0=0.5$ [155]	$e_0=0.5$ FE
CCCC	0.01	1	10.698	10.698	10.698	10.296	10.296	10.296	9.810	9.811	9.810
		2	21.798	21.803	21.798	20.979	20.984	20.979	19.991	19.995	19.990
		3	21.798	21.803	21.798	20.979	20.984	20.979	19.991	19.995	19.990
		4	32.113	32.119	32.112	30.907	30.912	30.905	29.450	29.456	29.449
		5	39.029	39.072	39.028	37.563	37.604	37.562	35.792	35.832	35.792
	0.1	1	9.680	9.680	9.680	9.317	9.317	9.317	8.877	8.877	8.877
		2	18.465	18.465	18.465	17.771	17.771	17.771	16.933	16.933	16.933
		3	18.465	18.465	18.465	17.771	17.771	17.771	16.933	16.933	16.933
		4	25.879	25.879	25.879	24.907	24.907	24.906	23.733	23.733	23.732
		5	30.488	30.488	30.488	29.342	29.343	29.342	27.959	27.959	27.959
SSSS	0.01	1	5.873	5.873	5.873	5.652	5.652	5.652	5.386	5.386	5.386
		2	14.674	14.675	14.674	14.123	14.124	14.123	13.457	13.458	13.457
		3	14.674	14.675	14.674	14.123	14.124	14.123	13.457	13.458	13.457
		4	23.466	23.467	23.466	22.584	22.585	22.584	21.520	21.521	21.520
		5	29.322	29.337	29.322	28.220	28.235	28.220	26.890	26.904	26.890
	0.1	1	5.674	5.674	5.674	5.461	5.461	5.461	5.204	5.204	5.204
		2	13.537	13.537	13.537	13.028	13.028	13.029	12.414	12.414	12.415
		3	13.537	13.537	13.537	13.028	13.028	13.029	12.414	12.414	12.415
		4	19.162	19.163	19.162	18.443	18.442	18.443	17.573	17.573	17.573
		5	19.162	19.163	19.162	18.443	18.442	18.443	17.573	17.573	17.573

Table 4.3 The computational cost comparison of cases studied.

	Case (i) (FFFF) ST	Case (i) (FFFF) FEM	Case (ii) (SSSS) ST	Case (ii) (SSSS) FEM	Case (iii) (CCCC) ST	Case (iii) (CCCC) FEM
DOFs	605	5766	477	8214	405	10086
Duration (s)	0.34	10	0.29	11	0.30	10

boundary condition. The material properties of the nonporous material is given as $E^* = 70$ GPa, $\nu = 0.3$, and $\rho^* = 2707$ kg/m^3. The calculated critical buckling loads are compared to those found using FE analysis and to those listed in Thang *et al.*'s study in which the results are obtained following FSDT assumptions and Navier procedure [41]. Table 4.4 lists the non-dimensional uniaxial and biaxial critical buckling loads ($\overline{N}_{cr} = N_{cr}b^2/E^*h^3$). As expected, the plate gets stiffer with increasing thickness; thereby leading to higher critical buckling loads. Due to the geometry of the plate and the selected boundary condition, the critical buckling load is higher if the plate is uniaxially compressed along x direction. In all cases, excellent agreement is observed with the results found in literature and calculated using the FE approach.

Based on the performed convergence analyses, it is demonstrated that the presented solution approach enables a rapid convergence. To quantitatively assess the computational performance, we measured the simulation durations to obtain the results in

Table 4.4 The comparison of non-dimensional critical uniaxial and biaxial buckling loads of an FGPM plate having the geometric and material properties of $a/b = 1.5$ and $e_o = 0.4$ under SSSS boundary condition.

Distribution	h/b	(uniaxial) $N_x = -1$, $N_y = 0$		(uniaxial) $N_x = 0$, $N_y = -1$			(biaxial) $N_x = -1$, $N_y = -1$		
		ST	FE	ST	Ref. [41]	FE	ST	Ref. [41]	FE
uniform	0.01	2.875	2.876	1.383	—	1.383	0.957	—	0.957
	0.05	2.822	2.823	1.369	—	1.369	0.948	—	0.948
	0.1	2.669	2.669	1.329	1.332	1.329	0.920	0.922	0.920
	0.2	2.191	2.191	1.190	1.198	1.190	0.824	0.829	0.824
symmetric	0.01	3.342	3.342	1.607	—	1.607	1.113	—	1.113
	0.05	3.272	3.272	1.590	—	1.590	1.100	—	1.101
	0.1	3.070	3.070	1.536	1.544	1.536	1.064	1.069	1.064
	0.2	2.462	2.462	1.355	1.370	1.355	0.938	0.948	0.938

Tables 4.1 and 4.2. Note that the simulations are performed on the same computer, and computation duration is measured as the total simulation time in terms of central processing time (CPU) to find the first hundred eigenvalues and eigenvectors. Since the presented approach is a meshless method, the size of the system matrices is significantly smaller (about 20 folds in this case study) than the size of the system matrices used in a finite element approach to achieve the same level of accuracy. Consequently, the simulations durations are decreased at least 30 times with respect to FE simulations. Therefore, it can be concluded that the presented ST solution technique enables to capture the vibration and buckling behavior of porous plates as accurate as finite-element approach, yet at a fraction of the computational duration.

4.1.1.3 Vibration and buckling analysis of reinforced FGPM plate

To remedy the significant reduction in the effective stiffness of the material due to the porosity, nanofillers are used as reinforcement materials. In literature, reinforcing with CNTs is a common approach that can be applied to introduce an FG property along the thickness direction. However, due to the increased specific surface area and interaction between the matrix material, reinforcing with GPLs offers better mechanical enhancement compared to reinforcing with CNTs. Therefore, to demonstrate and compare the mechanical enhancement due to the addition of different nanofillers, natural frequencies of an FGPM composite plate and the percent improvements in the natural frequency values are calculated. The geometry of the plate is selected to be $a/b = 1$ and $h/b = 0.1$; the porosity distribution is set to be symmetric with a porosity coefficient of $e_o = 0.3$. The material and geometric properties of the matrix and nanofiller materials are tabulated in Table 4.5. In both cases of nanofillers, uniform distribution is used and the effective material properties can be found using the Halpin-Tsai formulations defined in Sec. 2.1.3. However, note

Table 4.5 Material and geometric properties of matrix material, GPLs, and single-walled CNTs.

Property	Matrix	GPLs	CNTs
Young's Mod. [Pa]	3×10^9	1.01×10^{12}	1.12×10^{12}
Density [kg/m^3]	1200	1062.5	2290
Poisson ratio	0.34	0.186	0.245
Width [m]	—	1.5×10^{-6}	—
Thickness [m]	—	1.5×10^{-9}	0.34×10^{-9}
Length [m]	—	2.5×10^{-6}	10×10^{-6}
Radius [m]	—	—	1×10^{-9}

that the nanofiller geometry factor, ζ_W^{GPL} is equal to 2 for CNTs [48, 69].

Figure 4.2 presents the variation of first and second natural frequencies as a function of wt.%. To validate the results in the case of nanofiller reinforcement, FE simulations are also performed. As shown, presented model predicts the natural frequencies as accurate as the FE approach; the maximum difference is calculated to be less than 0.003%. Another important observation that can be inferred from Fig. 4.2 is that as the volume of the reinforcement material is increased, the stiffness of the structure is significantly improved. Lastly, reinforcing using GPLs presents significantly better mechanical enhancement; for instance, the improvements in the fundamental frequency values are calculated as 37 % and 73 % due to the inclusion of 0.5 wt.% CNT and GPL, respectively. As stated above, the main reason is due to the GPL's improved interaction with the matrix material.

Next, to investigate the effect of thickness on the critical uniaxial buckling load of an FG square composite plate reinforced with GPL, a case study is performed for the porosity and GPL distribution patterns shown in Figs. 2.2 and 2.3. The porosity coefficient and the weight fraction (wt.%) of GPL are set to $e_o = 0.5$ and $\Lambda = 1$ wt.%, respectively. The matrix material is selected to be copper with the material properties defined as $E_m = 130$ GPa, $\rho_m = 8960$ kg/m^3, $\nu_m = 0.34$. The results are listed in Tables 4.6 and 4.7. To validate the calculated critical buckling loads, the results found in literature are used. Note that in this study, the results in the referred literature are obtained using 12 layers and non-dimensionalized following the relation $\overline{N}_{cr} = N_{cr}(1 - \nu_m^2)/E^*h$; thus the same amount of layers and non-dimensionalization approach are used for comparison. As seen, the results are in good agreement to those found in Yang *et al.*'s study [69]; the maximum difference is below 1%. The (uniaxial and biaxial) critical buckling loads increases as the composite plate gets thicker and also if the plate is fully-clamped, due to the significant increase in the stiffness of the structure. Furthermore, distributing the GPLs symmetrically instead of uniformly will increase the stiffness of the structure (that leads to an increase in
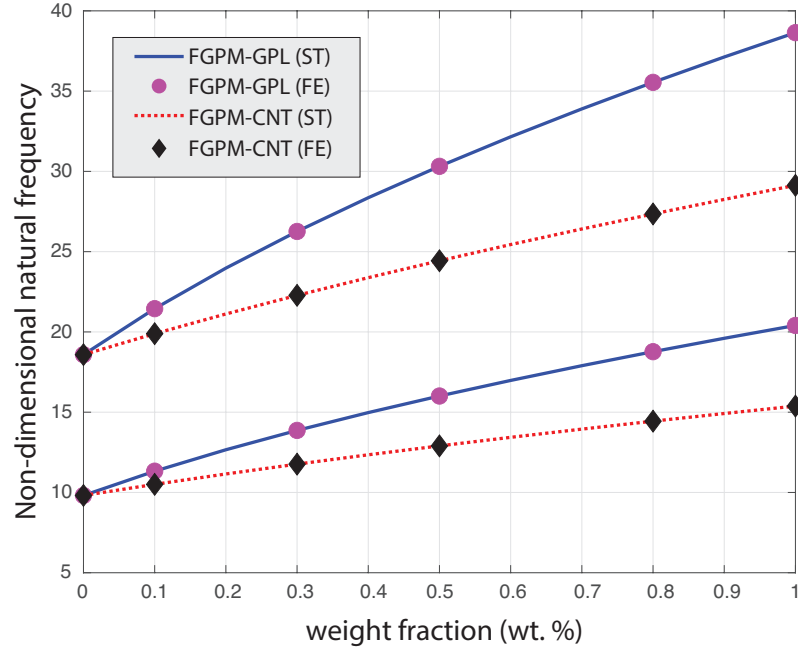
Figure 4.2 The comparison of non-dimensional first and second natural frequencies of a fully-clamped FG porous plate reinforced with uniformly distributed CNTs and GPLs. The geometry of the plate is defined as $a/b = 1$ and $h/b = 0.1$.

critical buckling loads) if the wt.% of the nanofillers is kept constant. This is mainly due to the fact that, in the case of symmetric distribution the GPL content at the outer layers of the plate is higher than the uniform distribution case and the stiffness of each layer is calculated based on the distance of each layer to the neutral surface (see Eq. 3.9).

To investigate the effects of weight fraction of GPL inclusion, the porosity and GPL distributions on the fundamental frequency and uniaxial critical buckling loads of an FGPM composite plate, a parametric case study is performed and the results are plotted in Fig. 4.3. Firstly, as expected, the fundamental frequency and critical buckling load increase as we increase the weight fraction of GPLs; even a small amount of GPL inclusion has a significant effect on the stiffness of the structure. Secondly, the distribution of the nanofiller has also a dominant effect. Although the same amount of nanofillers are used, distributing them closer to the outer layers of the material will increase the stiffness of the composite panel more than distributing them uniformly; thereby leading to higher natural frequency and critical buckling force values.

Table 4.6 The comparison of non-dimensional uniaxial ($N_x = -1$, $N_y = 0$) buckling loads of an FGPM square plate reinforced with GPLs having a porosity coefficient of $e_o = 0.5$ and weight fraction of $\Lambda = 1$ wt.%.

BC	b/h	Symmetric Porosity Distribution				Uniform Porosity Distribution			
		GPL - Patern A		GPL - Patern B		GPL - Patern A		GPL - Patern B	
		ST	[69]	ST	[69]	ST	[69]	ST	[69]
CCCC	20	0.02912	0.02899	0.02396	0.02384	0.02464	0.02452	0.02002	0.01990
	30	0.01349	0.01343	0.01103	0.01098	0.01136	0.01130	0.00917	0.00911
	40	0.00771	0.00767	0.00629	0.00625	0.00647	0.00644	0.00521	0.00518
	50	0.00497	0.00494	0.00405	0.00403	0.00417	0.00415	0.00335	0.00333
SSSS	20	0.01223	0.01217	0.00998	0.00992	0.01028	0.01022	0.00827	0.00822
	30	0.00550	0.00547	0.00448	0.00445	0.00461	0.00459	0.00371	0.00368
	40	0.00310	0.00309	0.00253	0.00251	0.00260	0.00259	0.00209	0.00208
	50	0.00199	0.00198	0.00162	0.00161	0.00167	0.00166	0.00134	0.00133
SCSC	20	0.02235	-	0.00237	-	0.00245	-	0.00196	-
	30	0.01035	-	0.00106	-	0.00110	-	0.00087	-
	40	0.00591	-	0.00060	-	0.00062	-	0.00049	-
	50	0.00381	-	0.00038	-	0.00040	-	0.00032	-
SFSF	20	0.00292	-	0.01835	-	0.01886	-	0.01530	-
	30	0.00131	-	0.00844	-	0.00869	-	0.00700	-
	40	0.00074	-	0.00481	-	0.00495	-	0.00398	-
	50	0.00047	-	0.00310	-	0.00319	-	0.00256	-

Posority Distribution (UD) - GPL Distribution (UD)
Posority Distribution (SYM) - GPL Distribution (UD)
Posority Distribution (UD) - GPL Distribution (SYM)
Posority Distribution (SYM) - GPL Distribution (SYM)
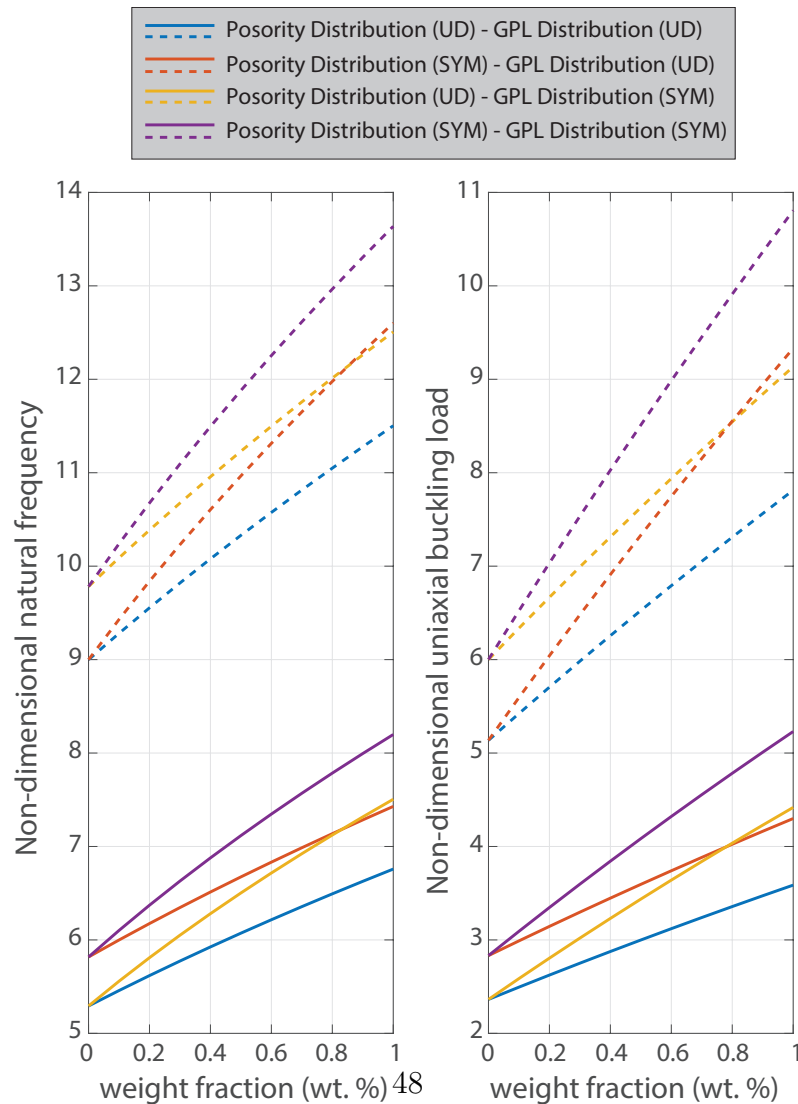
Figure 4.3 The effects of weight fraction and porosity/GPL distributions on non-dimensional fundamental frequency and uniaxial buckling load of a fully-clamped FGPM plate reinforced with GPLs. The geometry of the plate is

Table 4.7 The comparison of non-dimensional biaxial ($N_x = -1$, $N_y = -1$) buckling loads of an FGPM square plate reinforced with GPLs having a porosity coefficient of $e_o = 0.5$ and weight fraction of $\Lambda = 1$ wt.%.

| BC | b/h | Symmetric Porosity Distribution | | | | Uniform Porosity Distribution | | | |
| | | GPL - Patern A | | GPL - Patern B | | GPL - Patern A | | GPL - Patern B | |
		ST	Ref. [69]	ST	Ref. yang2017buckling	ST	Ref. [69]	ST	Ref. [69]
CCCC	20	0.01557	0.01550	0.01278	0.01271	0.01315	0.01308	0.01066	0.01059
	30	0.00715	0.00712	0.00584	0.00581	0.00602	0.00599	0.00485	0.00482
	40	0.00407	0.00405	0.00332	0.00330	0.00342	0.00340	0.00275	0.00273
	50	0.00262	0.00261	0.00214	0.00212	0.00220	0.00219	0.00177	0.00176
SSSS	20	0.00611	0.00608	0.00499	0.00496	0.00514	0.00511	0.00414	0.00411
	30	0.00275	0.00273	0.00224	0.00223	0.00231	0.00229	0.00185	0.00184
	40	0.00155	0.00154	0.00126	0.00126	0.00130	0.00129	0.00105	0.00104
	50	0.00100	0.00099	0.00081	0.00081	0.00083	0.00083	0.00067	0.00067
SCSC	20	0.01142	-	0.00934	-	0.00961	-	0.00776	-
	30	0.00522	-	0.00425	-	0.00437	-	0.00352	-
	40	0.00296	-	0.00241	-	0.00248	-	0.00199	-
	50	0.00190	-	0.00155	-	0.00159	-	0.00128	-

Finally to understand the effects of other parameters such as porosity coefficient and aspect ratio (a/b) on the dynamic and buckling behavior of FGPM reinforced with GPLs, several case studies are performed and the results are plotted in Figs. 4.4 and 4.5. As shown in Fig. 4.4(a), in the case of symmetric porosity distribution, porosity coefficient does not have a significant effect of the vibration behavior of the composite structure due to the fact that porosity decreases the stiffness and the weight of the structure proportionally. On the other hand, the weight fraction of the nanofiller affect the stiffness of the structure dominantly; thus the natural frequencies depends highly on the weight fraction. However, in the case of buckling behavior, both the porosity coefficient and the weight fraction values have a significant effect on the critical buckling load.

In Fig. 4.5, the variation in natural frequency and uniaxial buckling load values as a function of plate aspect ratio (a/b) is shown for three different thickness ratios (h/b). As expected, as the length of the structure increases, its natural frequency decreases as well. Since the non-dimensional natural frequency is plotted, the difference between the three different thickness ratios is extremely small; the only difference in these cases are due to the variations arising from the porosity and GPL distributions. On the other hand, the critical buckling load does not monotonically decrease as the aspect ratio increases. The lowest critical buckling loads are observed for aspect ratios where the number of half sine waves divides the buckling mode shape into unit squares [156, 157]. In both cases, the effect of aspect ratio is highly significant between $a/b = 0.5$ to $a/b = 1$; both the natural frequency and critical buckling load values experiences a sudden decrease with a minor increase in aspect ratio.
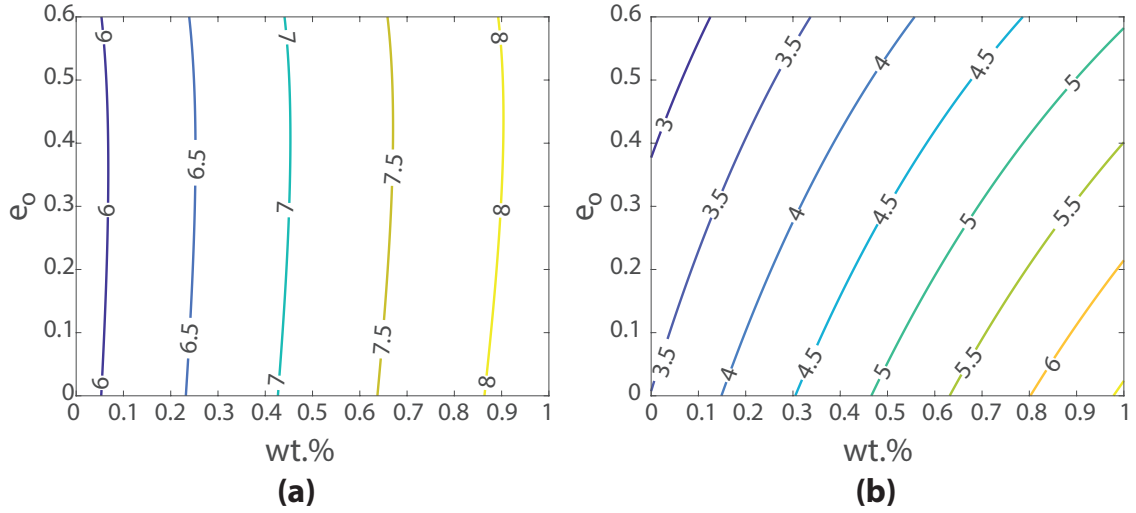
Figure 4.4 Contour plot showing the effects of weight fraction and porosity coefficient on **(a)** non-dimensional fundamental frequency and **(b)** uniaxial buckling load of a simply-supported FGPM plate reinforced with GPLs. The geometry of the plate is selected to be $a/b = 1$ and $h/b = 0.1$. The porosity and GPL distributions are selected to be symmetric.
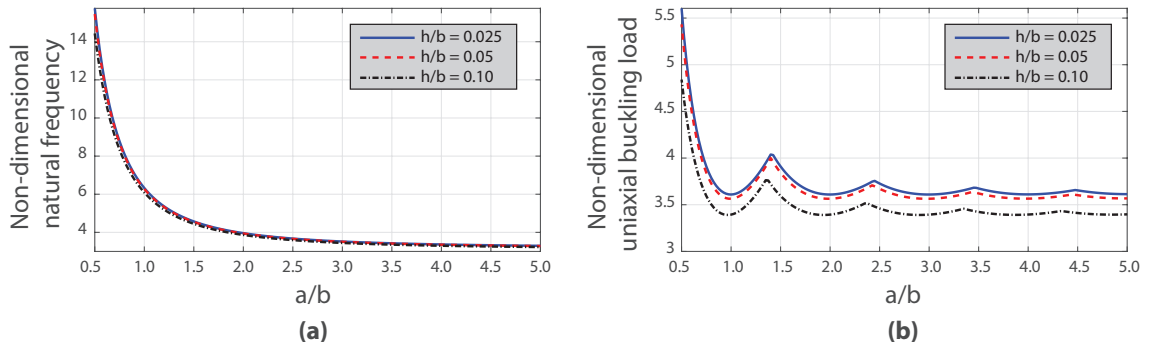
Figure 4.5 Effect of aspects ratio (a/b) on **(a)** non-dimensional fundamental frequency and **(b)** uniaxial $(N_x = -1, N_y = 0)$ buckling load of a simply-supported FGPM plate reinforced with GPLs. The porosity and GPL distributions are selected to be symmetric.

4.2 Layered FGM structure

The aim of the present work is to study the 3D (coupled) dynamics of laminated FGM composite structures having arbitrary shapes using the 3D spectral Chebychev (3D-ST) technique. In this technique, the integral boundary value problem (IBVP) governing the dynamics of the problem is derived using 3D elasticity equations. To simplify the domain of the problem, two consecutive transformations are applied: (i) first, a coordinate mapping to map the curved geometry to a straight one [50], [56], and (ii) second, a one-to-one mapping technique based on polynomial mapping to map the arbitrary curved geometry onto a simple square geometry [57]. Then, the simplified form of the IBVP is discretized using Gauss–Lobatto points and triple

expansion of Chebychev polynomials [58]. To facilitate the spatially varying material properties along one or more spatial directions, the Mori–Tanaka or theory of mixtures methods are utilized. Finally, the boundary conditions are incorporated and the laminates are coupled using projection matrix method. This technique offers several important advantages compared to the available methods in the literature. First of all, the projection matrices approach eliminates the need to use different basis/trial functions for each different boundary condition. Secondly, the presented approach can be applied to arbitrarily shaped composite structures since the free-from geometry is transferred to a simplified geometry. Thirdly, since the integral form of the boundary value problem is used, the necessity to impose natural boundary conditions is eliminated; only the essential boundary conditions need to be imposed. Lastly, the IBVP is discretized using Chebychev polynomials that exhibits exponential convergence behavior [59], [60]; and the derivative and integral operations are evaluated exactly and efficiently using Chebychev matrix operations and Galerkin's method [61]. Note that compared to (spectral-) collocation methods (such as Chebyshev spectral approach [62] or Carrera Unified Formulation [63], [64]) where the equations are satisfied only at the sampling points, the presented solution technique ensures that the integrals of the equations vanish with respect to all polynomials of a certain degree; thereby increases the accuracy/precision of the solution approach.

4.2.1 Model validation

The validation and performance of the presented spectral-Chebychev solution approach is performed through three case studies. In the first case study, the (non-dimensional) natural frequencies and the corresponding mode shapes of a FGM doubly curved lamina under various boundary conditions is investigated. Second case study includes the analyses of doubly-curved laminated FGM structures. Lastly, in the third case study, FGM structures having arbitrary geometries are studied. In each case, the results are compared either to those obtained through a commercial FE software or to those found in literature. For FE analysis, COMSOL Multiphysics® software is used. The composite structures are meshed with tetrahedral elements (with linear shape functions) and the natural frequency and mode shapes are determined using direct eigenfrequency solver *MUMPS* (which is based on LU decomposition).

For case studies, the constituent materials of the FGM doubly-curved structure are selected to be aluminum as the metallic structure ($E_m = 70$ GPa, $\nu_m = 0.3$, and

$\rho_m = 2702 \, \text{kg/m}^3$) and zirconia as the ceramic structure ($E_c = 200 \, \text{GPa}$, $\nu_c = 0.3$, and $\rho_c = 5700 \, \text{kg/m}^3$). Note that, if necessary, the IBVP is non-dimensionalized based on the material properties of the metallic structure (*i.e.*, $E_m^* = E_m/E_m$, $E_c^* = E_c/E_m$, $\rho_m^* = \rho_m/\rho_m$, and $\rho_c^* = \rho_c/\rho_m$).

4.2.1.1 Doubly-curved FGM rectangular lamina

In this case study, a doubly curved lamina made of FGM, as depicted in Fig. 4.6, is investigated using the presented solution method. Here, R_1 and R_2 represent the radii corresponding to the curvatures around x and y axes, respectively; L_x and L_y are the lengths of the rectangular lamina along x'' and y'' axes, respectively; and h represents the thickness of the lamina. Note that, depending on the R_1 and R_2 values, it is possible to analyze the dynamics of straight, cylindrical, spherical, and hyperbolic laminates.
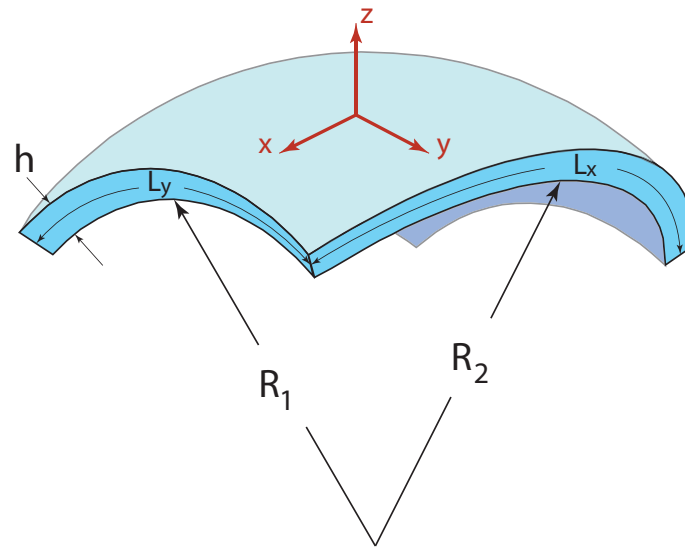
Figure 4.6 Schematic showing the geometries of a rectangular doubly-curved lamina.

Prior to the validation of the presented solution technique, a convergence analysis is performed to demonstrate the stability and fast convergence characteristics of the presented approach. In this analysis, the geometric parameters of the doubly curved FGM lamina is selected as $L_x/L_y = 1$ (*i.e.* when mapped to a straight lamina, it corresponds to a parallelepiped), $h/L_x = 0.1$, and $\beta_1 = \beta_2 = 0.25$ (note that β is defined as the fraction of full curvature in Sec. 2.2.2). The material distribution is assumed to be along the thickness direction (z direction) and gradation parameter is selected to be $p = 0.3$. For the investigated geometry, the number of polynomials

along each direction x, y, z (or ξ, η, and ζ) are increased incrementally, and the results are compared to those obtained for a reference case (that is obtained using a large triplet polynomial number set). To qualitatively assess the level of convergence for each triplet number of polynomials, a logarithmic convergence (LC) value defined as follows

$$C^i_{N_\xi,N_\eta,N_\zeta} = \log\left(\frac{|\lambda^i_{N_\xi,N_\eta,N_\zeta} - \lambda^i_r|}{\lambda^i_r}\right),\tag{4.2}$$

is used. Here, the λ's are the natural frequencies and C is the LC value. The superscripts represents the values corresponding to the ith natural frequency, and subscripts show the chosen triplet polynomial numbers or the result of the selected reference case. Therefore, based on a selected convergence value (that can be defined for each individual mode or can be defined as an average of a number of modes), the optimum triplet polynomial numbers can be selected. Note that the LC values forms a three-dimensional matrix. Thus, the optimum triplet polynomial number is determined such that it both satisfies the selected convergence criteria and leads to the smallest product of polynomials (thus minimizes the degrees of freedom -DOF- of the model).

To understand the convergence rate/characteristic thoroughly, two studies are performed. In the first one, the convergence characteristic of the presented solution approach is investigated in detail for an unconstrained doubly curved FGM parallelepiped. Although, the convergence analysis leads to a 3D-plot, to clearly visualize the behavior, 2D convergence plots that are given for a specific N_ζ value (*i.e.* horizontal and vertical axes indicate the N_ξ and N_η polynomials, respectively), are given in Fig. 4.7. Note that, the 2D convergence plots are based on the average LC values calculated using the first ten natural frequencies that are compared to the reference solution, that is selected as $N_\xi - N_\eta - N_\zeta = 21 - 21 - 13$. As seen from straight portions of the contour lines in Fig. 4.7, increasing the polynomial numbers along the N_ξ and N_η directions beyond a point does not affect the results. Since the geometry of the investigated geometry is selected as $L_y/L_x = 1$, the convergence plots are (almost) symmetric with respect to $N_\xi = N_\eta$ line. Therefore considering the convergence data in Fig. 4.7, if the convergence criteria is determined as $C^i < -3$ or $C^i < -4$, the triplet polynomial number can be selected as 9-9-7 or 11-11-11, respectively.

Next, to demonstrate the convergence characteristics corresponding to various boundary conditions and geometric parameters, four different cases are investigated (keeping the geometric parameters of the structure as $L_y/L_x = 1$ and $h/L_x = 0.1$): **(i)** unconstrained straight parallelepiped with uniform material prop-
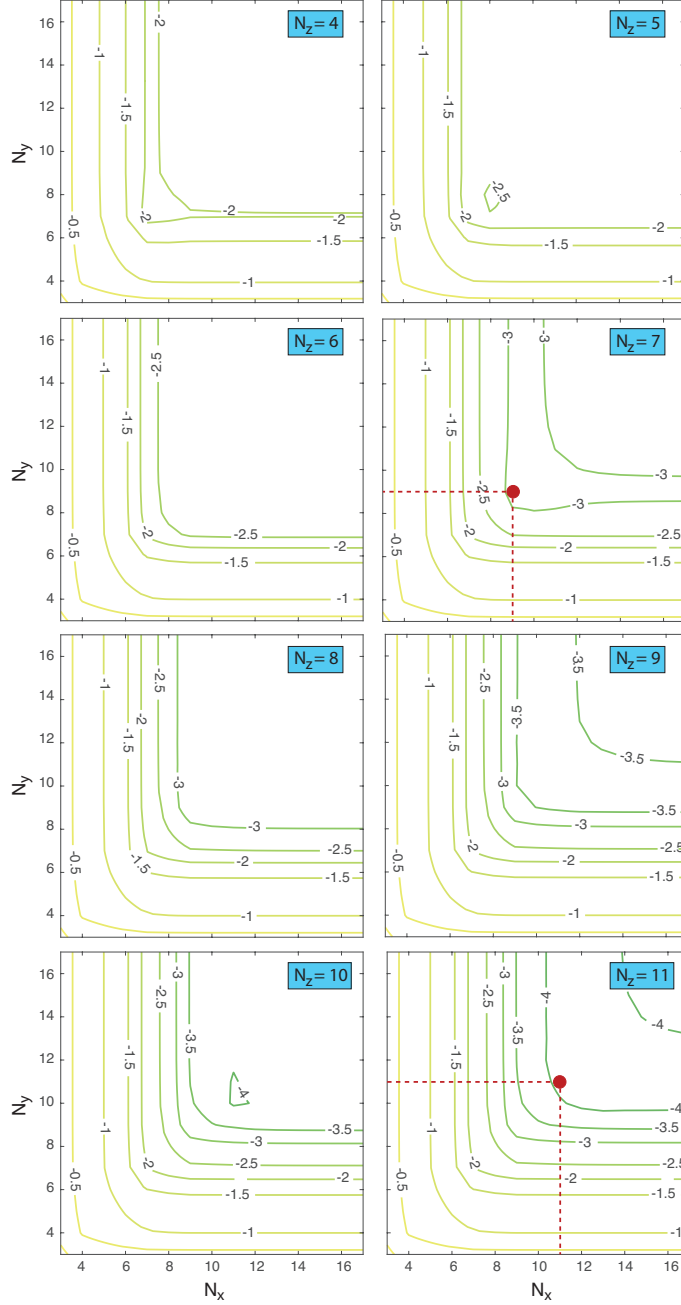
Figure 4.7 Convergence study for an unconstrained doubly curved FGM structure with uni-axially varying material property along the z ($p = 0.3$) direction. Red circle markers show the required (optimum) number of triplet-polynomials to meet the selected convergence criteria.

erties (*i.e.* $\beta_1 = \beta_2 = 0$ and $p = 0.0$), **(ii)** unconstrained singly-curved (cylindrical) parallelepiped with uniform material properties (*i.e.* $\beta_1 = 0.25$, $\beta_2 = 0$, and $p = 0.0$), **(iii)** unconstrained doubly curved FGM parallelepiped (*i.e.* $\beta_1 = \beta_2 = 0.25$ and $p = 0.3$), and **(iv)** fully-constraint doubly curved FGM parallelepiped (*i.e.* $\beta_1 = \beta_2 = 0.25$ and $p = 0.3$). The first ten (non-dimensional) natural frequencies are calculated in each case and the results are compared to the one that is found using $N_\xi - N_\eta - N_\zeta = 21 - 21 - 13$ polynomials (that is selected to be the reference
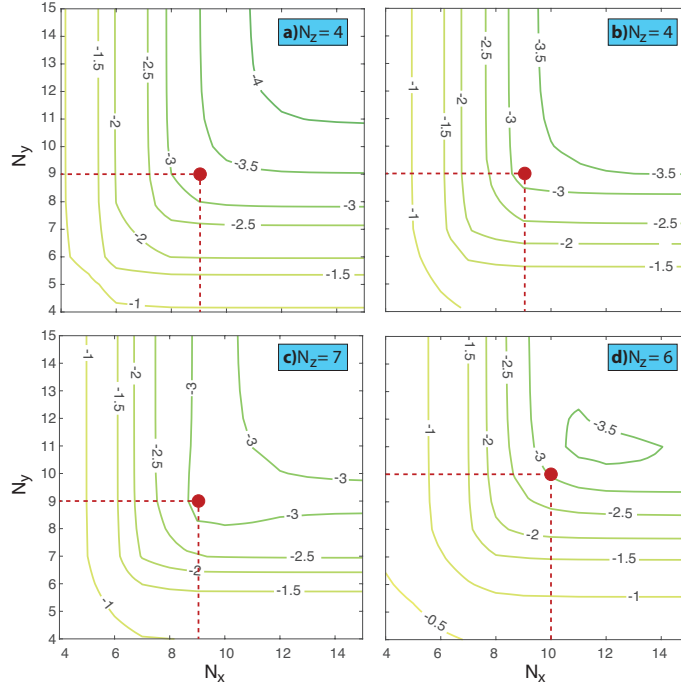
Figure 4.8 Convergence study for **(a)** unconstrained straight parallelepiped **(b)** unconstrained doubly-curved structure **(c)** unconstrained doubly-curved structure with uni-axially varying material properties along the z ($p = 0.3$) direction and **(d)** doubly-curved structure with uni-axially varying material properties along the z ($p = 0.3$) direction and constrained at all edges. Red circle markers show the required (optimum) number of triplet-polynomials in each case to meet the selected convergence criteria ($C^i < -3$).

solution). The convergence criteria is selected such that the individual and average error threshold values are set to 0.1% ($C^i < -3$). The selected triplet polynomial numbers are shown in Fig. 4.8. Although, the convergence analysis leads to a 3D plot, as mentioned above 2D convergence plots are used here. Therefore, based on the selected convergence criteria, the triplet polynomial numbers can be chosen as 9-9-4, 9-9-4, 9-9-7, and 10-10-6, for cases (i) through (iv), respectively.

Note that comparing the cases (i) and (ii) in Fig. 4.8, the required triplet polynomial numbers to meet the convergence criteria is found to be equal to each other; however, if the contours of the plots are analyzed, it can be seen that there is a shift in counter lines to higher polynomial numbers. Thus, the LC value corresponding the chosen set of polynomials in case (i) is calculated to be higher than case (ii) (see Fig. 4.8 (a) and (b)). Therefore, it can be concluded from Fig. 4.8 that as the complexity increases in the problem either in geometry (due to curvatures or boundary conditions) or in material distribution, the convergence rate decreases. As a result, to meet the required LC value, the required triplet polynomial numbers (*i.e.*, required degree of freedom) increases as well.

Table 4.8 The comparison of non-dimensional natural frequencies of an unconstrained doubly-curved FGM ($p = 0.3$ along the z direction) structure having the geometric properties of $L_x/L_y = 1$, $h/L_x = 0.1$, (i) $\beta_1 = 0.0$, $\beta_2 = 0$ (ii) $\beta_1 = 0.50$, $\beta_2 = 0.00$, (iii) $\beta_1 = 0.25$, $\beta_2 = 0.25$, and (iv) $\beta_1 = 0.25$, $\beta_2 = -0.25$ predicted using the presented ST solution and FE simulations.

Mode	Case (i) (straight panel)			Case (ii) (cylindrical panel)			Case (iii) (spherical panel)			Case (iv) (hyperbolic panel)		
	ST	FEM	Diff. (%)	ST	FEM	Diff. (%)	ST	FEM	Diff. (%)	ST	FEM	Diff. (%)
1	0.4120	0.4119	0.04	0.3554	0.3554	0.03	0.4446	0.4444	0.04	0.3408	0.3405	0.08
2	0.6124	0.6131	0.10	0.4165	0.4180	0.35	0.5616	0.5623	0.13	0.6126	0.6142	0.26
3	0.7527	0.7553	0.34	0.6856	0.6865	0.13	1.0193	1.0196	0.02	0.7776	0.7791	0.19
4	1.0350	1.0357	0.06	1.1130	1.1152	0.20	1.1599	1.1611	0.11	0.7983	0.7967	0.19
5	1.0350	1.0357	0.06	1.2018	1.2048	0.25	1.2175	1.2187	0.10	1.0316	1.0322	0.06
6	1.7960	1.8000	0.22	1.2961	1.2972	0.08	1.7941	1.7976	0.20	1.4010	1.3986	0.17
7	1.7960	1.8000	0.22	1.3981	1.4015	0.25	1.9098	1.9116	0.09	1.6454	1.6429	0.15
8	1.8116	1.8128	0.06	1.8740	1.8734	0.04	2.1370	2.1399	0.14	1.7236	1.7192	0.26
9	1.9731	1.9730	0.00	2.1874	2.1908	0.15	2.1396	2.1399	0.02	1.7302	1.7346	0.25
10	2.2012	2.2044	0.15	2.2764	2.2873	0.48	2.5320	2.5370	0.20	1.7793	1.7801	0.05

To validate and present the capability of the solution approach, firstly, various 3D geometries such as straight, cylindrical, spherical, and hyperbolic structures are investigated (see Table 4.8). Secondly, the dynamics of a 3D doubly-curved structure under various boundary conditions is analyzed (see Table 4.9). As described in Sec. 3.2.1, the essential boundary conditions can be applied in 3D-ST solution by using the projection matrices. In both studies, the material variation is assumed to be along the z (ζ) direction and the gradation parameter, p, is selected to be 0.3 (see Eq. (2.34)) in both cases. The calculated non-dimensional natural frequencies are compared to those obtained from a commercial FE software (COMSOL v5.3). Note that a similar convergence analysis is performed for the FE analysis to determine the required element number. As seen from the given tables, the maximum difference in predicted natural frequencies is calculated as 0.77% (the average difference is found as 0.13%); therefore we can conclude that the results are in excellent agreement.

The predicted mode shapes are also investigated and validated using FE results. As an example, Fig. 4.9 shows the predicted first four mode shapes for the cases investigated in Table 4.8. To validate the mode shapes, the modal assurance criteria (MAC), which is a measure of consistency of mode shapes calculated by two different solution approaches [158], is used. The MAC plots for the case studies given in Tables 4.8 and 4.9 are given in Fig. 4.10. Note that for the symmetric mode shapes (corresponding to the same natural frequency) as can be seen in the straight panel case in 4th and 5th and 6th and 7th mode shapes, the MAC values can be lower than 0.9. However, in general it is observed that the calculated MAC values for the first ten natural frequencies for all cases are close to unity. The average MAC value is calculated to be 0.9716 for the investigated cases. Therefore, we can conclude that

Table 4.9 The comparison of non-dimensional natural frequencies of a doubly-curved FGM structure having the geometric properties of $L_x/L_y = 4/3$, $h/L_x = 0.1$, $\beta_1 = 1/4$, $\beta_2 = 1/3$ and material variation parameter as $p = 0.3$ (along the z direction) under four different boundary conditions: **(i)** unconstrained (FFFF), **(ii)** constrained at $x = -L_x/2$ side (CFFF), **(iii)** constrained at $x = -L_x/2$ and $x = L_x/2$ sides (CFCF), and **(iv)** constrained on all sides (CCCC).

Mode	Case (i): FFFF			Case (ii): CFFF			Case (iii): CFCF			Case (iv): CCCC		
	ST	FEM	Diff. (%)	ST	FEM	Diff. (%)	ST	FEM	Diff. (%)	ST	FEM	Diff. (%)
1	0.3864	0.3868	0.10	0.0720	0.0719	0.10	0.7072	0.7055	0.24	1.8366	1.8358	0.04
2	0.3985	0.3985	0.00	0.1068	0.1066	0.14	0.7368	0.7355	0.18	2.0453	2.0421	0.16
3	0.8518	0.8516	0.02	0.2845	0.2844	0.04	0.9476	0.9470	0.06	2.0833	2.0849	0.07
4	0.9724	0.9740	0.17	0.3592	0.3587	0.16	0.9925	0.9918	0.08	2.5830	2.5858	0.11
5	1.4424	1.4446	0.15	0.6656	0.6650	0.08	1.2509	1.2503	0.05	2.6733	2.6729	0.01
6	1.4832	1.4844	0.08	0.8084	0.8083	0.02	1.5865	1.5858	0.04	2.9768	2.9802	0.12
7	1.6618	1.6633	0.09	1.1838	1.1838	0.00	1.8398	1.8413	0.08	3.2907	3.2935	0.09
8	1.7743	1.7775	0.18	1.3963	1.3958	0.04	1.8775	1.8759	0.08	3.4268	3.4004	0.77
9	2.1222	2.1257	0.17	1.5648	1.5656	0.05	1.8785	1.8796	0.06	3.5447	3.5494	0.13
10	2.1958	2.1943	0.07	1.6545	1.6542	0.01	2.2219	2.2195	0.11	3.9027	3.8946	0.21

Table 4.10 The computational cost comparison of cases studied in Table 1

	Case (i) (straight panel)		Case (ii) (cylindrical panel)		Case (iii) (spherical panel)		Case (iv) (hyperbolic panel)	
	ST	FEM	ST	FEM	ST	FEM	ST	FEM
DOFs	1701	153165	2079	178794	1701	145806	1701	158877
Duration (s)	1.55	127	3.92	1112	3.07	91	2.9	125

the mode shapes obtained using the presented solution technique are in excellent agreement to those found through FEM approach.

In these analyses, we also compared the computational cost of each solution approach based on the central processing unit (CPU) time. To compare the computational cost, the total duration of the simulation to find the first hundred eigenvalues and eigenvectors is measured. Tables 4.10 and 4.11 show the simulation duration (in terms CPU time) of the presented solution technique and the FE simulations to achieve a converged result, and the corresponding number of degrees of freedom for each case. The comparison are performed on the same computer. As a result, the matrix sizes are decreased significantly (around 50 folds), thereby reducing the computational cost of the investigated cases at least 10 folds. Note that in FE modeling, the meshing is performed automatically with tetrahedral elements (with linear shape functions) and solutions are performed using MUMPS algorithm (that can take advantage of all of the processor cores).

The presented approach can be used both together with the Mori-Tanaka and theory of mixtures approaches to impose the varying material properties to the system equations. To investigate the changes in predicted natural frequencies, we performed three case studies for an unconstrained cylindrical FG composite structure having
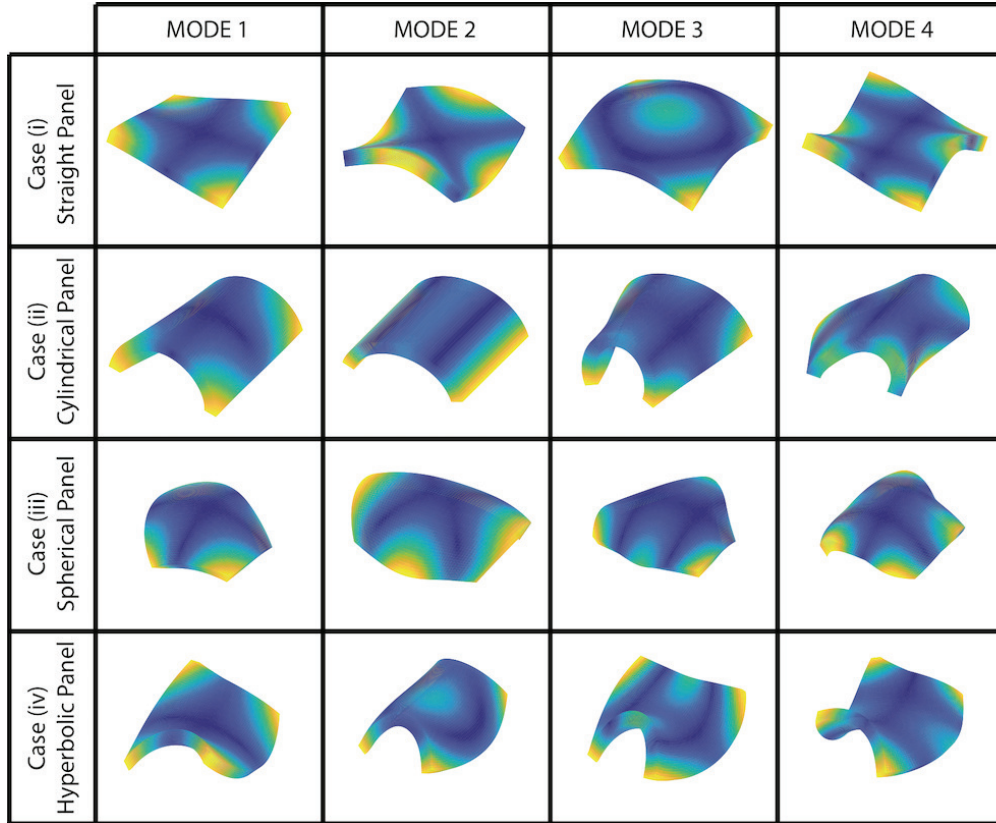
Figure 4.9 The first four mode shapes of the case studies investigated in Table 4.8.
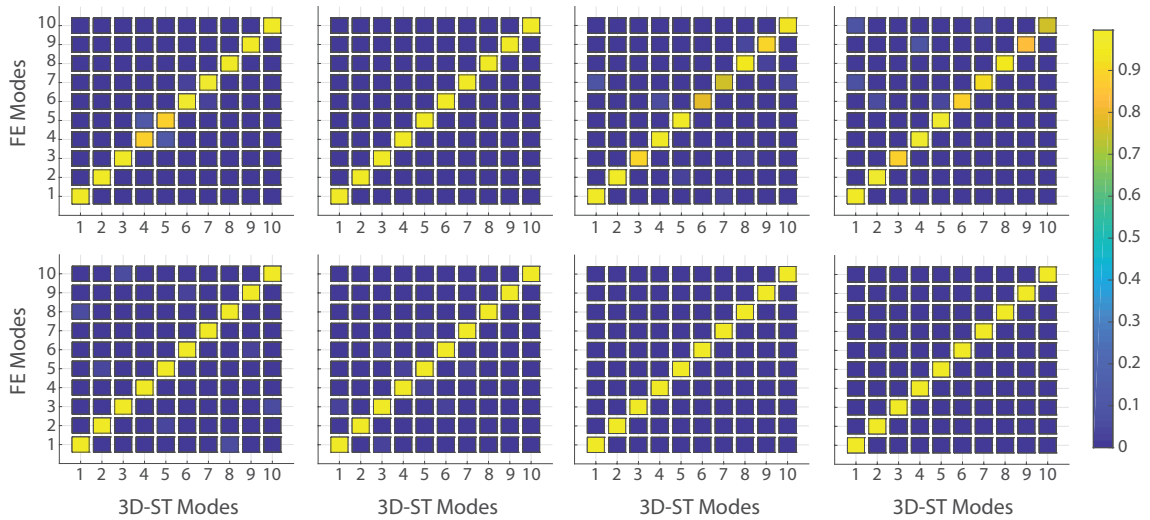
Figure 4.10 The MAC plots of the first ten natural frequencies for the cases investigated in Tables 4.8 and 4.9 (Top row shows the results of the cases (i) to (iv) in Table 4.8 and bottom row shows the results of the cases (i) to (iv) in Table 4.9 from left to right).

the geometric properties of $L_y/L_x = 1$, $h/L_x = 0.1$, $\beta_1 = 0.25$ and $\beta_2 = 0.0$. Table 4.12 presents the first ten natural frequencies obtained for three different volumetric ratios ($p = 0.1$, $p = 1.0$, and $p = 10.0$). It is observed that Mori-Tanaka and theory of mixture methods lead to similar results, as also stated in [14]; however experimen-

Table 4.11 The computational cost comparison of cases studied in Table 2

	Case (i) (FFFF)		Case (ii) (CFFF)		Case (iii) (CFCF)		Case (iv) (CCCC)	
	ST	FEM	ST	FEM	ST	FEM	ST	FEM
DOFs	1680	107319	1848	107319	1848	107319	2457	107319
Duration (s)	2.79	78	3.4	67	3.26	82	6.89	73
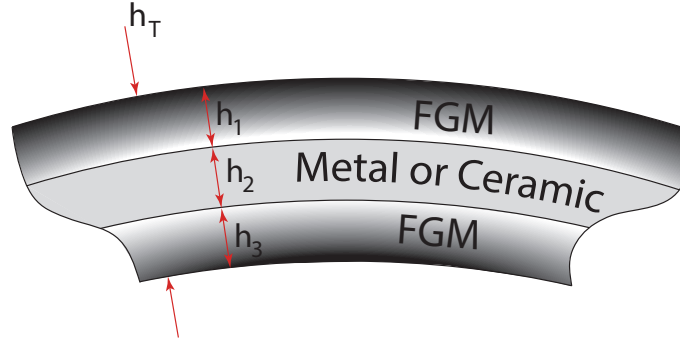
Figure 4.11 Schematic of a FG sandwich composite structure.

tation need to be done to determine the most accurate approach to characterize the varying material property.

Table 4.12 The comparison of first ten (non-dimensional) natural frequencies of an unconstrained cylindrical FG composite structure having the geometric properties of $L_y/L_x = 1$, $h/L_x = 0.1$, $\beta_1 = 0.25$ and $\beta_2 = 0.0$.

Mode	(i) $p = 0.1$		(ii) $p = 1.0$		(iii) $p = 10.0$	
	Mori-Tanaka	Theory of Mixtures	Mori-Tanaka	Theory of Mixtures	Mori-Tanaka	Theory of Mixtures
1	0.3981	0.4078	0.3674	0.3815	0.3779	0.3871
2	0.5656	0.5807	0.5211	0.5417	0.5374	0.5503
3	0.8944	0.9169	0.8244	0.8574	0.8456	0.8650
4	1.0719	1.0961	0.9951	1.0365	0.9854	1.0091
5	1.0747	1.0999	0.9957	1.0429	1.0091	1.0337
6	1.5567	1.5982	1.4330	1.4924	1.4692	1.5024
7	1.7762	1.8177	1.6436	1.7153	1.6550	1.6935
8	1.8081	1.8540	1.6651	1.7345	1.6989	1.7357
9	2.1257	2.1760	1.9686	2.0561	1.9770	2.0237
10	2.2375	2.2912	2.0706	2.1599	2.0925	2.1420

4.2.1.2 Laminated FGM parallelepiped

In this section, the dynamics of laminated doubly curved FG structures are studied. In this case study, two different FG sandwich configurations, as seen in Fig. 4.11, are considered: **(a)** soft-core and **(b)** hard-core. The first configuration is referred as the soft-core since the middle laminate is metal and outer layers are FGM. Similarly, the second configuration is hard-core since the middle layer is ceramic and outer layers are FGM.

Table 4.13 The comparison of natural frequencies (in Hz) of a soft-core FG ($p = 1$) sandwich cylindrical ($\beta_1 = 0.5$, and $\beta_2 = 0$) structure having the geometric properties of $L_x = 2.67$ m, $L_y = 3$ m, $h_T = 0.3$ m (where $h_2/h_1 = 2$ and $h_1 = h_3$).

| Mode | Case (i): FFFF | | | Case (ii): FCFC | | | Case (iii): CFCF | | | Case (iv): CCCC | | |
	ST	Ye *at al.*	FEM	ST	Ye *at al.*	FEM	ST	Ye *at al.*	FEM	ST	Ye *at al.*	FEM
1	171.2	171.2	171.2	414.3	418.6	414.1	340.2	343.0	340.1	674.7	678.1	674.6
2	220.2	220.2	220.2	562.5	565.0	562.2	401.9	404.6	401.8	845.3	850.9	845.5
3	327.4	327.3	327.4	564.5	568.0	564.3	484.4	486.5	484.3	1100.5	1104.7	1100.5
4	449.1	-	449.0	716.6	-	716.7	671.9	-	671.8	1134.1	-	1134.2
5	525.1	-	525.1	830.1	-	830.2	742.3	-	742.4	1272.1	-	1273.1
6	580.8	-	582.0	909.0	-	908.8	751.2	-	751.1	1311.3	-	1311.4
7	657.6	-	658.2	949.6	-	949.7	783.9	-	783.8	1348.6	-	1350.2
8	666.2	-	666.1	1147.6	-	1148.2	951.2	-	951.1	1506.1	-	1506.7
9	887.9	-	888.5	1206.7	-	1207.5	1093.2	-	1093.2	1523.6	-	1524.0
10	910.2	-	910.5	1222.3	-	1223.2	1183.6	-	1183.2	1555.7	-	1556.2

First, the dynamics of a soft-core FG sandwich cylindrical structure having the geometric properties of $L_x = 2.67$ m, $L_y = 3$ m, $h_T = 0.3$ m (where $h_2/h_1 = 2$ and $h_1 = h_3$, *i.e.* 1-2-1 configuration), $\beta_1 = 0.5$, and $\beta_2 = 0$ is investigated. The predicted natural frequencies are compared to those obtained from FE simulations and also to those found in the literature. For this purpose, a recent study done by Ye *et al.*, in which they investigated the dynamics of FG sandwich shells using cosine Fourier series together with the Rayleigh-Ritz approach, is used [12]. In this study, the material gradation in the FG layer is determined using theory of mixtures. For the analysis, they selected the constituent materials of the FGM doubly-curved structure to be aluminum as the metallic structure having the properties of $E_m = 70$ GPa, $\nu_m = 0.3$, and $\rho_m = 2707$ kg/m^3 and the ceramic structure having the properties of $E_c = 380$ GPa, $\nu_c = 0.3$, and $\rho_c = 3800$ kg/m^3. The volumetric amounts of the constituent materials are calculated based on power law, Eq. (2.34), and the material gradation parameter, p, is set to 1. The first ten natural frequencies (in Hz) are predicted under FFFF, FCFC, CFCF, and CCCC boundary conditions and listed in Table 4.14. Note that, in Ye *et al.*'s work only the first three natural frequencies are calculated; however, here we included the comparison of the first ten natural frequencies. As seen, the results are in excellent agreement to those calculated using FE approach, and to those presented in Ye *et al.*'s work [12]; the average and maximum percent differences in predicted natural frequencies are calculated as 0.03 % and 0.21 %, respectively.

Second, the dynamics of a hard-core FG sandwich spherical structure having the geometric $L_x = 1.34$ m, $L_y = 2.0$ m, $h_T = 0.3$ m (where $h_1 = h_2 = h_3$, *i.e.* 1-1-1 configuration), $\beta_1 = 0.25$, and $\beta_2 = 3/8$ is investigated. Similar to the previous case, the material gradation parameter, p, is set to 1. The calculated natural frequencies are compared using the FE results and the results presented in Ye *et al.*'s work [12]. Table 4.14 lists the first ten natural frequencies that are calculated under

Table 4.14 The comparison of natural frequencies (in Hz) of a hard-core FG (p=1) sandwich spherical ($\beta_1 = 1/4$, and $\beta_2 = 3/8$) structure having the geometric properties of $L_x = 1.34$ m, $L_y = 2.0$ m, $h_T = 0.3$ m (where $h_2/h_1 = 1$ and $h_1 = h_3$).

Mode	Case (i): FFFF			Case (ii): FCFC			Case (iii): CFCF			Case (iv): CCCC		
	ST	Ye *at al.*	FEM	ST	Ye *at al.*	FEM	ST	Ye *at al.*	FEM	ST	Ye *at al.*	FEM
1	430.4	430.5	430.4	1057.0	1060.8	1055.6	1188.9	1194.5	1188.3	1725.1	1726.8	1724.1
2	468.5	468.6	468.5	1074.9	1077	1074.4	1244.1	1247.9	1243.6	1991.1	1992	1990.5
3	923.7	923.8	923.6	1336.8	1337.7	1336.4	1467.3	1467.9	1467.1	2059.9	2062.9	2058.4
4	1098.8	-	1098.7	1483.0	-	1482.8	1605.2	-	1604.9	2588.7	-	2587.6
5	1166.7	-	1166.3	1518.5	-	1517.7	1713.1	-	1711.4	2651.4	-	2649.7
6	1460.9	-	1461.4	1792.2	-	1791.8	1789.3	-	1787.6	2699.6	-	2699.4
7	1732.9	-	1732.5	2155.3	-	2154.9	1941.5	-	1941.1	3231.4	-	3231.1
8	1908.4	-	1908.2	2296.0	-	2294.8	2232.2	-	2231.8	3250.8	-	3249.6
9	2021.6	-	2021.5	2320.7	-	2320.5	2572.7	-	2573.5	3449.5	-	3446.1
10	2082.9	-	2083.5	2449.3	-	2448.3	2782.9	-	2781.5	3471.6	-	3471.2
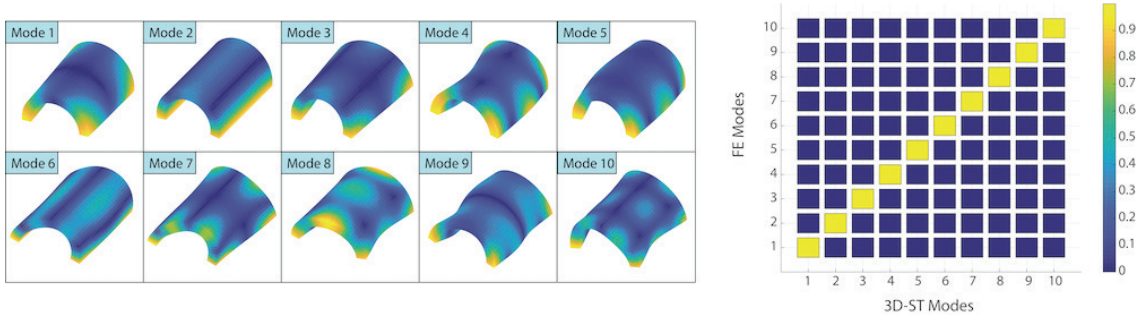
Figure 4.12 The first ten mode shapes and the corresponding MAC plot for the unconstrained soft-core sandwich composite given in Table 4.13.

FFFF, FCFC, CFCF, and CCCC boundary conditions. It is observed that the natural frequencies obtained using the ST solution match those obtained from the FE closely; the maximum difference is below 0.13 % for any boundary condition.

In both soft and hard core sandwich structures investigated here, the mode shapes are also calculated and validated using modal assurance criteria. The minimum MAC value for all the cases listed in Tables 4.13 and 4.14 is found to be 0.9915. As an example, Fig. 4.12 shows the first ten natural frequencies of the unconstrained soft-core structure and the corresponding MAC plot.

Due to the simplicity, numerical efficiency, and completely parameterized nature of the presented ST solution approach, it is possible to perform the analysis of the effects of different parameters on the dynamics of FG structures easily. As an example, we investigated the change of first three natural frequencies with **(1)** increasing gradation amounts for a hard-core FG sandwich spherical composite having the geometric properties of $L_x/L_y = 1$ m, $h_T/L_x = 0.3$ m (where $h_1 = h_2 = h_3$, *i.e.* 1-1-1 configuration), and $\beta_1 = \beta_2 = 0.25$; **(2)** increasing core thickness for a hard-core FG (p=0.8) sandwich spherical composite having the geometric properties of $L_x/L_y = 1$, $h_1/L_x = h_2/L_x = 0.1$, and $\beta_1 = \beta_2 = 0.25$. The results of the ST and
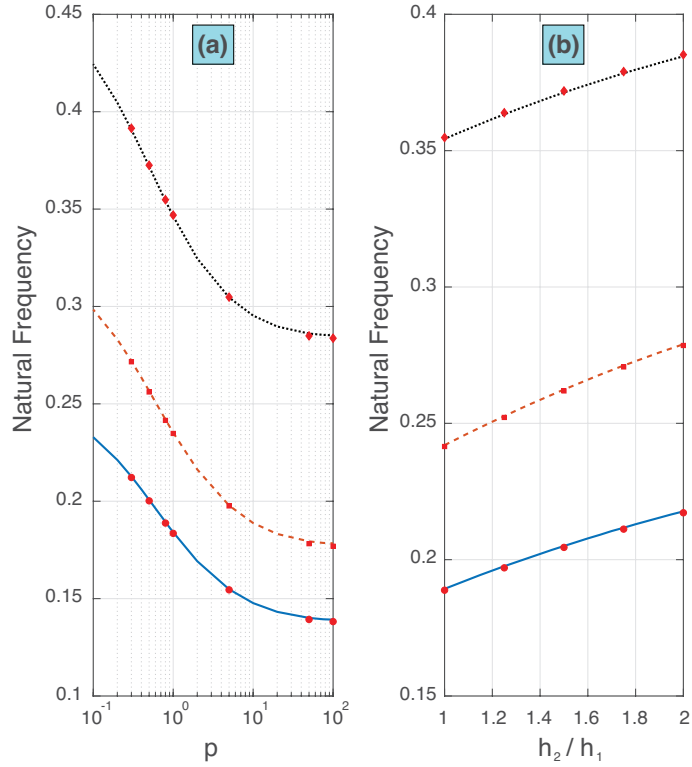
Figure 4.13 Variation of the first three non-dimensional natural frequencies of a spherical sandwich FG composite structure for **(a)** varying gradation parameter (p) and **(b)** varying core thickness (h_2/h_1). The solid (blue), dashed (red), and dotted black lines presents 1st, 2nd, and 3rd (non-dimensional) natural frequencies found using the ST approach. Similarly, circle, square, and diamond markers shoes the results of the FE simulations.

FE approaches with varying volume fraction parameter (p) and core thickness are plotted in Fig. 4.13. As observed, the natural frequencies are decreasing with decreasing the ceramic content or the core thickness of the structure, and the ST model matches very closely with the results of the FE (the maximum difference is 0.85 %).

4.2.1.3 Curved FG laminated structure having complex geometry

In this case study, to present the capability of the 3D-ST solution approach, curved FG laminated structures having complex/arbitrary geometries are investigated. As mentioned in Sec. 2.2.2, the presented solution technique enables accurately capturing the dynamics of structures having complex geometries using the one-to-one mapping procedure. This mapping procedure basically simplifies the domain of the problem (defined by the governing IBVP) through the Jacobian of mapping. To this end, the curved geometry as depicted in Fig. 4.14 is investigated.
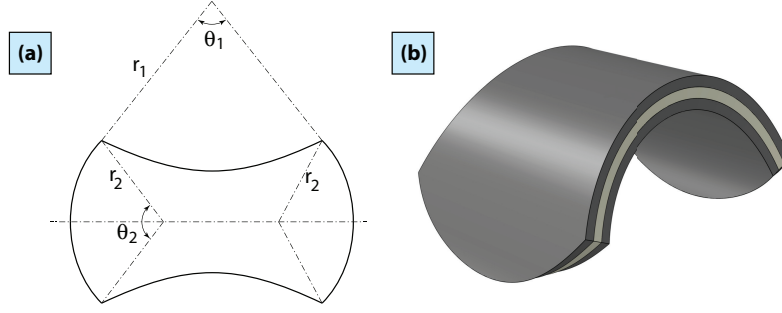
Figure 4.14 Laminated composite structure having arbitrary geometry: **(a-b)** in-plane geometry (in $x'' - y''$ plane) and curved three-dimensional model of the investigated geometry, respectively.

Table 4.15 The comparison of first ten natural frequencies (in Hz) of an unconstrained doubly-curved ($\beta_1 = 0.5$ and $\beta_2 = 0.0$) FG (p=0.7) soft-core sandwich lamina having a total thickness of $h_T = 0.3$ m, 0.4 m, and 0.5 m and thickness ratios of 1-1-1, 1-2-1, and 2-1-2, respectively, using the presented 3D-ST solution and 3D-FE simulations.

Mode	**(i)** 1-1-1			**(ii)** 1-2-1			**(iii)** 2-1-2		
	3D-ST	3D-FEM	Diff. (%)	3D-ST	3D-FEM	Diff. (%)	3D-ST	3D-FEM	Diff. (%)
1	68.98	69.05	0.09	85.39	85.44	0.06	98.33	98.39	0.07
2	106.66	106.66	0.00	132.83	132.77	0.04	152.38	152.27	0.07
3	202.04	202.25	0.10	246.70	246.85	0.06	272.43	272.38	0.02
4	206.82	206.87	0.03	249.02	248.99	0.01	277.86	278.08	0.08
5	395.54	395.72	0.05	470.36	470.37	0.00	503.84	503.80	0.01
6	396.31	396.43	0.03	473.46	474.33	0.18	521.08	522.52	0.28
7	567.38	564.19	0.56	666.90	666.75	0.02	644.23	643.99	0.04
8	628.90	628.98	0.01	671.31	668.39	0.44	737.00	735.18	0.25
9	641.22	639.84	0.22	754.97	754.52	0.06	791.51	791.53	0.00
10	682.53	682.53	0.00	762.38	763.12	0.10	811.57	813.25	0.21

In this case study, a doubly-curved soft-core sandwich composite structure (as depicted in Fig. 4.14(b)) having the curved (in-plane) geometry is considered. The material gradation amount for the outer layers is set to $p = 0.7$, and the curvature amounts are assumed to be $\beta_1 = 0.5$ and $\beta_2 = 0.0$. The total thickness of the sandwich composite structure is varied as $h_T = 0.3$ m, 0.4 m, and 0.5 m and the corresponding thickness ratios of each sub-cases are set to $h_1/h_2 = 1$, $h_1/h_2 = 0.5$, and $h_1/h_2 = 2$, respectively (note that the thicknesses of the outer layers are assumed to be equal, $h_1 = h_3$). The first ten natural frequencies calculated using the presented 3D-ST approach and FEM analysis are listed in Table 4.15. As observed, the results found using the 3D-ST approach accurately matches to those found using FE approach. The average and maximum differences in results are obtained to be 0.1 % and 0.56 %, respectively.

Similar to previous case studies, the mode shapes are also calculated using the
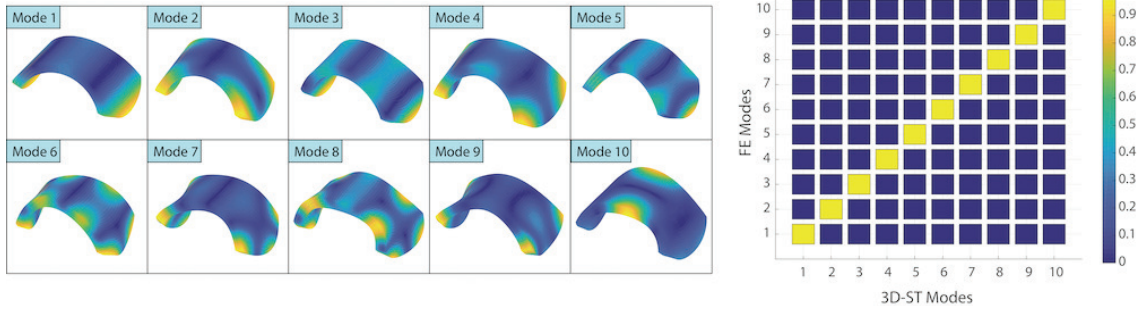
Figure 4.15 The first ten mode shapes and the corresponding MAC plot for the case (i) where the thickness ratio is selected as 1-1-1 (in Table 4.15.

presented solution technique and compared to those found using COMSOL. Modal assurance criteria is used to assess the consistency of the mode shapes obtained by these two approaches. Figure 4.15 shows the first ten mode shapes of the soft-core case study where the thickness ratio is selected as 1-1-1. Based on these analyses, the minimum MAC value is calculated as 0.9941; therefore we can conclude that the mode shapes obtained by the ST technique are in excellent agreement to those found by FE approach.

4.3 Sandwich structure with carbon nanotubes face-sheets and honeycomb type core

This section, the 3D-ST method is developed to study and design the straight and curved sandwich structures. The hexagonal type of honeycomb as a core layer of sandwich structure is reinforced by the face-sheets, including CNTs within porous media. CNTs distribute along the thickness of face-sheets with two symmetric, one anti-symmetric and uniform form. To validate the presented approach, vibration and static studies are conducted by obtaining the natural frequencies and deformation, respectively. The design process is accomplished using the Pattern Search algorithm to optimize the CNTs orientations to maximize the fundamental frequency and minimize the displacement.

4.3.1 Model Validation

The 3D-ST approach explained in section. 3.2 is validated through studying the vibration and static behavior of the straight and curved sandwich structure. For this purpose, the face-sheets contain CNT particles where the CNTs distribution

along the thickness of the layers are the same for both face-sheets as $FG-O$ type of distribution. The distribution type defined in Eq. 2.51 is utilized for the variation of porosity along the thickness. The CNTs material properties are presented in Table. 4.16 and 4.17. The middle layer is defined as a hexagonal honeycomb with the mechanical properties presented in Table. 4.18. For the vibration analysis, all edges are clamped. For the bending study the clamped boundary condition is applied at $y = L_y$ edge where a line force is applied on the edge $y = 0$ as shown in Fig. (2.7)a. The obtained results from the 3D-ST approach are compared to those calculated with the FE method. The finite element approach is accomplished by using COMSOL v5.5.

Table 4.16 Material properties of CNTs composite

material	Elasticity(Pa)	Poisson ratio	Shear elasticity(Pa)	Density($\frac{kg}{m^3}$)
CNT	E11=5.6466×10^{12}	$\nu_{12} = \nu_{13} = 0.175$	$G_{12} = G_{G13} = 1.9445 \times 10^{12}$	1400
	$E_{22} = E_{33} = 7.08 \times 10^{12}$	$\nu_{23} = \nu_{21}$	$G_{23} = \frac{1}{2}\frac{E_{22}}{1+\nu_{23}}$	
Matrix	2.1×10^9	0.34	-	1150

Table 4.17 CNT material parameters

V^*_{CNT}	η_1	η_2	η_3
0.11	0.149	0.934	0.934
0.14	0.150	0.941	0.941
0.17	0.149	1.381	1.381
0.28	0.141	1.585	1.109

Table 4.18 Material properties of hexagonal honeycomb structure

Elasticity(Pa)	Poisson ratio	Shear elasticity(Pa)	Density($\frac{kg}{m^3}$)
$E_{11} = 0.0354 \times 10^6$	$\nu_{12} = 0.999856$	$G_{12} = 0.0266 \times 10^6$	
$E_{22} = 0.0354 \times 10^6$	$\nu_{13} = 0$	$G_{13} = 92.463 \times 10^6$	24.94
$E_{33} = 655.87 \times 10^6$	$\nu_{23} = 0$	$G_{23} = 141.12 \times 10^6$	

4.3.1.1 Straight sandwich structure

In this section, vibration and bending analysis of a square layered structure are studied. The non-dimensional geometry properties are $L_x/L_y = 1$ with two different thickness to length ratios of $h_t/L_y = 0.1$ and 0.2. Also, the ratio of face-sheets to the middle layer is $h_o/h_m = 0.5$. The number of polynomials used to model the structure to accomplish the vibration and static studies is 11×11 in x and y directions. Also, the number of polynomials in the thickness direction is set to 7, 5, and 7 for

the bottom face-sheet, core layer, and upper face-sheet, respectively. After applying the coupling conditions, the overall degrees of freedom decreased to $3\times11\times11\times17$. Table. 4.19 shows the first five natural frequencies of a square thick structure for different porosity parameters (e_0) and different CNTs orientations$[\psi_1,\psi_2]$, where ψ_1 and ψ_2 are the bottom face-sheet and top face-sheet CNTs orientations, respectively. The results are compared to those obtained from the FE analysis. The error percentage indicates that the 3D-ST approach can predict the vibration behavior of the sandwich structure accurately. The bending analysis of the aforementioned struc-

Table 4.19 Natural frequencies (Hz) of straight structure with different porosity values and CNTs orientations$[\psi_1,\psi_2]$.

h/a	Modes	$e_0 = 0.1$ [30,60]			$e_0 = 0.3$ [-45,45]			$e_0 = 0.5$ [60,30]		
		3D-ST	FEM	Diff (%)	3D-ST	FEM	Diff (%)	3D-ST	FEM	Diff (%)
	1	96.80	96.69	0.12%	91.29	91.15	0.15%	96.71	96.52	0.19%
	2	153.51	153.32	0.12%	156.66	156.46	0.12%	153.21	152.92	0.19%
0.1	3	174.56	174.42	0.08%	163.31	163.08	0.14%	173.79	173.51	0.16%
	4	210.70	210.44	0.12%	222.71	222.44	0.12%	210.13	209.74	0.18%
	5	245.90	245.72	0.07%	237.32	237.05	0.11%	245.17	244.78	0.16%
	1	123.71	123.65	0.05%	123.00	122.90	0.08%	123.17	123.02	0.13%
	2	192.16	191.97	0.10%	198.30	198.08	0.11%	190.84	190.56	0.15%
0.2	3	215.57	215.39	0.08%	207.41	207.15	0.12%	211.63	211.33	0.14%
	4	259.46	259.18	0.11%	272.20	271.83	0.13%	258.14	257.74	0.15%
	5	275.98	275.04	0.34%	290.54	290.14	0.14%	261.16	260.44	0.28%

ture is accomplished by calculating the displacement magnitude of the center of the structure on the top surface of the upper face-sheet. The acting force is described in section 4.3.1. However, for the thickness ratios of 0.1 and 0.2, the line force amount is 10^6 N/m. Table. 4.20 indicates the displacements $(\frac{\delta}{L_y})$ of the structure with different CNTs volume percents and various CNT orientations. Comparing obtained results with the FE approach solutions shows that the 3D-ST approach can obtain accurate results in static studies.

Table 4.20 Bending analysis of straight structure for different volume and orientations$[\psi_1,\psi_2]$ of CNTs.

h/L$_x$	$V^*_{CNT} = 0.11$ [30,60]			$V^*_{CNT} = 0.13$ [-45,45]			$V^*_{CNT} = 0.17$ [60,30]		
	3D-ST	FEM	Diff%	3D-ST	FEM	Diff%	3D-ST	FEM	Diff%
0.1	0.4150	0.4184	0.82%	0.5892	0.5944	0.88%	0.2877	0.2902	0.86%
0.2	0.0710	0.0717	0.99%	0.0887	0.0894	0.81%	0.0518	0.0522	0.75%

4.3.1.2 Single-curved sandwich structure

In this section, a single curved sandwich structure's vibration and static behaviors are investigated to validate the presented approach. Considering the Fig. 2.7a, the geometry properties for this study are $\frac{L_x}{R} = \frac{\pi}{2}$, $\frac{L_y}{R} = 3$ and $\frac{h_t}{R} = 0.3$ and 0.6. The curvature amount(β) is set to 0.25. The material property configuration and the type of boundary conditions were described in the section. (4.3.1). The vibration and static investigations are accomplished for different volume percentages and various orientations of CNTs[ψ_1, ψ_2]. Vibration study of the single-curved structure is conducted by obtaining the first five natural frequencies shown in Table. 4.21. The results show an excellent agreement between the 3D-ST approach and the FE method. It should be noticed that to study the curved layered thick structure, the 3D-ST approach employs $13 \times 13 \times (7 \times 5 \times 7)$ polynomials in X, Y and Z directions, respectively. Consequently, considering the boundary condition, the number of degrees of freedom is 7293 for the 3D-ST approach. This number is equal to 40000 for the FE method. Hence, it can be concluded that decreasing the number of degrees of freedom results in decreasing the computational time.

The static behavior of a curved sandwich structure is studied via investigation of

Table 4.21 Natural frequencies (Hz) of the curved sandwich structure for different porosity values and various CNTs orientations[ψ_1, ψ_2].

h/a	Modes	$e_0 = 0.1$ [30,60]			$e_0 = 0.3$ [-45,45]			$e_0 = 0.5$ [60,30]		
		3D-ST	FEM	Diff%	3D-ST	FEM	Diff%	3D-ST	FEM	Diff%
	1	272.89	272.76	0.05	270.15	269.99	0.06	269.31	269.15	0.06
	2	292.46	294.75	0.78	294.33	295.12	0.27	280.78	281.76	0.35
0.1	3	307.00	306.88	0.04	308.73	309.47	0.24	305.40	305.20	0.07
	4	356.64	358.61	0.55	354.35	354.43	0.02	344.10	344.71	0.18
	5	367.47	367.48	0.00	381.42	382.38	0.25	362.49	362.36	0.04
	1	266.24	266.58	0.13	261.80	261.57	0.09	257.39	257.21	0.07
	2	299.11	298.68	0.15	301.95	302.15	0.07	286.37	286.84	0.16
0.2	3	315.72	315.81	0.03	324.73	325.53	0.24	305.89	305.74	0.05
	4	383.20	382.83	0.10	361.62	361.25	0.10	367.30	367.58	0.08
	5	394.15	393.82	0.08	377.09	377.21	0.03	378.44	378.37	0.02

the structure's displacement using the 3D-ST approach. The boundary condition type and line load are described in the section. 4.3.1. Three different volume percent of CNTs are defined for the face-sheets with various orientations[ψ_1, ψ_2]. The applied load on the edge for thickness ratios of 0.3 and 0.6 are 10^5. Table. 4.22 indicates the comparison of displacements at the center of the structure between the presented approach and the FE method. The results show that the 3D-ST approach can predict the proper static displacement of a thick sandwich structure with complex geometry.

In the following, a parametric study is accomplished to present the CNTs orientations effect on the displacement and fundamental natural frequency of a described

Table 4.22 Bending analysis of a curved sandwich structure with different volume and orientations$[\psi_1, \psi_2]$ of CNTs

| | $V_{CNT}^* = 0.11$ | | | $V_{CNT}^* = 0.13$ | | | $V_{CNT}^* = 0.17$ | | |
| | [30,60] | | | [-45,45] | | | [60,30] | | |
h/a	3D-ST	FEM	Diff%	3D-ST	FEM	Diff%	3D-ST	FEM	Diff%
0.1	0.0307	0.0304	0.93	0.0401	0.0399	0.53	0.0236	0.0233	0.94
0.2	0.0060	0.0060	0.51	0.0073	0.0073	0.78	0.0045	0.0045	0.85

geometry in this section. The structure is clamped at $y = 0$ edge. The CNTs volume is set to 0.17. The results are plotted and shown in Fig. 4.16. The results show that the CNTs orientations effect the static and dynamic behavior of the structure significantly. For the presented case of structure, the structure indicates to be more stiff around the zero orientation of CNTs. The validation is accomplished for some cases and shown on the figure with black circles. Obviously, the CNTs orientations of the upper or bottom face-sheets have a recognizable effect on the structure behavior. For instance, for two points marked with red stars on the Fig. 4.16a and b for the displacement and fundamental natural frequency studies, the CNTs orientations are [-50,0], [0,-50] and [-70,0], [0,-70], respectively. It shows that the behavior of the structure is not symmetric relative to the CNTs orientations, where the percent of differences are 5% and 10% for displacement and fundamental natural frequency, respectively. This issued can be caused by the curvature complexity which leads to have the variation of length in X axis for bottom and upper face-sheets. The parametric study shows that the CNTs affect on the structure static and dynamic behavior is significant and a design studies should be conducted to obtain a desired decision.

4.3.2 Design of sandwich-structured composites

This section aims to optimize the CNTs orientations of face-sheets ($[\psi_1, \psi_2]$) to catch the desired dynamic and static behavior. The objective functions of the optimization are maximizing the fundamental natural frequency(ω_f) and minimizing the deflection of the center point of the upper face-sheet(δ), separately. The contained CNTs of each face-sheet has independent orientations defined as the design variables of this optimization study. Mathematically, the optimization study can be written as;

$$\text{Objective function}: \quad \text{Maximum} \;\; \omega_f \;\; or \;\; \text{Minimize} \; \delta$$
$$\text{Design variables}: \quad [\psi_1, \psi_2] \qquad\qquad\qquad\qquad (4.3)$$
$$\text{Bounds}: \quad -\frac{\pi}{2} < \psi_1 < \frac{\pi}{2}, \quad -\frac{\pi}{2} < \psi_2 < \frac{\pi}{2}$$
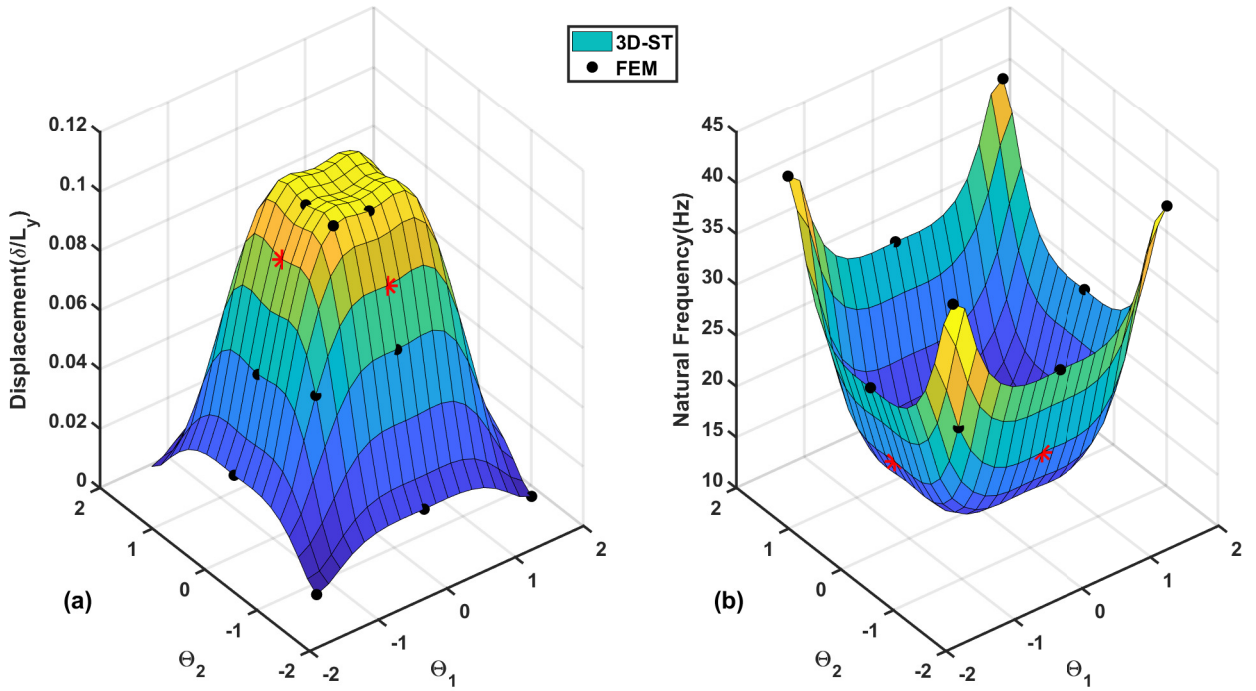
Figure 4.16 Parametric study of CNTs orientations effect on the (a) displacement and (b) fundamental natural frequency of a sandwich structure

To solve the optimization problem, the Pattern Search(PS) method presented by Hooke and Jeeves[159]is used, which is a member of the Generalized Pattern Search (GPS) algorithms. This method is presented as a local optimization theory. However, this method has valuable characteristics compared to the global optimization algorithms such as Genetic Algorithm(GA)[160]. The initial mesh size is set to 1, which can change with the basis of 2. For the optimization step, geometry of structure is set to two thickness ratios ($\frac{h}{L_y} = 0.1, 0.2$) and five curvature amounts ($\beta = 0.1, 0.2, 0.3, 0.4, 0.5$). Also, four case of CNT distributions along the thickness of face-sheets ($FG-X, FG-O, FG-V$ and UD) with four value of volume percentage of CNTs ($V^* = 0.11, 0.14, 0.17$ and 0.28) are defined. The porosity distribution is set to the symmetric equation presented in Eq. 2.52 with porosity coefficient of $e_0 = 0.3$. The boundary conditions for the natural frequency and displacement optimizations are defined as all-edges clamped and one-edge clamped at $(y = L_y)$, respectively. Also, in the case of displacement optimization, line force is applied to the half part of the $y = L_y$ edge of the upper face-sheet in Z direction with the value of $10^6 \frac{N}{m}$(shown in Fig. 2.7 with the red color.

4.3.2.1 Fundamental natural frequency optimization

In this section, the optimum CNTs angle of upper and bottom face-sheets are obtained to maximize the fundamental natural frequencies. Table. 4.23 presents the optimum CNT angles and obtained maximum fundamental natural frequencies related to the optimum CNT angles. It should be noticed that each row of results includes optimum CNTs orientations$[\psi_1, \psi_2]$ and maximum fundamental natural frequency(ω_f). In an overview, Table. 4.23 shows that the optimum CNT angles highly depend on the geometry and material properties of the sandwich structure. For instance, the change of curvature amount (β) results in the mode shape jump, leading to changes in the optimum CNT angles. However, optimum CNT angles are changed for different thickness ratios with the same curvature amounts. On the other hand, It is clear that the structure tends to have a higher fundamental natural frequency due to the curvature amount. However, it can be concluded that for higher curvature amounts, the increment of fundamental natural frequency has a slow growth, whereas it decreases after a specific curvature amount (here β=0.4). Another part of this optimization study is to present the effect of material variation on the optimum CNT angles and maximum fundamental natural frequency. Table. 4.23 indicates that the distribution type of CNTs along the thickness has a small effect on the obtained optimum CNT angles. However, the results show that geometry parameters are more effective on the CNTs angles than the material characteristics. To highlight the material and geometry complexity effects on the optimization process, the maximum fundamental natural frequencies are presented in Table. 4.23. Considering the curvature amount, it is clear that CNTs distribution type can affect the maximum fundamental natural frequency approximately 1% to 5% with the same volume of CNTs. The CNTs distribution type effect is more comprehensible when the CNT volume and curvature amounts have higher values. A substantial point about the CNT volume role is that increasing the CNTs volume increases the natural frequency. However, the increase of optimum natural frequency does not have a meaningful relation with the increase of CNTs volume. For instance, change of the contained volume of CNTs from 0.14 to 0.17 (+21%) results in an 18% increment of optimum fundamental natural frequency, approximately, where this volume changes from 0.11 to 0.14 (+27%) result in 3% increment of optimum fundamental natural frequency. This issue is related to the CNTs efficiency parameters (η_i) obtained from the molecular dynamic analysis of CNTs. To show the optimization importance, Fig. 4.17 indicates the comparison of optimum fundamental natural frequencies to those obtained for the [0,0] angle of CNTs for upper and bottom face-sheets. Fig. 4.17 is accomplished for different types of CNT distributions, thickness ratios, and curvature amounts, where the CNTs volume is set to 0.11. The results show that the fundamental natural frequency can be increased 45% at most by designing the CNTs orientations. As shown in Fig. 4.17,

Table 4.23 Optimized CNT orientations of upper and bottom face-sheets $[\theta_1,\theta_2]$ and maximum fundamental frequencies.

V*	β	$\frac{h}{L_x}=0.1$				$\frac{h}{L_x}=0.2$			
		FG-X	FG-O	FG-V	UD	FG-X	FG-O	FG-V	UD
0.11	0.1	[0,0] 149.2	[0,0] 146.5	[0,0] 148.2	[0,0] 150.2	[0,0] 158.6	[0,0] 154.7	[0,0] 156.7	[0,0] 158.3
	0.2	[0,0] 162.8	[0,0] 160.3	[0,0] 161.6	[0,0] 162.6	[0,0] 167.5	[0,0] 165.3	[0,0] 166.4	[0,0] 167.1
	0.3	[-50, -35] 165.2	[-45,-35] 161.0	[-45,-40] 161.9	[-50,-35] 163.8	[55,0] 202.1	[55,5] 171.0	[50,0] 171.9	[55,0] 173.1
	0.4	[-60,60] 171.9	[-60,60] 167.0	[-60,60] 169.0	[-60,60] 169.9	[-65,60] 182.6	[-60,55] 177.2	[-60,55] 178.9	[-65,60] 180.5
	0.5	[-60,70] 170.9	[-60,70] 165.9	[-60,70] 167.7	[-60,70] 168.9	[-55,55] 182.4	[-55,55] 177.5	[-55,50] 178.3	[-55,60] 180.6
0.14	0.1	[0,0] 153.8	[0,0] 151.1	[0,0] 152.7	[0,0] 154.3	[0,0] 162.5	[0,0] 158.7	[0,0] 160.6	[0,0] 161.8
	0.2	[0,0] 166.6	[0,0] 163.9	[0,0] 165.3	[0,0] 165.9	[0,0] 170.8	[0,0] 168.5	[0,0] 169.6	[0,0] 169.9
	0.3	[-50,-35] 168.5	[-50,-40] 164.5	[-45,-40] 164.8	[-50,-35] 166.7	[55,0] 177.6	[55,-10] 173.7	[50,0] 174.8	[55,0] 175.8
	0.4	[-60,60] 175.8	[-60,60] 170.5	[-60,60] 172.5	[-60,60] 173.3	[-65,60] 186.2	[-65,60] 180.7	[-60,60] 182.2	[-65,60] 183.8
	0.5	[-60,70] 174.4	[-60,70] 168.8	[-60,70] 170.7	[-60,70] 171.9	[-60,55] 185.7	[-55,55] 180.4	[-55,55] 181.7	[-55,60] 183.9
0.17	0.1	[0,0] 180.6	[0,0] 176.6	[0,0] 178.9	[0,0] 180.6	[0,0] 189.2	[0,0] 183.5	[0,0] 186.3	[0,0] 187.7
	0.2	[35,0] 192.8	[45,0] 186.1	[45,10] 187.4	[35,-5] 190.2	[0,0] 201.0	[0,0] 197.4	[0,0] 199.0	[0,0] 199.2
	0.3	[-35,40] 198.3	[-35,40] 191.4	[-40,40] 194.0	[-40,35] 195.2	[0,50] 206.3	[-10,45] 200.5	[-15,35] 202.5	[0,50] 203.2
	0.4	[-60,60] 205.4	[-60,60] 197.6	[-60,60] 200.3	[-60,60] 201.4	[-55,60] 217.0	[60,55] 209.6	[-55,55] 211.6	[-60,60] 213.6
	0.5	[-60,70] 199.7	[-60,65] 192.1	[-60,65] 194.6	[-60,70] 196.0	[-55,55] 214.4	[-55,55] 206.4	[-55,50] 207.6	[-65,65] 210.6
0.28	0.1	[0,0] 185.4	[0,0] 182.0	[0,0] 183.0	[0,0] 180.7	[0,0] 192.3	[0,0] 187.8	[0,0] 189.0	[0,0] 186.8
	0.2	[30,0] 194.8	[40,0] 189.2	[35,-5] 190.3	[30,0] 188.7	[0,0] 200.8	[0,0] 197.6	[0,0] 198.0	[0,0] 194.8
	0.3	[-60,40] 200.1	[-55,40] 193.6	[-55,40] 194.9	[-60,40] 192.8	[55,0] 206.8	[-60,55] 200.5	[-5,50] 201.7	[55,0] 200.1
	0.4	[-60,65] 208.2	[-60,65] 200.4	[-60,65] 202.1	[-65,65] 200.9	[-60,65] 217.5	[-60,60] 210.9	[-60,60] 211.6	[-65,60] 210.5
	0.5	[-55,70] 201.5	[-60,70] 193.2	[-60,70] 194.9	[-60,70] 194.8	[-55,60] 214.2	[-55,60] 206.3	[-55,60] 207.6	[-55,60] 207.4

the optimization is more effective in higher curvature amounts. In general, it can be detected that optimization can change the dynamic behavior of the structure. For instance, Fig. 4.17 shows that the sandwich structure with [0,0] orientations of CNTs, tends to decrease the fundamental natural frequency for higher curvature amounts, where the optimum CNTs orientations behave in the opposite direction.
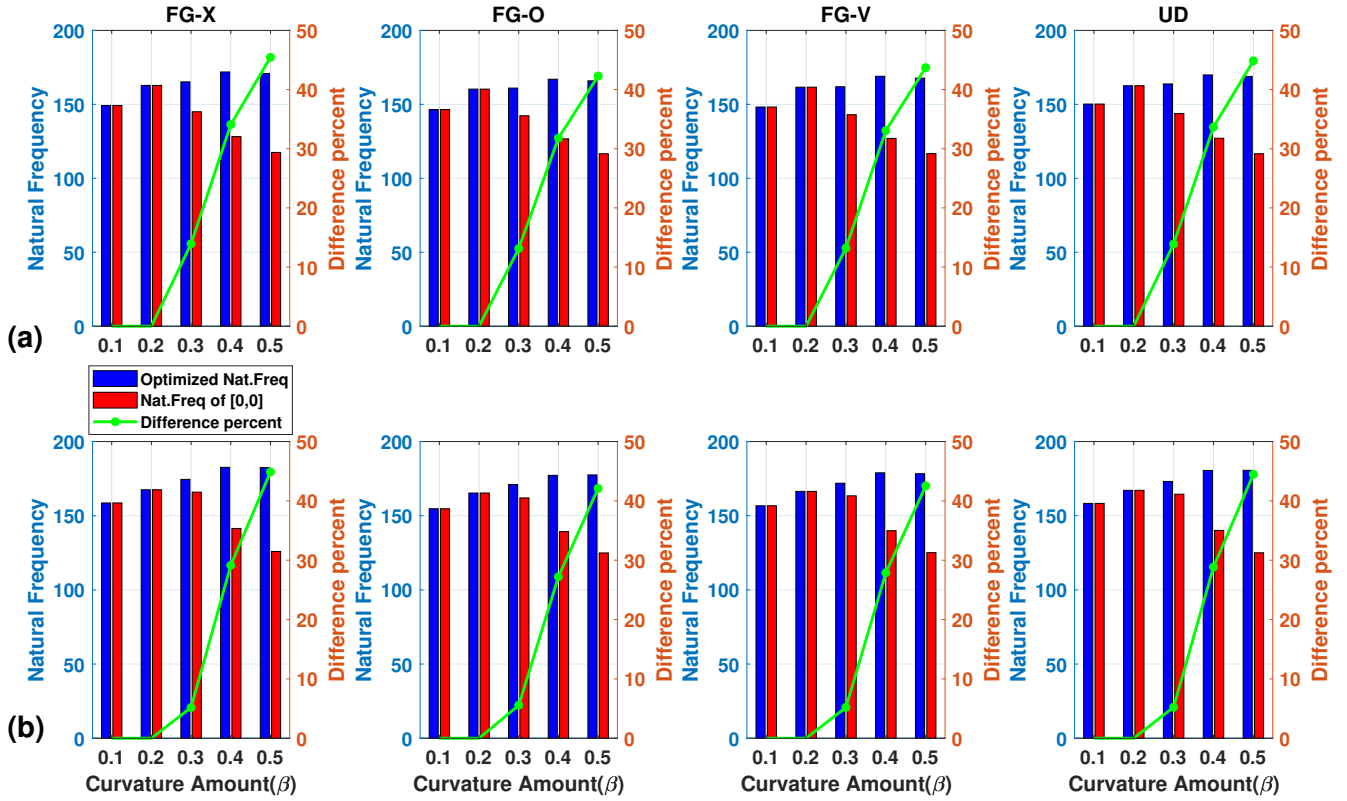
Figure 4.17 Comparison of the optimum natural frequency and the obtained fundamental frequency by set of [0,0] orientation for the face-sheets for different CNT distributions; (a) $h/L_x = 0.1, (b) h/L_x = 0.2$.

4.3.2.2 Optimization of static behavior of a sandwich structure

In this section, the optimization study of the static behavior of the sandwich structure is accomplished to minimize the displacement of the center of the top surface of the upper face-sheet. The CNTs orientations of the face-sheets are designed to catch the minimum displacement. Fig. 4.18 shows the comparison of the optimized displacement and the displacement with [0,0] CNTs orientations of face-sheets. The CNTs distribution is $FG - X$ in this section. The comparison indicates that the CNTs orientations significantly affect the displacement of sandwich structure with

honeycomb core. It should be noticed that the line force is applied to the half-edge of the structure, which leads to having a torsion moment and shear stress. In this regard, the honeycomb structures cannot tolerate that stress effectively, because of their structural characteristics. It is obvious that for the lower thickness ratio (Fig. 4.18a), the percentage of improvement is too high in comparison to the higher thickness ratio(Fig. 4.18b). Also, it is shown that increasing the curvature follows the making the optimized CNTs orientation role less effective in minimizing the displacement. On the other hand, the mentioned issue is confirmed for the volume percentage of CNTs role, where for the lower volume percentage of CNTs the design study should be considered a determinant element of analysis.

Another design study is conducted using the aluminum core to show the structure behavior in different conditions. The same boundary condition, line load, and CNTs material properties are included in this study. The elasticity modulus, Poisson ratio and density of the aluminum are 70 Gpa, 0.34 and 2700 kg/m^3, respectively. Fig. 4.19 shows the displacement results for the optimized and [0,0] orientations of CNTs displacements. In comparison to the sandwich structure with a honeycomb core(Fig. 4.19), curvature effect shows the same trend of decreasing. In general, it can be seen that the improvement percentage is decreased in comparison to the sandwich structure with a honeycomb core. The variation of volume of CNTs shows a vice versa effect compared to its effect on the honeycomb case, where the percent of improvement of displacement increases with the increase of the volume of CNTs. Also, the same trend is detected for the thickness ratio, wherein the case of aluminum core, for the high thickness ratio ($\frac{h}{L_y} = 0.2$), the percentage of the difference between optimized orientations and [0,0] case is higher than the lower thickness ratio ($\frac{h}{L_y} = 0.2$). In conclusion, the design approach strongly depends on the geometry complexities and material properties, which can be an interesting field to be investigated in more detail.
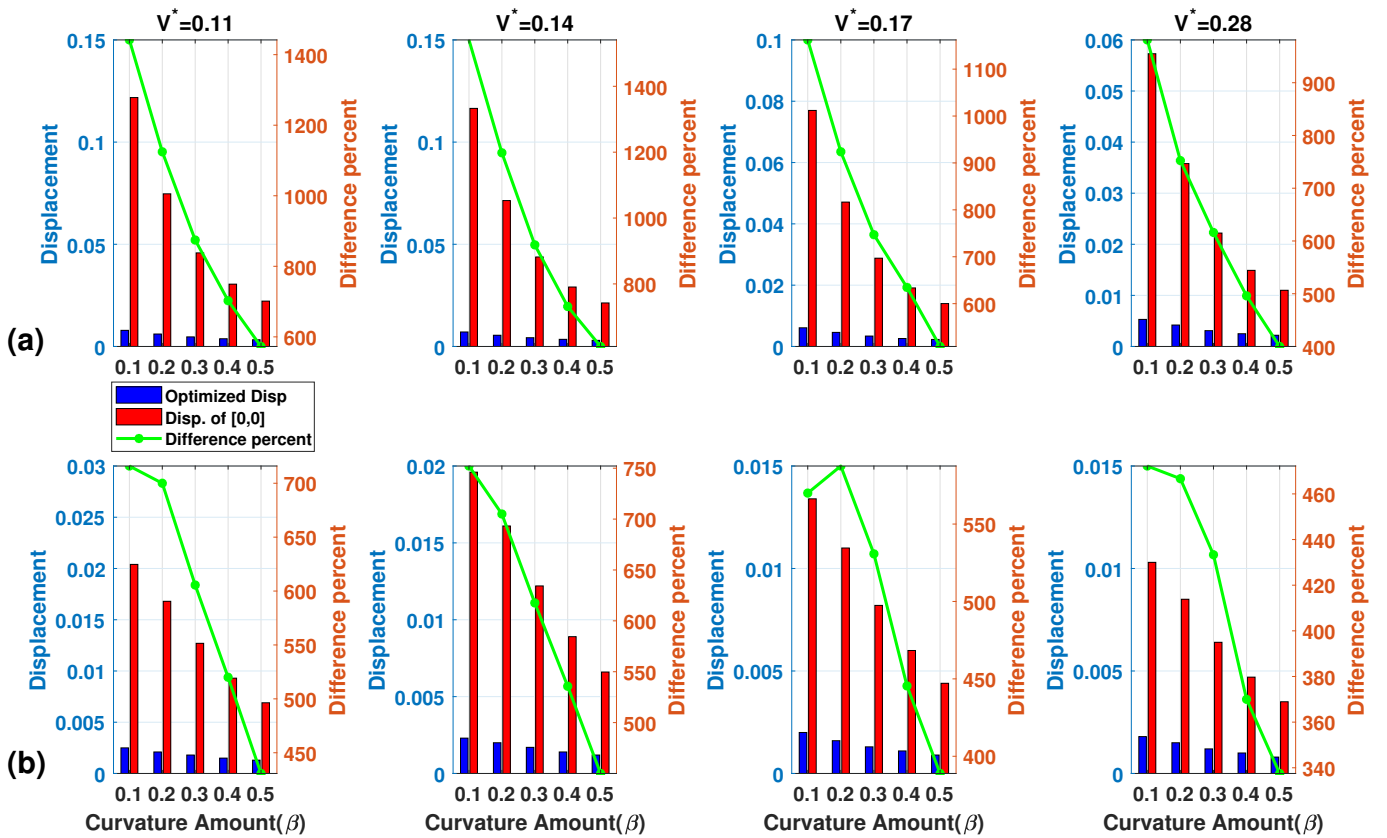
Figure 4.18 Comparison of the minimum displacement with optimum CNT angles and obtained displacement of the sandwich structure with [0,0] orientation of the CNTs for different volume of CNTs; (a) $h/L_y = 0.1$, (b) $h/L_y = 0.2$.
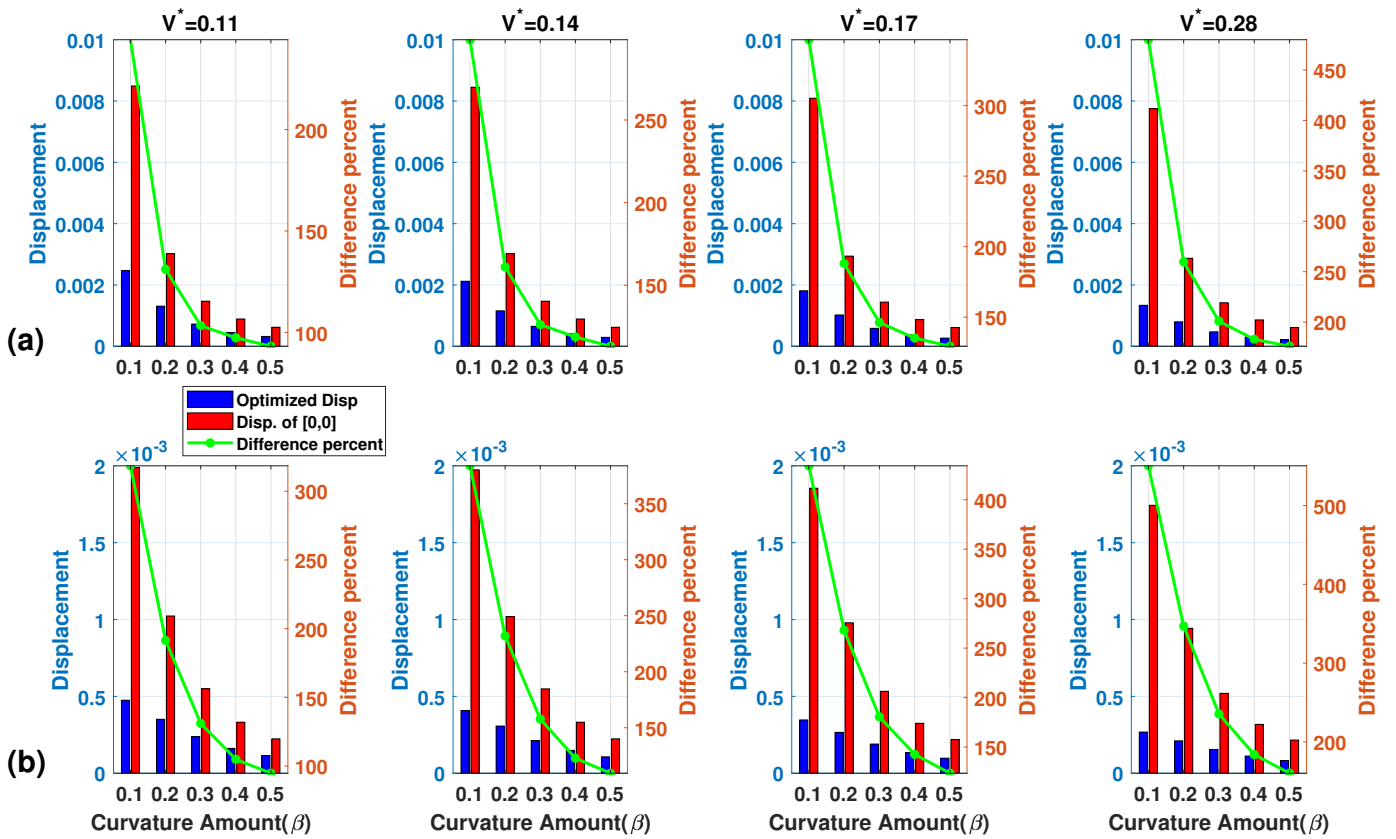
Figure 4.19 Comparison of the minimum displacement with optimum CNT angles and obtained displacement of the sandwich structure with [0,0] orientation of the CNTs for different volume of CNTs and aluminum core; (a) $h/L_y = 0.1, (b) h/L_y = 0.2$.

5. CONCLUSIONS

5.1 Results and discussion

In this study, we presented a general 2D and 3D spectral-Chebyshev modeling approach to obtain high-fidelity dynamic models for laminated or sandwich (doubly-) curved (FG) composite structures. The Hamilton energy approach is utilized to obtain the integral boundary value problem. The Chebyshev polynomials are used to approximate the function due to their exponential convergence characteristics. The derivative operator is obtained using the expansion of a function, where the inner product approach accomplishes the integral operation. Furthermore, the domain is discretized using the Gauss-Lobatto points.

The performance of the solution approach in terms of accuracy and computational efficiency is shown through various case studies. For comparison, the reference solutions are obtained either using a commercial FE software (COMSOL) or data available in literature. Since, the solution approach uses mapping algorithms (coordinate transformation) to simplify the domain, the vibrational behavior of composite laminated structures having complex geometries can be accurately identified. Furthermore, due to the parametrized nature of the presented solution approach, it is possible to efficiently perform various parametric analyses.

Based on the studies performed, following the conclusions can be obtained:

- In all case studies (both using 2D and 3D spectral Chebyshev approach), it is shown that the results obtained using the presented solution approach are in excellent agreement to those found in literature or to those obtained using FE analysis. The maximum differences are calculated to be less than 1 % corresponding to literature and FE result. To validate the predicted mode shapes, modal assurance criteria is used and MAC plots are obtained for each case study. The minimum MAC value is calculated to be 0.8 for the symmetric (repeated) modes; note that the average MAC value for the investigated cases

76

are above 0.95.

- Based on the computational efficiency analyses performed in the same computing environment, the presented solution approach provides analysis speed-ups at least 30 folds compared to FE methods. The main reason due to this advantage is the significant decrease in the number of degrees of freedom to achieve the same level of accuracy.

- As expected, the increasing porosity decreases the stiffness of the plate leading to lower uniaxial/biaxial buckling loads. However, since the mass of the structure decreases with porosity, it has a minor effect on natural frequencies. On the other hand, as the reinforcement amount increases (either in the case of CNT or GPL reinforcement), there is a significant improvement in the stiffness of the structure.

- Due to the fact the GPLs are a type of 2D nanofillers, significant improvements are observed compared to CNT reinforcements. This finding is consistent with the literature, since it has been reported that the GPLs showed better mechanical enhancement as a result of the increased interaction between the nanofiller and matrix materials [47, 48, 42].

- Note that the developed model can also be extended **(i)** to different distribution profiles including asymmetric distributions considering the chance in the neutral surface [161] or **(ii)** to the analysis of curved composite panels by including a curvilinear coordinate frame and updating Eq. (2.2) accordingly. In the future, this modeling technique can be utilized to optimize the gradation profile and wt.% of the reinforcement amount in composite panels exploiting its numerically efficient and accurate nature.

- To leverage the computational efficiency, design studies are performed for sandwich structures. The CNTs orientations are designed to obtain the maximum fundamental natural frequency and minimum displacement, respectively. The pattern search method is used as an optimization algorithm. It can be concluded that in both dynamic and static optimization processes, the optimum CNTs orientations highly depend on the geometry and material characteristics. To comprehend the advantage of optimization, we compared the optimum CNT orientations and [0,0] orientations of CNTs. The results show that dynamic and deformation behavior (with defined objective functions) are enhanced approximately 45% and 1000%, respectively.

5.2 Future work

In this thesis, the 2D and 3D spectral Chebyshev technique is presented. It is possible to extend this study in different aspects such as **(i)** flexibility for different geometries, **(ii)** material complexities, and **(iii)** various different engineering problems.

In this thesis, although complex geometries such as singly or doubly curved geometries are studied, due to the nature of the spectral technique, the geometry needs to be expressed higher order polynomials; thereby necessitates a continuity. To overcome this problem such that this approach can be applied to an assembly of structures or geometries that have discontinuities such as cavities, it should be extended to a spectral element formulation. One of the first attempts of this approach is applied to piezoelectric energy harvester systems that shows promising results to be implemented for composite structure design problems [162].

Furthermore, it can be applied to different types of composite structures such as variable stiffness composites or to analyze different phenomenon such as non-linearity, post buckling, cracked or delaminated composite structures.

5.3 Side works

During the developing the spectral-Chebychev approach as the main work of investigations, we try to extend this approach to study various problems presented in following to show the capability of this technique.

5.3.1 Dynamic analysis of a doubly curved composite structure

In this research[163], a modeling framework for the dynamic analysis of doubly curved composite panels is developed. Lamination parameters are used to characterize the stiffness properties of the laminate, and the responses are calculated through the two-dimensional spectral-Tchebychev method. The proposed framework combines the computational efficiency advantages of both lamination parameters formulation and spectral-Tchebychev method which is extended for dynamic analysis of curved composite laminates.

5.3.2 Electromechanical analysis of functionally graded panels

This study [164] presents an electromechanical modeling approach for predicting the dynamics of (straight/curved) functionally graded panels with multiple surface-integrated piezo-patches. Bi-axial material variation is considered using the theory of mixture approach. The governing equations are derived following the first order shear deformation theory and the Hamilton's principle. The derived boundary value problem is solved numerically using a meshless approach based on Chebyshev polynomials. Mass and stiffness contributions of piezo-patch(es), as well as two-way electromechanical coupling behavior, are incorporated both for modal and harmonic analyses. To validate the accuracy of the presented solution technique, the results for various cases are compared to those obtained from finite-element analyses. It is shown that the maximum difference in the predicted natural frequencies is below 1%, but for a fraction of the computational time. Furthermore, the harmonic analysis results excellently match FE results. Note that material variation changes the spatial stiffness of the panel and thus, the functionally graded panel can be designed according to a predefined objective function using the proposed modeling approach. As a demonstration, specific to energy harvesting application, the voltage/power output was maximized through material and geometry/shape variations. It was demonstrated that significant improvements can be achieved through the presented methodology.

5.3.3 vibration analysis of axially moving doubly-curved panels/shells

In this research [165] a general model to study the vibration behavior of axially moving two-dimensional continuums in the presence of curvature along the moving axis is developed. To this end, an axially moving doubly-curved panel of variable radius of curvature is considered. The integral boundary value problem is obtained based on a higher-order shear deformation with first-order thickness stretching theory. Due to its high accuracy and computational performance, spectral Chebyshev approach is used to numerically solve the boundary value problem. Considering the geometry capabilities of the developed model, dynamics of various axially moving structures such as flat, singly- and doubly-curved plates/shells in different engineering applications with different boundary conditions can be investigated. The numerical results confirmed that the calculated natural frequencies for axially moving flat plates and circular cylindrical shells are in excellent agreement to those found in the literature and obtained via finite element approach. Furthermore, the effects of the axial ve-

locity, thickness stretching, curvature ratio, and boundary conditions on the natural frequencies and stability behavior of the doubly-curved panels are investigated.

5.3.4 Nonlinear resonances of axially functionally graded rotating beams

The purpose of the current study is to develop an accurate model to investigate the nonlinear resonances in an axially functionally graded beam rotating with timedependent speed. To this end, two important features including stiffening and Coriolis effects are modeled based on nonlinear strain relations. Equations governing the axial, chordwise, and flapwise deformations about the determined steady-state equilibrium position are obtained, and the rotating speed variation is considered as a periodic disturbance about this equilibrium condition. Multi-mode discretization of the equations is performed via the spectral Chebyshev approach and the method of multiple scales for Gyroscopic systems is employed to study the nonlinear behavior. After determining the required polynomial number based on convergence analysis, results obtained are verified by comparing to those found in literature and numerical simulations. Moreover, the model is validated based on simulations carried out by a commercial finite element software. Properties of the functionally graded material and the values of average rotating speed leading to 2:1 internal resonance in the system are found. Time and steady-state responses of the system under primary and parametric resonances caused by the time-dependent rotating speed are investigated when the system is tuned to 2:1 internal resonance. A comprehensive study on the time response, frequency response, and stability behavior shows that the rotating axially functionally graded beam exhibits a complicated nonlinear behavior under the effect of the rotating speed fluctuation frequency, damping coefficient, and properties of the functionally graded material.

5.3.5 Design of laminated conical shells

This study presents a modeling approach to accurately and efficiently predict the dynamics of laminated conical shells. The governing equations are derived based on the first order shear deformation theory kinematic equations following the Hamilton's principle. To express the strain energy of the shells, in-plane and bending lamination parameters are used. A two-dimensional spectral approach based on Chebyshev polynomials is implemented to solve the governing equations. The developed framework including the spectral-Chebyshev approach and lamination parameters

results in an accurate and computationally efficient solution method. To demonstrate the performance of the presented solution approach, various case studies including straight panels, curved shells, and truncated conical shells are investigated. The benchmarks indicate that the calculated non-dimensional natural frequencies excellently match the results found using finite element method and the simulation duration can be decreased by 100 folds. To leverage the computational performance of the presented approach, a stacking sequence optimization is performed to maximize the fundamental frequency of a shell geometry, and the corresponding fiber angles are retrieved from the optimized lamination parameters. Furthermore, a parametric analysis is performed to investigate the effect of geometry on the optimized lamination parameters (and fiber angles) based on fundamental natural frequency maximization.

Bibliography

[1] T. W. Clyne, D. Hull, An introduction to composite materials, Cambridge university press, 2019.

[2] J. N. Reddy, Mechanics of composite materials: selected works of Nicholas J. Pagano, Vol. 34, Springer Science & Business Media, 1994.

[3] K. K. Chawla, Composite materials: science and engineering, Springer Science & Business Media, 2012.

[4] C. T. Herakovich, Mechanics of composites: a historical review, Mechanics Research Communications 41 (2012) 1–20.

[5] M. K. Buragohain, Composite structures: design, mechanics, analysis, manufacturing, and testing, CRC press, 2017.

[6] J. R. Vinson, Sandwich structures (2001).

[7] D. Cripps, T. Searle, J. Summerscales, Open mold techniques for thermoset composites (2000).

[8] D. Sidwell, Hand lay-up and bag molding, in: Handbook of Composites, Springer, 1998, pp. 352–377.

[9] K. Swaminathan, D. T. Naveenkumar, A. M. Zenkour, E. Carrera, Stress, vibration and buckling analyses of FGM plates-A state-of-the-art review, Composite Structures 120 (2015) 10–31. `doi:10.1016/j.compstruct.2014.09.070`.
URL http://dx.doi.org/10.1016/j.compstruct.2014.09.070

[10] H. Chen, A. Wang, Y. Hao, W. Zhang, Free vibration of FGM sandwich doubly-curved shallow shell based on a new shear deformation theory with stretching effects, Composite Structures 179 (2017) 50–60. `doi:10.1016/j.compstruct.2017.07.032`.
URL http://dx.doi.org/10.1016/j.compstruct.2017.07.032

[11] N. El Meiche, A. Tounsi, N. Ziane, I. Mechab, et al., A new hyperbolic shear deformation theory for buckling and vibration of functionally graded sandwich plate, International Journal of Mechanical Sciences 53 (4) (2011) 237–247.

[12] T. Ye, G. Jin, Z. Su, Three-dimensional vibration analysis of functionally graded sandwich deep open spherical and cylindrical shells with general restraints, Journal of Vibration and Control 22 (15) (2016) 3326–3354.

[13] F. Tornabene, E. Viola, N. Fantuzzi, General higher-order equivalent single layer theory for free vibrations of doubly-curved laminated composite shells and panels, Composite Structures 104 (2013) 94–117.

[14] F. Tornabene, N. Fantuzzi, M. Bacciocchi, Free vibrations of free-form doubly-curved shells made of functionally graded materials using higher-order equivalent single layer theories, Composites Part B: Engineering 67 (2014) 490–509.

[15] Y. Hao, Z. Li, W. Zhang, S. Li, M. Yao, Vibration of functionally graded sandwich doubly curved shells using improved shear deformation theory, Science China Technological Sciences 61 (6) (2018) 791–808.

[16] F. Tornabene, N. Fantuzzi, M. Bacciocchi, E. Viola, J. N. Reddy, A numerical investigation on the natural frequencies of fgm sandwich shells with variable thickness by the local generalized differential quadrature method, Applied Sciences 7 (2) (2017) 131.

[17] P. Davies, Towards More Representative Accelerated Aging of Marine Composites, 2020. `doi:10.1007/978-3-030-31065-3_17`.

[18] M. T. Tran, A. T. Trinh, et al., Static and vibration analysis of cross-ply laminated composite doubly curved shallow shell panels with stiffeners resting on winkler–pasternak elastic foundations, International Journal of Advanced Structural Engineering 9 (2) (2017) 153–164.

[19] K. Swaminathan, D. Naveenkumar, A. Zenkour, E. Carrera, Stress, vibration and buckling analyses of fgm plates—a state-of-the-art review, Composite Structures 120 (2015) 10–31.

[20] V. Birman, L. W. Byrd, Modeling and analysis of functionally graded materials and structures (2007).

[21] H.-S. Shen, Functionally graded materials: nonlinear analysis of plates and shells, CRC press, 2016.

[22] S. S. Vel, R. Batra, Three-dimensional exact solution for the vibration of functionally graded rectangular plates, Journal of Sound and Vibration 272 (3-5) (2004) 703–730.

[23] A. J. Goupee, S. S. Vel, Optimization of natural frequencies of bidirectional functionally graded beams, Structural and Multidisciplinary Optimization 32 (6) (2006) 473–484.

[24] N. T. Alshabatat, K. Naghshineh, Optimization of natural frequencies and sound power of beams using functionally graded material, Advances in Acoustics and Vibration 2014 (2014).

[25] K. Maalawi, Optimization of functionally graded material structures: some case studies, in: Optimum Composite Structures, IntechOpen, 2018.

[26] T. Mori, K. Tanaka, Average stress in matrix and average elastic energy of materials with misfitting inclusions, Acta metallurgica 21 (5) (1973) 571–574.

[27] A. Neves, A. Ferreira, E. Carrera, M. Cinefra, C. Roque, R. Jorge, C. M. Soares, Static, free vibration and buckling analysis of isotropic and sandwich functionally graded plates using a quasi-3d higher-order shear deformation theory and a meshless technique, Composites Part B: Engineering 44 (1) (2013) 657–674.

[28] R. M. Jones, Taylor and francis,", Mechanics of Composite Materials (1999).

[29] C. C. Chamis, Mechanics of composite materials: past, present, and future, Journal of Composites, Technology and Research 11 (1) (1989) 3–14.

[30] J. C. Halpin, Effects of environmental factors on composite materials., Tech. rep., Air Force Materials Lab Wright-Patterson AFB OH (1969).

[31] L. L. Vignoli, M. A. Savi, P. M. Pacheco, A. L. Kalamkarov, Comparative analysis of micromechanical models for the elastic composite laminae, Composites Part B: Engineering 174 (2019) 106961.

[32] T. Mura, Micromechanics of defects in solids (martinus nijhoff, dordrecht, 1987)., and 179 149.

[33] K. Mercan, A. K. Baltacıoglu, Ö. Civalek, Free vibration of laminated and fgm/cnt composites annular thick plates with shear deformation by discrete singular convolution method, Composite Structures 186 (2018) 139–153.

[34] S. Nikbakht, S. Kamarian, M. Shakeri, A review on optimization of composite structures Part II: Functionally graded materials, Composite Structures 214 (December 2018) (2019) 83–102. `doi:10.1016/j.compstruct.2019.01.105`.
URL https://doi.org/10.1016/j.compstruct.2019.01.105

[35] M. F. Ashby, T. Evans, N. A. Fleck, J. Hutchinson, H. Wadley, L. Gibson, Metal foams: a design guide, Elsevier, 2000.

[36] J. Banhart, Manufacture, characterisation and application of cellular metals and metal foams, Progress in materials science 46 (6) (2001) 559–632.

[37] W. Pompe, H. Worch, M. Epple, W. Friess, M. Gelinsky, P. Greil, U. Hempel, D. Scharnweber, K. Schulte, Functionally graded materials for biomedical applications, Materials Science and Engineering: A 362 (1-2) (2003) 40–60.

[38] A. Hassani, A. Habibolahzadeh, H. Bafti, Production of graded aluminum foams via powder space holder technique, Materials & Design 40 (2012) 510–515.

[39] S.-Y. He, Y. Zhang, G. Dai, J.-Q. Jiang, Preparation of density-graded aluminum foam, Materials Science and Engineering: A 618 (2014) 496–499.

[40] M. Heshmati, F. Daneshmand, A study on the vibrational properties of weight-efficient plates made of material with functionally graded porosity, Composite Structures 200 (2018) 229–238.

[41] P. T. Thang, T. Nguyen-Thoi, D. Lee, J. Kang, J. Lee, Elastic buckling and free vibration analyses of porous-cellular plates with uniform and non-uniform porosity distributions, Aerospace Science and Technology 79 (2018) 278–287.

[42] S. Kitipornchai, D. Chen, J. Yang, Free vibration and elastic buckling of functionally graded porous beams reinforced by graphene platelets, Materials & Design 116 (2017) 656–665.

[43] K. Li, D. Wu, X. Chen, J. Cheng, Z. Liu, W. Gao, M. Liu, Isogeometric analysis of functionally graded porous plates reinforced by graphene platelets, Composite Structures 204 (2018) 114–130.

[44] S. Zhao, Z. Yang, S. Kitipornchai, J. Yang, Dynamic instability of functionally graded porous arches reinforced by graphene platelets, Thin-Walled Structures 147 (2020) 106491.

[45] S. Zghal, A. Frikha, F. Dammak, Mechanical buckling analysis of functionally graded power-based and carbon nanotubes-reinforced composite plates and curved panels, Composites Part B: Engineering 150 (2018) 165–183.

[46] P. Zhu, Z. Lei, K. M. Liew, Static and free vibration analyses of carbon nanotube-reinforced composite plates using finite element method with first order shear deformation plate theory, Composite Structures 94 (4) (2012) 1450–1460.

[47] I. Zaman, H.-C. Kuan, J. Dai, N. Kawashima, A. Michelmore, A. Sovi, S. Dong, L. Luong, J. Ma, From carbon nanotubes and silicate layers to graphene platelets for polymer nanocomposites, Nanoscale 4 (15) (2012) 4578–4586.

[48] M. A. Rafiee, J. Rafiee, Z. Wang, H. Song, Z.-Z. Yu, N. Koratkar, Enhanced mechanical properties of nanocomposites at low graphene content, ACS nano 3 (12) (2009) 3884–3890.

[49] J. P. Salvetat-Delmotte, A. Rubio, Mechanical properties of carbon nanotubes: A fiber digest for beginners, Carbon 40 (10) (2002) 1729–1734. `doi:10.1016/S0008-6223(02)00012-X`.

[50] S. Iijima, T. Ichihashi, Single-shell carbon nanotubes of 1-nm diameter, nature 363 (6430) (1993) 603–605.

[51] D. Bethune, C. H. Kiang, M. De Vries, G. Gorman, R. Savoy, J. Vazquez, R. Beyers, Cobalt-catalysed growth of carbon nanotubes with single-atomic-layer walls, Nature 363 (6430) (1993) 605–607.

[52] S. Iijima, Helical microtubules of graphitic carbon, nature 354 (6348) (1991) 56–58.

[53] D. WILLIAN Jr, Materials science and engineering: An introduction, 3ª edição, John Willey, New York (1994).

[54] K. M. Liew, X. Zhao, A. J. Ferreira, A review of meshless methods for laminated and functionally graded plates and shells, Composite Structures 93 (8) (2011) 2031–2041.

[55] H.-S. Shen, Nonlinear bending of functionally graded carbon nanotube-reinforced composite plates in thermal environments, Composite Structures 91 (1) (2009) 9–19.

[56] K. M. Liew, Z. Pan, L.-W. Zhang, The recent progress of functionally graded cnt reinforced composites and structures, Science China Physics, Mechanics & Astronomy 63 (3) (2020) 1–17.

[57] J. M. Wernik, S. A. Meguid, Multiscale modeling of the nonlinear response of nano-reinforced polymers, Acta Mechanica 217 (1-2) (2011) 1–16. `doi: 10.1007/s00707-010-0377-7`.

[58] E. T. Thostenson, Z. Ren, T. W. Chou, Advances in the science and technology of carbon nanotubes and their composites: A review, Composites Science and Technology 61 (13) (2001) 1899–1912. `doi:10.1016/S0266-3538(01) 00094-X`.

[59] M. Moniruzzaman, K. I. Winey, Polymer nanocomposites containing carbon nanotubes, Macromolecules 39 (16) (2006) 5194–5205. `doi:10.1021/ ma060733p`.

[60] B. Valter, M. K. Ram, C. Nicolini, Synthesis of multiwalled carbon nanotubes and poly(o-anisidine) nanocomposite material: Fabrication and characterization of its Langmuir-Schaefer films, Langmuir 18 (5) (2002) 1535–1541. `doi:10.1021/la0104673`.

[61] D. Qian, E. C. Dickey, R. Andrews, T. Rantell, Load transfer and deformation mechanisms in carbon nanotube-polystyrene composites, Applied Physics Letters 76 (20) (2000) 2868–2870. `doi:10.1063/1.126500`.

[62] E. T. Thostenson, T.-w. Chou, Aligned multi-walled carbon nanotube-reinforced composites : processing and mechanical characterization 77 (2002).

[63] P. Zhu, Z. X. Lei, K. M. Liew, Static and free vibration analyses of carbon nanotube-reinforced composite plates using finite element method with first order shear deformation plate theory, Composite Structures 94 (4) (2012) 1450–1460. `doi:10.1016/j.compstruct.2011.11.010`.
URL http://dx.doi.org/10.1016/j.compstruct.2011.11.010

[64] B. S. Aragh, A. H. Barati, H. Hedayati, Eshelby-Mori-Tanaka approach for vibrational behavior of continuously graded carbon nanotube-reinforced cylindrical panels, Composites Part B: Engineering 43 (4) (2012) 1943–1954. `doi:10.1016/j.compositesb.2012.01.004`.
URL http://dx.doi.org/10.1016/j.compositesb.2012.01.004

[65] H. N. Wadley, Multifunctional periodic cellular metals, Philosophical Transactions of the Royal Society A: Mathematical, Physical and Engineering Sciences 364 (1838) (2006) 31–68. `doi:10.1098/rsta.2005.1697`.

[66] F. Côté, V. S. Deshpande, N. A. Fleck, A. G. Evans, The compressive and shear responses of corrugated and diamond lattice materials, International Journal of Solids and Structures 43 (20) (2006) 6220–6242. `doi:10.1016/j.ijsolstr.2005.07.045`.

[67] V. S. Deshpande, N. A. Fleck, M. F. Ashby, Effective properties of the octet-truss lattice material, Journal of the Mechanics and Physics of Solids 49 (8) (2001) 1747–1769. `doi:10.1016/S0022-5096(01)00010-2`.

[68] I. Dayyani, A. D. Shaw, E. I. Saavedra Flores, M. I. Friswell, The mechanics of composite corrugated structures: A review with applications in morphing aircraft, Composite Structures 133 (2015) 358–380. `doi:10.1016/j.compstruct.2015.07.099`.
URL http://dx.doi.org/10.1016/j.compstruct.2015.07.099

[69] J. Yang, H. Wu, S. Kitipornchai, Buckling and postbuckling of functionally graded multilayer graphene platelet-reinforced composite beams, Composite Structures 161 (2017) 111–118.

[70] Y. Kiani, M. Mirzaei, Enhancement of non-linear thermal stability of temperature dependent laminated beams with graphene reinforcements, Composite Structures 186 (2018) 114–122.

[71] M. Ganapathi, B. Anirudh, C. Anant, O. Polit, Dynamic characteristics of functionally graded graphene reinforced porous nanocomposite curved beams based on trigonometric shear deformation theory with thickness stretch effect, Mechanics of Advanced Materials and Structures (2019) 1–12.

[72] Z. Liu, C. Yang, W. Gao, D. Wu, G. Li, Nonlinear behaviour and stability of functionally graded porous arches with graphene platelets reinforcements, International Journal of Engineering Science 137 (2019) 37–56.

[73] Q. Li, D. Wu, X. Chen, L. Liu, Y. Yu, W. Gao, Nonlinear vibration and dynamic buckling analyses of sandwich functionally graded porous plate with graphene platelet reinforcement resting on winkler–pasternak elastic foundation, International Journal of Mechanical Sciences 148 (2018) 596–610.

[74] S. S. Mirjavadi, M. Forsat, A. Hamouda, M. R. Barati, Dynamic response of functionally graded graphene nanoplatelet reinforced shells with porosity distributions under transverse dynamic loads, Materials Research Express 6 (7) (2019) 075045.

[75] A. R. Saidi, R. Bahaadini, K. Majidi-Mozafari, On vibration and stability analysis of porous plates reinforced by graphene platelets under aerodynamical loading, Composites Part B: Engineering 164 (2019) 778–799.

[76] D. Li, Layerwise theories of laminated composite structures and their applications: A review, Archives of Computational Methods in Engineering 28 (2) (2021) 577–600.

[77] R. F. Gibson, E. O. Ayorinde, Y.-F. Wen, Vibrations of carbon nanotubes and their composites: a review, Composites science and technology 67 (1) (2007) 1–28.

[78] G. Serhat, I. Basdogan, Design of curved composite panels for optimal dynamic response using lamination parameters, Composites Part B: Engineering 147 (2018) 135–146.

[79] M. Aydogdu, Conditions for functionally graded plates to remain flat under in-plane loads by classical plate theory, Composite Structures 82 (1) (2008) 155–157.

[80] B. Koohbor, S. Mallon, A. Kidane, A. Anand, V. Parameswaran, Through thickness elastic profile determination of functionally graded materials, Experimental Mechanics 55 (8) (2015) 1427–1440.

[81] Ö. Civalek, Vibration of laminated composite panels and curved plates with different types of fgm composite constituent, Composites Part B: Engineering 122 (2017) 89–108.

[82] K. Gao, W. Gao, D. Chen, J. Yang, Nonlinear free vibration of functionally graded graphene platelets reinforced porous nanocomposite plates resting on elastic foundation, Composite Structures 204 (2018) 831–846.

[83] F. Tornabene, Free vibration analysis of functionally graded conical, cylindrical shell and annular plate structures with a four-parameter power-law distribution, Computer Methods in Applied Mechanics and Engineering 198 (37-40) (2009) 2911–2935.

[84] S. Hosseini-Hashemi, K. Khorshidi, M. Amabili, Exact solution for linear buckling of rectangular mindlin plates, Journal of Sound and Vibration 315 (1-2) (2008) 318–342.

[85] F. Abad, J. Rouzegar, An exact spectral element method for free vibration analysis of fg plate integrated with piezoelectric layers, Composite Structures 180 (2017) 696–708.

[86] F. Tornabene, N. Fantuzzi, M. Bacciocchi, A new doubly-curved shell element for the free vibrations of arbitrarily shaped laminated structures based on weak formulation isogeometric analysis, Composite Structures 171 (2017) 429–461.

[87] A. G. Shenas, P. Malekzadeh, S. Ziaee, Vibration analysis of pre-twisted functionally graded carbon nanotube reinforced composite beams in thermal environment, Composite Structures 162 (2017) 325–340.

[88] J. Reddy, Analysis of functionally graded plates, International Journal for numerical methods in engineering 47 (1-3) (2000) 663–684.

[89] S. Pradyumna, J. Bandyopadhyay, Free vibration analysis of functionally graded curved panels using a higher-order finite element formulation, Journal of Sound and Vibration 318 (1-2) (2008) 176–192.

[90] F. Tornabene, N. Fantuzzi, F. Ubertini, E. Viola, Strong formulation finite element method based on differential quadrature: a survey, Applied Mechanics Reviews 67 (2) (2015).

[91] N. Fantuzzi, F. Tornabene, E. Viola, Four-parameter functionally graded cracked plates of arbitrary shape: a gdqfem solution for free vibrations, Mechanics of Advanced Materials and Structures 23 (1) (2016) 89–107.

[92] H. Matsunaga, Free vibration and stability of functionally graded shallow shells according to a 2d higher-order deformation theory, Composite Structures 84 (2) (2008) 132–146.

[93] F. Tornabene, A. Liverani, G. Caligiana, Fgm and laminated doubly curved shells and panels of revolution with a free-form meridian: a 2-d gdq solution for free vibrations, International Journal of Mechanical Sciences 53 (6) (2011) 446–470.

[94] F. Tornabene, N. Fantuzzi, M. Bacciocchi, The local gdq method for the natural frequencies of doubly-curved shells with variable thickness: a general formulation, Composites Part B: Engineering 92 (2016) 265–289.

[95] E. Carrera, Historical review of zig-zag theories for multilayered plates and shells, Appl. Mech. Rev. 56 (3) (2003) 287–308.

[96] A. Ferreira, E. Carrera, M. Cinefra, E. Viola, F. Tornabene, N. Fantuzzi, A. Zenkour, Analysis of thick isotropic and cross-ply laminated plates by generalized differential quadrature method and a unified formulation, Composites Part B: Engineering 58 (2014) 544–552.

[97] S. K. Kumar, D. Harursampath, E. Carrera, M. Cinefra, S. Valvano, Modal analysis of delaminated plates and shells using carrera unified formulation–mitc9 shell element, Mechanics of Advanced Materials and Structures 25 (8) (2018) 681–697.

[98] C. Shu, Differential quadrature and its application in engineering, Springer Science & Business Media, 2012.

[99] P. Tan, N. Nguyen-Thanh, T. Rabczuk, K. Zhou, Static, dynamic and buckling analyses of 3d fgm plates and shells via an isogeometric-meshfree coupling approach, Composite Structures 198 (2018) 35–50.

[100] C. H. Thai, A. Ferreira, T. Tran, P. Phung-Van, Free vibration, buckling and bending analyses of multilayer functionally graded graphene nanoplatelets reinforced composite plates using the nurbs formulation, Composite Structures 220 (2019) 749–759.

[101] R. Ansari, J. Torabi, R. Hassani, A comprehensive study on the free vibration of arbitrary shaped thick functionally graded cnt-reinforced composite plates, Engineering Structures 181 (2019) 653–669.

[102] T. J. Hughes, J. A. Cottrell, Y. Bazilevs, Isogeometric analysis: Cad, finite elements, nurbs, exact geometry and mesh refinement, Computer methods in applied mechanics and engineering 194 (39-41) (2005) 4135–4195.

[103] M. Khiloun, A. A. Bousahla, A. Kaci, A. Bessaim, A. Tounsi, S. Mahmoud, Analytical modeling of bending and vibration of thick advanced composite plates using a four-variable quasi 3d hsdt, Engineering with Computers 36 (3) (2020) 807–821.

[104] J. Zhao, K. Choe, C. Shuai, A. Wang, Q. Wang, Free vibration analysis of functionally graded carbon nanotube reinforced composite truncated conical panels with general boundary conditions, Composites Part B: Engineering 160 (2019) 225–240.

[105] R. Kadoli, N. Ganesan, Buckling and free vibration analysis of functionally graded cylindrical shells subjected to a temperature-specified boundary condition, Journal of sound and vibration 289 (3) (2006) 450–480.

[106] Y. Zhao, Y. Huang, M. Guo, A novel approach for free vibration of axially functionally graded beams with non-uniform cross-section based on chebyshev polynomials theory, Composite Structures 168 (2017) 277–284.

[107] B. Bediz, Three-dimensional vibration behavior of bi-directional functionally graded curved parallelepipeds using spectral tchebychev approach, Composite Structures 191 (2018) 100–112.

[108] B. Yagci, S. Filiz, L. L. Romero, O. B. Ozdoganlar, A spectral-tchebychev technique for solving linear and nonlinear beam equations, Journal of Sound and Vibration 321 (1-2) (2009) 375–404.

[109] M. R. Anamagh, B. Bediz, Three-dimensional dynamics of functionally graded and laminated doubly-curved composite structures having arbitrary geometries and boundary conditions, Composites Part B: Engineering 172 (February) (2019) 533–546. `doi:10.1016/j.compositesb.2019.05.087`.
URL https://doi.org/10.1016/j.compositesb.2019.05.087

[110] H. Zafarmand, M. Salehi, K. Asemi, Three dimensional free vibration and transient analysis of two directional functionally graded thick cylindrical panels under impact loading, Latin American Journal of Solids and Structures 12 (2) (2015) 205–225. `doi:10.1590/1679-78251099`.

[111] L. Demasi, 2D, quasi 3D and 3D exact solutions for bending of thick and thin sandwich plates, Journal of Sandwich Structures and Materials 10 (4) (2008) 271–310. `doi:10.1177/1099636208089311`.

[112] A. V. Marchuk, S. V. Reneiskaya, O. N. Leshchuk, Three-Dimensional Analysis of the Free Vibrations of Layered Composite Plates Based on the Semianalytic Finite-Element Method, International Applied Mechanics 56 (4) (2020) 481–497. `doi:10.1007/s10778-020-01031-9`.

[113] S. Natarajan, M. Haboussi, G. Manickam, Application of higher-order structural theory to bending and free vibration analysis of sandwich plates with CNT reinforced composite facesheets, Composite Structures 113 (1) (2014) 197–207. `arXiv:1403.1712`, `doi:10.1016/j.compstruct.2014.03.007`.
URL http://dx.doi.org/10.1016/j.compstruct.2014.03.007

[114] M. R. Moghaddam, G. H. Baradaran, Three-dimensional free vibrations analysis of functionally graded rectangular plates by the meshless local petrov–galerkin (mlpg) method, Applied Mathematics and Computation 304 (2017) 153–163.

[115] P. Malekzadeh, Three-dimensional free vibration analysis of thick functionally graded plates on elastic foundations, Composite Structures 89 (3) (2009) 367–373.

[116] P. Malekzadeh, M. Ghaedsharaf, Three-dimensional free vibration of laminated cylindrical panels with functionally graded layers, Composite Structures 108 (2014) 894–904.

[117] M. Farid, P. Zahedinejad, P. Malekzadeh, Three-dimensional temperature dependent free vibration analysis of functionally graded material curved panels resting on two-parameter elastic foundation using a hybrid semi-analytic, differential quadrature method, Materials and Design 31 (1) (2010) 2–13. `doi:10.1016/j.matdes.2009.07.025`.
URL http://dx.doi.org/10.1016/j.matdes.2009.07.025

[118] P. Malekzadeh, Three-dimensional free vibration analysis of thick functionally graded plates on elastic foundations, Composite Structures 89 (3) (2009) 367–373. `doi:10.1016/j.compstruct.2008.08.007`.
URL http://dx.doi.org/10.1016/j.compstruct.2008.08.007

[119] D. Liu, Z. Li, S. Kitipornchai, J. Yang, Three-dimensional free vibration and bending analyses of functionally graded graphene nanoplatelets-reinforced nanocomposite annular plates, Composite Structures 229 (2019) 111453.

[120] P. Malekzadeh, Y. Heydarpour, Mixed Navier-layerwise differential quadrature three-dimensional static and free vibration analysis of functionally graded carbon nanotube reinforced composite laminated plates, Meccanica 50 (1) (2015) 143–167. `doi:10.1007/s11012-014-0061-4`.

[121] A. Alibeigloo, Effect of viscoelastic interface on three-dimensional static and vibration behavior of laminated composite plate, Composites Part B: Engineering 75 (2015) 17–28. `doi:10.1016/j.compositesb.2015.01.025`.
URL http://dx.doi.org/10.1016/j.compositesb.2015.01.025

[122] A. Alibeigloo, H. Jafarian, Three-Dimensional Static and Free Vibration Analysis of Carbon Nano Tube Reinforced Composite Cylindrical Shell Using Differential Quadrature Method, International Journal of Applied Mechanics 8 (3) (2016) 1–23. `doi:10.1142/S1758825116500332`.

[123] A. Alibeigloo, K. M. Liew, Free vibration analysis of sandwich cylindrical panel with functionally graded core using three-dimensional theory of elasticity, Composite Structures 113 (1) (2014) 23–30. `doi:10.1016/j.compstruct.2014.03.004`.
URL http://dx.doi.org/10.1016/j.compstruct.2014.03.004

[124] P. Zahedinejad, P. Malekzadeh, M. Farid, G. Karami, A semi-analytical three-dimensional free vibration analysis of functionally graded curved panels, International Journal of Pressure Vessels and Piping 87 (8) (2010) 470–480.

[125] M. Adineh, M. Kadkhodayan, Three-dimensional thermo-elastic analysis of multi-directional functionally graded rectangular plates on elastic foundation, Acta Mechanica 228 (3) (2017) 881–899.

[126] A. E. Alshorbagy, M. A. Eltaher, F. Mahmoud, Free vibration characteristics of a functionally graded beam by finite element method, Applied Mathematical Modelling 35 (1) (2011) 412–425.

[127] K. Asemi, S. J. Salami, M. Salehi, M. Sadighi, Dynamic and static analysis of fgm skew plates with 3d elasticity based graded finite element modeling, Latin American Journal of Solids and Structures 11 (3) (2014) 504–533.

[128] H. A. Deveci, L. Aydin, H. Seçil Artem, Buckling optimization of composite laminates using a hybrid algorithm under puck failure criterion constraint, Journal of Reinforced Plastics and Composites 35 (16) (2016) 1233–1247.

[129] F.-X. Irisarri, D. H. Bassir, N. Carrere, J.-F. Maire, Multiobjective stacking sequence optimization for laminated composite structures, Composites Science and Technology 69 (7-8) (2009) 983–990.

[130] A. Vosoughi, H. D. Forkhorji, H. Roohbakhsh, Maximum fundamental frequency of thick laminated composite plates by a hybrid optimization method, Composites Part B: Engineering 86 (2016) 254–260.

[131] L. Aydin, O. Aydin, H. S. Artem, A. Mert, Design of dimensionally stable composites using efficient global optimization method, Proceedings of the Institution of Mechanical Engineers, Part L: Journal of Materials: Design and Applications 233 (2) (2019) 156–168.

[132] A. R. Setoodeh, M. Shojaee, Critical buckling load optimization of functionally graded carbon nanotube-reinforced laminated composite quadrilateral plates, Polymer Composites 39 (2018) E853–E868. `doi:10.1002/pc.24289`.

[133] T. Vo-Duy, T. Truong-Thi, V. Ho-Huu, T. Nguyen-Thoi, Frequency optimization of laminated functionally graded carbon nanotube reinforced composite quadrilateral plates using smoothed FEM and evolution algorithm, Journal of Composite Materials 52 (14) (2018) 1971–1986. `doi:10.1177/0021998317737831`.

[134] K. Torabi, H. Afshari, Optimization of flutter boundaries of cantilevered trapezoidal functionally graded sandwich plates, Journal of Sandwich Structures and Materials 21 (2) (2019) 503–531. `doi:10.1177/1099636217697492`.

[135] Q. X. Lieu, J. Lee, D. Lee, S. Lee, D. Kim, J. Lee, Shape and size optimization of functionally graded sandwich plates using isogeometric analysis and adaptive hybrid evolutionary firefly algorithm, Thin-Walled Structures 124 (November 2017) (2018) 588–604. `doi:10.1016/j.tws.2017.11.054`. URL https://doi.org/10.1016/j.tws.2017.11.054

[136] M. Ashjari, M. R. Khoshravan, Multi-objective optimization of a functionally graded sandwich panel under mechanical loading in the presence of stress constraint, Journal of the Mechanical Behavior of Materials 26 (3-4) (2017) 79–93. `doi:10.1515/jmbm-2017-0017`.

[137] J. H. Affdl, J. Kardos, The halpin-tsai equations: a review, Polymer Engineering & Science 16 (5) (1976) 344–352.

[138] E. B. Becker, G. F. Carey, J. T. Oden, Finite elements, an introduction: Volume i., ., 258 (1981) 1981.

[139] Y. Benveniste, A new approach to the application of mori-tanaka's theory in composite materials, Mechanics of materials 6 (2) (1987) 147–157.

[140] S. Kelsey, R. Gellatly, B. Clark, The Shear Modulus of Foil Honeycomb Cores, Aircraft Engineering and Aerospace Technology 30 (10) (1958) 294–302. `doi:10.1108/eb033026`.

[141] W. Q. Sun, W. Cheng, Finite element model updating of honeycomb sandwich plates using a response surface model and global optimization technique, Structural and Multidisciplinary Optimization 55 (1) (2017) 121–139. `doi:10.1007/s00158-016-1479-1`.
URL http://dx.doi.org/10.1007/s00158-016-1479-1

[142] J. Klintworth, W. Stronge, Elasto-plastic yield limits and deformation laws for transversely crushed honeycombs, International Journal of Mechanical Sciences 30 (3-4) (1988) 273–292.

[143] F. Scarpa, G. Tomlinson, Theoretical characteristics of the vibration of sandwich plates with in-plane negative Poisson's ratio values, Journal of Sound and Vibration 230 (1) (2000) 45–67. `doi:10.1006/jsvi.1999.2600`.

[144] M. Grediac, A finite element study of the transverse shear in honeycomb cores, International Journal of Solids and Structures 30 (13) (1993) 1777–1788. `doi:10.1016/0020-7683(93)90233-W`.

[145] J. Zhang, M. F. Ashby, The out-of-plane properties of honeycombs, International Journal of Mechanical Sciences 34 (6) (1992) 475–489. `doi:10.1016/0020-7403(92)90013-7`.

[146] J.N. Reddy, Mechanics of laminated composite plates and shells: theory and analysis (2003). `doi:10.1007/978-1-4471-0095-9`.

[147] B. Bediz, S. Aksoy, A spectral-Tchebychev solution for three-dimensional dynamics of curved beams under mixed boundary conditions, Journal of Sound and Vibration 413 (2018) 26–40. `doi:10.1016/j.jsv.2017.10.006`.
URL http://dx.doi.org/10.1016/j.jsv.2017.10.006

[148] D. Gottlieb, S. A. Orszag, Numerical analysis of spectral methods: theory and applications, SIAM, 1977.

[149] R. Pasquetti, F. Rapetti, Spectral element methods on triangles and quadrilaterals: comparisons and applications, Journal of Computational Physics 198 (1) (2004) 349–362.

[150] S. Filiz, B. Bediz, L. A. Romero, O. B. Ozdoganlar, A spectral-Tchebychev solution for three-dimensional vibrations of parallelepipeds under mixed boundary conditions, Journal of applied mechanics 79 (5) (2012).

[151] S. Filiz, B. Bediz, L. Romero, O. B. Ozdoganlar, Three dimensional dynamics of pretwisted beams: A spectral-tchebychev solution, Journal of Sound and Vibration 333 (10) (2014) 2823–2839.

[152] B. Bediz, U. Kumar, T. L. Schmitz, O. B. Ozdoganlar, Modeling and experimentation for three-dimensional dynamics of endmills, International Journal of Machine Tools and Manufacture 53 (1) (2012) 39–50.

[153] B. W. Bader, T. G. Kolda, Algorithm 862: Matlab tensor classes for fast algorithm prototyping, ACM Transactions on Mathematical Software (TOMS) 32 (4) (2006) 635–653.

[154] B. W. Bader, T. G. Kolda, et al., Matlab tensor toolbox version 2.5, Available online, January 7 (2012).

[155] Y. Xue, G. Jin, X. Ma, H. Chen, T. Ye, M. Chen, Y. Zhang, Free vibration analysis of porous plates with porosity distributions in the thickness and in-plane directions using isogeometric approach, International Journal of Mechanical Sciences 152 (2019) 346–362.

[156] L.-K. Yao, B. He, Y. Zhang, W. Zhou, Semi-analytical finite strip transfer matrix method for buckling analysis of rectangular thin plates, Mathematical Problems in Engineering 2015 (2015).

[157] N. M. Barkoula, B. Alcock, N. O. Cabrera, T. Peijs, Flame-Retardancy Properties of Intumescent Ammonium Poly(Phosphate) and Mineral Filler Magnesium Hydroxide in Combination with Graphene, Polymers and Polymer Composites 16 (2) (2008) 101–113. `arXiv:1206.4529`, `doi:10.1002/pc`.

[158] R. J. Allemang, The modal assurance criterion–twenty years of use and abuse, Sound and vibration 37 (8) (2003) 14–23.

[159] R. Hooke, T. A. Jeeves, "Direct Search" Solution of Numerical and Statistical Problems, Journal of the ACM (JACM) 8 (2) (1961) 212–229. `doi:10.1145/321062.321069`.

[160] M. Wetter, J. Wright, Comparison of a Generalized Pattern Search and a Genetic Algorithm Optimization Method, Ibpsa (2003) 1401–1408.

[161] A. Aghakhani, P. L. Motlagh, B. Bediz, I. Basdogan, A general electromechanical model for plates with integrated piezo-patches using spectral-tchebychev method, Journal of Sound and Vibration 458 (2019) 74–88.

[162] S. Alan, B. Bediz, A novel electromechanical spectral element method for piezoelectric energy harvester plates, Journal of Sound and Vibration 505 (2021) 116139.

[163] G. Serhat, M. R. Anamagh, B. Bediz, I. Basdogan, Dynamic analysis of doubly curved composite panels using lamination parameters and spectral-tchebychev method, Computers & Structures 239 (2020) 106294.

[164] P. L. Motlagh, M. R. Anamagh, B. Bediz, I. Basdogan, Electromechanical analysis of functionally graded panels with surface-integrated piezo-patches for optimal energy harvesting, Composite Structures 263 (2021) 113714.

[165] S. Lotfan, M. R. Anamagh, B. Bediz, A general higher-order model for vibration analysis of axially moving doubly-curved panels/shells, Thin-Walled Structures 164 (2021) 107813.

APPENDIX A

The in-plane geometric information of the arbitrary cross-sections in the third case study is given in Fig. A.1. To map the arbitrary cross-section into a simple rectangular cross-section using Eq. (2.32), a fourth order polynomial mapping is used. As shown in Fig. A.1, fourth order polynomial mapping necessitates 25 sampling points.
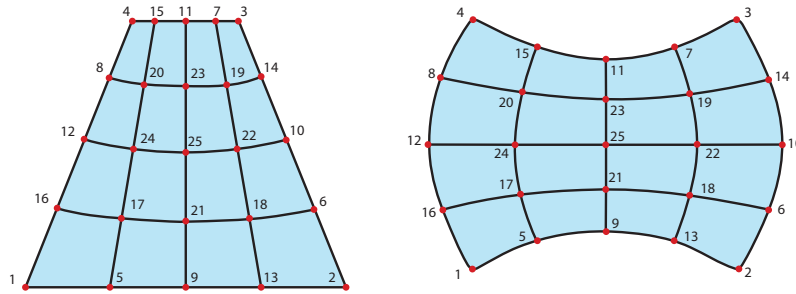
Figure A.1 Coordinates of the arbitrary in-plane cross-section geometry used in the case studies: **(i)** tapered geometry (top figure), **(ii)** complex-curved geometry (bottom figure)

Points 1, 2, 3, and 4 in Fig. A.1 correspond to the four edges of the rectangular cross-section as seen in Fig. 2.6. Table A.1 shows the x and y positions of each mapping point used in this study. The details of the mapping procedure is described in detail in [107]. Note that the accuracy of the cross-sectional mapping highly depends on the selection of the mapping points and the order of the polynomial mapping; however, in this study no attempt has been made to obtain the optimum mapping.

Table A.1 Positions (x and y coordinates) of the 25 sampling points used to map the complex cross-section into a simple rectangular cross-section.

Point #	Tapered Geometry		Curved Geometry	
	x [m]	y [m]	x [m]	y [m]
1	-3	0	-1.5	-1
2	3	0	1.5	-1
3	1	5	1.5	1
4	-1	5	-1.5	1
5	-1.413	0	-0.760	-0.813
6	2.410	1.490	1.868	-0.559
7	0.583	5	0.760	0.813
8	-1.427	3.932	-1.868	0.559
9	0	0	0	-0.750
10	1.893	2.766	2	0
11	0	5	0	0.750
12	-1.893	2.766	-2	0
13	1.413	0	0.760	-0.813
14	1.427	3.932	1.868	0.559
15	-0.583	5	-0.760	0.813
16	-2.410	1.490	-1.868	-0.559
17	-1.238	1.262	-0.944	-0.465
18	1.238	1.262	0.944	-0.465
19	0.750	3.791	0.944	0.465
20	-0.750	3.791	-0.943	0.434
21	0	1.263	0	-0.434
22	0.970	2.581	1.010	0
23	0	3.777	0	0.434
24	-0.970	2.581	-1.010	0
25	0	2.544	0	0